Texture evolution in high-pressure torsion processing

Hiba Azzeddine, Djamel Bradai, Thierry Baudin, Terence G Langdon

Texture evolution in high-pressure torsion processing

Hiba Azzeddine[1,*], Djamel Bradai[2], Thierry Baudin[3], Terence G. Langdon[4]

[1] Laboratoire Matériaux et Energies Renouvelables, Faculté des Sciences, Université Mohamed Boudiaf, M'sila, 28000, Algeria.
[2] Faculty of Physics, University of Sciences and Technology Houari Boumediene, Algiers, Algeria
[3] Université Paris-Saclay, CNRS, Institut de chimie moléculaire et des matériaux d'Orsay, 91405, Orsay, France
[4] Materials Research Group, Department of Mechanical Engineering, University of Southampton, Southampton SO17 1BJ, UK

***** Corresponding author: Prof. Hiba Azzeddine, email: hiba.azzeddine@univ-msila.dz

Abstract

Among the severe plastic deformation processing (SPD) of materials, high-pressure torsion (HPT) is known to induce considerable amounts of plastic strain and crucial grain refinement up to the nanometer scale. There have been several reviews on the mechanical properties and/or microstructure correlations of SPD-processed materials published during the last two decades. By contrast, a review on the crystallographic texture evolution during HPT processing is not at present available. Consequently, this work was undertaken to review the texture evolution in Face-Centered Cubic (FCC), Body-Centered Cubic (BCC) and Hexagonal Close-Packed (HCP) crystal structure materials processed exclusively by HPT with a special emphasis on the influence of many intrinsic and extrinsic factors such as the imposed strain, the deformation temperature and the alloying elements.

Keywords: alloys; deformation; high-pressure torsion; recrystallization; texture.

Contents

1. Introduction

At the present time the application of severe plastic deformation (SPD) is known as the most effective 'top-down' procedure for achieving exceptional grain refinement in bulk solids through attaining ultrafine microstructures within the submicrometer (0.1–1 μm) or nanometer range (<100 nm) with relatively large fractions of high-angle grain boundaries (HAGBs) and also without changing significantly the overall dimensions of the sample. Usually this is possible through the application of very high strains via deformation under extensive hydrostatic pressure leading to an accumulation of a high dislocation density and/or extensive numbers of vacancies. A combination of an ultrafine grain size and a high density of lattice defects greatly enhances the mechanical and physical properties of the deformed materials such as strength, ductility, the occurrence of superplasticity and conductivity. Furthermore, SPD processing can impressively modify the nature of the solid-state phase transformation including the sequence and kinetics in various materials [1-12].

Several SPD processing techniques have been proposed but it is noted that equal-channel angular pressing (ECAP) [13], accumulative roll-bonding (ARB) [14] and high-pressure torsion (HPT) [15] have received the most scientific and industrial attention. Figure 1 shows a schematic illustration, reference system, and the appropriate relationship for the equivalent strain for each three of these SPD techniques where the relationships for the equivalent strains are given in [16] for ECAP, [17] for ARB and [18] for HPT.

In ECAP processing a billet with a round or square cross-section deforms by a simple shear strain when its passes through a special die (Figure 1a). The cross-section of the billet remains unchanged which permits a repetition of the deformation and hence an accumulation of very large strains [13]. Different ECAP routes were proposed based

on the rotation of the billet about the pressing axis between the various passes in different dies formed with different angles Φ and Ψ which lead to various microstructural and mechanical properties evolutions [19]. More details on the principles of ECAP processing are given in other reports [13, 20, 21].

ARB processing (Figure 1b) consists of rolling a sheet usually to 50% reduction of thickness, cutting the sheet in two halves, stacking them together after degreasing and wire-brushing to achieve the original thickness of the sheet and then rolling again [14]. Consequently, several repetitions are possible to achieve extensive strains. A modified ARB processing procedure was proposed and labeled cross-ARB (CARB) in which the sheet is rotated about 90° around the normal direction after each ARB cycle [22]. This change in deformation path affects significantly the grain refinement and then the mechanical properties such as the tensile strength [22-26]. ARB processing is a useful method for manufacturing metal matrix composite materials and for multilayer composite materials such as Al/B4C [23], Al/Mg [27], and Cu/Nb [28] or with more than two different materials like Al/Ti/Nb [29] and Al/Cu/Mg [30].

The principle of HPT processing shown in Figure 1c demonstrates that a disc sample undergoes a torsional shear straining under a high hydrostatic pressure (typically about 1–6 GPa). The equivalent strain is not homogeneously distributed across the disc and instead it varies with the distance from the center of the disc as shown by the equation in Figure 1c [18]. More details on the fundamentals and applications of HPT processing and the historical development is given in other reports [31-33]. Several modified HPT processing methods were proposed over the last decade such as high-pressure tube twisting (HPTT) [34], tube high-pressure shearing (t-HPS) [35, 36], high-pressure-double-torsion (HPDT) [34], high-pressure sliding (HPS) [37], reversal high pressure torsion (RHPT) [38] and high pressure compressive shearing (HPCS) [39] in

order to provide solutions to the limitations of HPT processing such as the inhomogeneity of the shear strain across the disc radius or the smallness of the sample [40]. Recently, it was demonstrated that HPT processing is an excellent tool for the consolidation of metal powders [41-43] and for fabricating hybrid systems in order to ultimately obtain metal matrix nanocomposites (MMNCs) such as Al–Mg [44-46], Al-Cu [47] and Zn-Mg [48].

At present, the ECAP and ARB processing techniques are widely investigated and they have attracted more industrial attention than HPT processing because they provide the capability of producing fairly large billets (for ECAP) and sheets (for ARB) so that they may be used in a range of structural applications [13, 49]. By contrast, HPT processing suffers from a significant handicap because of the smallness of the samples which appears to render this technique generally inappropriate for industrial implementation [33]. Nevertheless, it has been demonstrated that HPT processing can lead to more significant grain refinement than ARB and ECAP processing [49-54] and in addition HPT produces a higher fraction of high-angle grains boundaries (HAGBs) [55, 56]. It is reasonable to conclude, therefore, that processing by HPT will attract more attention with the increasing current emphasis on the commercialization of bulk nanostructured materials [57].

The derived equation for the estimation of equivalent strain in HPT (Figure 1) indicates that HPT processing is capable of reaching an unlimited amount of strain in a single operation due to the nature of the HPT process through the superimposition of hydrostatic pressure and torsion [15, 32]. By contrast, ECAP [18] and ARB [13] processing require several passes in order to achieve large strains. HPT processing allows materials with low crystal symmetry, such as magnesium-based alloys, to be severely deformed at room temperature (RT) without cracking due to the development

of a hydrostatic stress [58, 59]. Moreover, HPT processing is considered a powerful process for solid-state consolidation from metallic powders and other constituents [60-66].

For many years, scientific research was focused on understanding the effect of grain refinement and dislocation density on the strain hardening of SPD-processed materials [2]. Recently, crystallographic texture was demonstrated to contribute significantly in the strain hardening, especially during the early stages of deformation [67, 68].

In practice, crystallographic texture (or preferred orientations) is defined as the quantitative orientation distribution of grains in a polycrystal aggregate. Often, the preferred orientation is mainly categorized into the "deformation texture" and the "recrystallization (or annealing) texture". The development of the texture is observed during crystallization from a melt (casting) or more frequently during thermo-mechanical processing such as welding and heat treatment [69].

The texture mainly evolves during deformation processing from grain rotation via the activity of different slip systems and/or twinning which leads to the formation of intragranular substructures. These latter often exhibit orientation deviations from the initial parent grain orientation and the substructures will subsequently move towards characteristic preferred orientations dictated by the imposed deformation [70]. For example, materials develop a shear texture after ECAP and HPT processing because both processing methods are essentially shear-based processes [54, 68, 71, 72] while a typical rolling texture is usually observed for ARB-processed materials due to its plane-strain nature [27, 49, 73].

Consequently, texture development has a strong effect on different properties of the materials and this may be useful for achieving additional information in areas such

as the deformation mechanisms [74, 75], the role of strain hardening [76-81], phase transformations including precipitation kinetics [82] and recrystallization processes [83-86], the significance of mechanical anisotropy [87-89] and other physical properties such as the magnetic, photovoltaic and corrosion properties [90-95]. It is important to note that there is no evidence for any direct correlation between texture and the electrical conductivity evolution. However, there is an experimental study on a low carbon steel processed by ECAP followed by modeling which shows that the texture can induce grain coarsening during large strain deformation [96-98]. This was explained because if two neighboring grains develop similar orientations during deformation then the disorientation between them progressively diminishes so that high-angle grain boundaries transform to low-angle grain boundaries and this thereby produces a coalescence of neighboring grains into larger grains [96, 97].

Figure 2 gives an example on the effect of different texture orientations on the forming anisotropy which is generally defined as the Lankford coefficient or R-value [88]. The R-value is defined as the ratio of the true strains in the width and thickness directions measured in tensile tests. Figure 2 shows that Cube {001}<100> and Goss {110}<100> known as the recrystallization texture possessed low R-values compared to the rolling texture (the Copper {112}<111> and Brass {110}<112> components). The shear texture components (A{111}<110> and A* {111}<112>) caused an increase in the R-value, while the C {001}<110> component has an insignificant influence on the R-value [88]. Such results demonstrate that rolling and shear textures can improve formability in deep drawing by comparison with the recrystallization texture. By contrast, sharpening the Goss {110}<100> and Cube {001}<100> components is beneficial for improving the magnetic and photovoltaic properties of materials, respectively [90, 92].

Several reviews on the resulting microstructures and the mechanical properties of materials and alloys processed by different SPD processing techniques are now available [15, 20, 21, 99-110]. However, there are to date only very limited reviews dealing with the textural evolutions after SPD processing [70, 71] and the available information is especially limited for HPT processing. Hence, the main objective of the present review is to provide a comprehensive compilation of existing data on textural evolution of materials having FCC, BCC and HCP crystal structures when processed exclusively by HPT.

In the present review the texture evolution was first grouped based on the crystalline structure (FCC, BCC, and HCP). For each group, the texture review was divided into three sections: (1) effect of initial conditions of materials, (2) effect of HPT processing deformation conditions and (3) evolution of recrystallization texture of HPT-processed materials. In addition, this review attempts to provide a direct correlation between the texture evolution, grain refinement and different properties, especially the mechanical properties, based on the available published data for each crystalline structure. Finally, texture simulations during HPT processing are given for different materials and texture comparisons are presented with some HPT processing variants (HPDT, RHPT, HPTT and HPCS) and combinations with other SPD processing procedures.

2. Texture evolution after HPT processing for different materials

In principle, the texture may be determined either globally by X-ray or neutron diffraction or locally by electron backscatter diffraction (EBSD) measurements. Both of these procedures offer specific advantages and some limitations as a consequence of the

fundamental characteristics of the radiation and the nature of the interaction with metals [111].

The ideal shear texture components present in FCC, BCC and HCP materials are described initially before providing reviews of the evolution of texture after HPT processing for these different structures. The texture components are characterized by the Miller indices ({hkl} <uvw>) and the Euler angles (φ_1, Φ, φ_2) in the Bunge notation and described in the Euler space from the calculated Orientation Distribution Function (ODF) and from experimental or recalculated pole figures [112].

2.1.Texture evolution after HPT processing of FCC materials

2.1.1. Ideal shear texture components for materials with FCC structure

The shear texture in FCC materials is typically formed of *A*, $\bar{A}$, A_1^*, A_2^* , *B*, $\bar{B}$ and *C* components [113-115]. These are described in terms of a conventional {hkl} <uvw> notation where the plane {hkl} is parallel to the shear plane and <uvw> is the crystal direction parallel to the shear direction. However, these texture components can be described in different spaces linked to the sample coordinate system. Figure 3 and Table 1 illustrate the ideal positions of different texture components in ODF sections at φ_2 = 0 and 45 ° and the {111} pole figure with respect to the plane measurements for the SD-RD, SD-CD and CD-RD planes where SD represents the shear direction, RD is the radial direction and CD is the compression direction (see Figure 1c). SD, RD and CD are referred to as the *x*, *y*, and *z* directions, respectively. It should be noted that all pole figures for FCC, BCC and HCP symmetries are presented in equal area projections. The majority of published reports presents the texture on the SD-RD and SD-CD planes [54, 72, 116-136] and rarely on the CD-RD plane [137].

The presence of all these texture components allows the formation of two fibers: an *A*-fiber ({111}// SP), where SP is the shear plane (or defined as the SD-RD plane) containing *A*, $\bar{A}$, A_1^* and A_2^* components and a *B*-fiber (<110>//SD) with *A*, $\bar{A}$, *B*, $\bar{B}$ and *C* components. The illustration of the *A* and *B* fibers can be seen in the {111} pole figure (Figure 3).

It should be noted that the presentation of the ideal pole figures and ODF are calculated using triclinic symmetry (φ_1 = 0–360°, Φ = 0–90°, φ_2 = 0–90°). Several researchers opted for monoclinic symmetry (φ_1 = 0–180°, Φ = 0–90°, φ_2 = 0–90°) to calculate the ODF. In this case, the two pairs of *A* and $\bar{A}$ and the *B* and $\bar{B}$ components have the same intensity. By contrast, the A_1^* and A_2^* components do not present the same intensity since they are not symmetric with respect to the monoclinic symmetry.

Several reports present the evolution of the texture strength by calculating the texture index I using the following equation [77]:

$$I = \frac{1}{8\pi^2}\int_G f^2(g)dg \quad (1)$$

where f(g) is the ODF values, G is the Euler space and I = 1 for materials with a random texture while a single orientation should have an infinite value of I [77].

Table 2 summarizes the main texture evolution as a function of the equivalent strain after HPT processing of several FCC materials available in the literature [54, 72, 116-137]. Accordingly, in the next sections the texture evolution is discussed based on different parameters such as the nature of the processed materials (such as stacking fault energy, initial condition prior to HPT processing) and the HPT processing conditions (such as the accumulated shear strain, the examination position and the deformation temperature). Finally, the recrystallization texture of HPT-processed FCC materials is also presented and discussed.

It is worth noting that in some published data the imposed strain during HPT processing was not precisely given due to a lack of information for the experimental conditions and hence in some places the accumulated strain was specified only in terms of the total numbers of HPT turns (N).

2.1.2. Effect of initial conditions of FCC materials

2.1.2.1.Effect of stacking fault energy

It is well known that the plastic deformation is accommodated by the activation of sufficient dislocation glide systems in materials with a high stacking fault energy, γ_{SFE}, while a decreasing γ_{SFE} promotes deformation by mechanical twinning. Figure 4 shows an example of the effect of the γ_{SFE} on the nature of the texture after HPT processing. The texture of materials with high γ_{SFE} such as pure Al (~160 mJ/m^2) [116-118, 138], Pd-10Au (% wt.)(~150 mJ/m^2) [133] and pure Ni (~128 mJ/m^2) [122, 139-141] consist of a weak *A*-fiber and strong *B*-fiber with the dominance of the *C* component (as shown in Figure 4a). However, changing the initial grain size of the Pd-10Au alloy leads to a very different deformation texture [133, 134] where this effect of the initial grain size is discussed in the next section. By contrast, the texture of materials with medium γ_{SFE} such as Pure Cu (~78 mJ/m^2) is characterized by a strong *B*-fiber with the dominance of $B/\bar{B}$ at the expense of the *C* component [127]. For materials with low γ_{SFE} such as the CrMnFeCoNi high-entropy alloy (γ_{SFE} ~ 22–35 mJ/m^2 [142, 143]), the texture is characterized by the presence of A_1^* and A_2^* components and sharp $B/\bar{B}$ components. Apparently, the evolution of the texture of materials with different γ_{SFE} values is similar for conventional torsion deformation and HPT processing [144]. The difference in the nature of texture formation in the different materials is related to the activation of dislocation slip systems and twinning in the deformed materials since these

processes can occur only in specific crystallographic planes and hence lead to preferred orientations.

It is interesting to note that the compilation in Table 2 demonstrates that the texture evolution after high shear strains is also affected by the value of the γ_{SFE}. For example, the texture of Al-based alloys becomes weak after high shear strains [116-121, 129] while the texture of Ni and Cu-based alloys appear to be reasonably stable [72, 123, 127, 128]. This difference is related to the hardening and grain refinement behaviors in high and low γ_{SFE} alloys. Thus, alloys with high γ_{SFE} are characterized by softening behavior during high strain (as illustrated in Figure 5) due to the rapid annihilation of dislocations, their rearrangement to sub-grains with LAGBs and then their transformation to HAGBs to produce ultrafine grains [145, 146]. This grain refinement process is termed continuous dynamic recrystallization (CDRX) and it is characterized by a homogeneous microstructure [106]. It is interesting to point out that CDRX is the main grain refinement mechanism operating in low to high γ_{SFE} materials processed at strains higher than 3 such as cold to warm SPD ($T < 0.5T_m$, T_m is the melting temperature) [106]. While discontinuous dynamic recrystallization (DDRX), which involves nucleation and grain growth processes, is responsible for the grain refinement in low to medium γ_{SFE} materials SPD processed at high temperatures ($T > 0.5T_m$) [106].

This behavior leads to rapid microstructural recovery and a change in the texture evolution as shown in Table 2, especially for Al-based alloys. By contrast, lowering the γ_{SFE} leads to strain hardening without microstructural recovery (as illustrated in Figure 5) [146, 147] due to the decrease in the rate of annihilation of dislocations since the recombination and cross-slip of dissociated dislocations is difficult and this causes a

delay in the recovery and dynamic recrystallization (DRX) [148]. This behavior produces more grain refinement and a stable texture at high shear strains.

A schematic illustration of hardening models (without recovery, with recovery and softening) for materials processed by HPT [146] and experimental examples are presented in Figure 5 for CrMnFeCoNi (low γ_{SFE} ~ 22–35 mJ/m^2) [149], Cu-2.5Ni-0.6Ni alloy (medium γ_{SFE} ~64.2 mJ/m^2) [150] and pure Al (high γ_{SFE} (~160 mJ/m^2) [151]. The third model known as the strain softening model was proposed based on the microhardness behavior of Al-Zn and Pb-Sn after HPT processing [146]. In such alloys, HPT processing causes significant grain refinement but with a corresponding decrease in the microhardness compared with the initial conditions due mainly to the dissolution of precipitates particles during HPT processing [152-156]. Unfortunately, a correlation between this model and the texture evolution is not possible at present due to the lack of any texture experimental results in these materials. A discussion on the correlation of texture evolution with the different hardening models can be found also for HCP materials in section 2.3.3.3.

The results collected until now are limited especially to FCC materials with low γ_{SFE} values but Table 3 summarizes the general texture evolutions as a function of the γ_{SFE} values correlated with deformation mechanisms and strain hardening models.

A comparison of texture evolution of a Cu-2.5Ni-0.6Si alloy (low γ_{SFE} ~64.2 mJ/m^2) and a Fe-36Ni alloy (high γ_{SFE} ~122 mJ/m^2) under similar HPT processing conditions is presented in Figure 6 [157]. As can be seen, a typical shear texture with the presence of all shear components is formed immediately after N = 1/2 turn for the low γ_{SFE} alloy (Cu-2.5Ni-0.6Si alloy) and the texture of the alloy appears to be stable after N = 1, 5 and 10 turns. By contrast, the texture evolution of the high γ_{SFE} alloy (Fe-

36Ni alloy) exhibits different trends. A nearly typical shear texture with the presence of most shear texture components gradually develops until N = 5 turns.

The fraction of different grain boundary misorientations (very low-angle grain boundaries, VLAGB (2–5°), LAGB (5–15°) and HAGB (> 15°)) in the shear components for both alloys after HPT processing for N = 10 turns as presented in Table 4 demonstrates that the Cu-2.5Ni-0.6Si alloy contains a low fraction of HAGBs ~2.6–4.6% compared with ~13–18% of HAGBs in the Fe-36Ni alloy. These behaviors confirm the slow rate of formation of new grains as designated HAGBs in the low γ_{SFE} alloys [157].

The evolution and variation of the texture as a function of accumulated shear strain is discussed in more detail in section 2.1.3.1.

2.1.2.2.Effect of initial grain size

Obviously, the type of shear texture after HPT processing will change with a change in the initial grain size of the alloy [133, 134]. As can be seen in Figure 7, a typical shear texture of materials with high γ_{SFE} (presence of weak *A*-fiber and strong *B*-fiber with a dominance of the *C* component) is observed after N = 1/2 turn (ε = 9–12) in the Pd-10Au (wt. %) alloy having an initial grain size of 100 μm (coarse grains) [133]. The texture development in the Pd-10Au alloy with an initial grain size above 20 nm (nanocrystalline) under identical HPT processing conditions is more typical of materials with low γ_{SFE} (showing the presence of $B/\bar{B}$ and A_2^* components) with the presence of a new component named “Oblique Cube” as indicated in Figure 7. For an initial grain size lower than 20 nm the texture of the HPT-processed Pd-10Au alloy is near random [134]. It must be noted that the initial texture was already random which means that no texture evolution occurred during HPT processing of the nanocrystalline alloy [134].

The Oblique Cube component is the well-known Cube {001}<100> component (recrystallization texture) but rotated around the radial direction from the ideal position. This component is frequently observed in BCC alloys processed by HPT at a high deformation temperature as discussed in the next sections. In practice, the Cube grains undergo a rotation around the radial direction (becoming an Oblique Cube component) during further deformation [158]. This component appears as a consequence of stress-induced grain growth rather than due to static recrystallization. In fact, a strong grain growth is evident in nano-crystalline Pb pure processed by HPT at RT for large stains (ε_{eq}> 12) [159].

In addition, the texture intensity is twice sharper in the coarse grain alloy than in the nanocrystalline alloy [133]. The transition of the texture type can be correlated with the deformation mechanism operating during the HPT processing. The change of the texture when the initial grain size is about 20 nm is due to the shear banding, the partial activation of grain boundary sliding (GBS) and grain rotation accommodated by twinning and faulting [159]. In addition, texture simulation demonstrates that the resultant texture in the nanocrystalline alloy may result from the activation of the {111}<112> slip system, in addition to the usual operating {111}<110> slip system [134], while the dominant deformation mechanisms in coarse grain alloys are the activation of dislocations and may also include shear banding [159]. The absence of the development of any texture evolution up to strains of 12 when the initial grain size is below 20 nm is attributed to the domination of grain boundary meditated processes such as GBS [134]. Furthermore, it is expected that the texture will change by increasing shear strain at higher levels leading to the occurrence of grain growth and then an easy activation of dislocations. The saturation of grain size of single phase materials at high shear strains in HPT processing is independent of the initial grain size and specifically

whether it is coarser or finer [110]. This means that the grain size obtained in HPT-processed nanocrystalline material processed at high strain is approximately equal to the grain size obtained by deforming a coarse material processed at the same conditions. Hence, the differences in the saturation grain size of nanocrystalline materials depend strongly on the material purity and impurity content [110, 134]. Some questions remain open concerning the texture evolution: i) Will the texture be independent on the initial grain size at higher shear strains, as in the saturation regime? ii) Which type of texture will form at higher strains for materials with initial grain sizes below ~20 nm?

The texture is similar for HPT-processed pure Ni (weak *A*-fiber, strong *B*-fiber with the dominance of the *C* component) at N = 5 turns having initial grain sizes of 100 μm or ~350 nm resulting from prior ECAP processing (8 passes via route *Bc*) [122]. However, the deformation mechanisms and texture transition are reported at much lower grain sizes [110, 133, 134].

The shape of the grains also strongly affects the development of the texture during HPT processing. A typical shear texture is formed when the microstructure is composed of equiaxed grains, while a microstructure with elongated grains leads to the formation of shear texture with a dominance of the *C* component [160].

2.1.2.3.Effect of heat treatment before HPT processing

The effect of a preliminary heat treatment on the texture evolution was investigated for the Al-0.6Mg-0.4Si (wt.%), commercial AA6082 and Cu-0.86Cr (at.%) alloys [119, 120, 130]. Figure 8 presents the evolution of the texture of the Al-0.6Mg-0.4Si alloy under different initial conditions (solid solution treatment at 813 K for 2 h and quenched to RT, aged for 5 minutes at 473 and 523 K, respectively) [119]. The qualitative and quantitative aspects of the texture after HPT processing change with a

change in the annealing conditions. It is suggested that a preliminary annealing leads to the formation of precipitation that influences both the initial texture and the deformation texture. It is well known that precipitate particles can act as obstacles to the movement of dislocations and thereby change the deformation mechanisms which finally affects the deformation texture.

In order to confirm any correlation, Table 5 was developed based on the fundamental microstructural parameters of grain size and fraction of HAGBs, the microhardness and the texture evolutions reported for AA6082 [120] and Cu-0.86Cr [130] alloys during HPT processing. It is evident that the effect of precipitate particles on the microstructural parameters, microhardness and texture evolution depend strongly on the amount of shear strain. At low strains, only the nano-size particles (10 nm in length and 4 nm in diameter) form during the T6 aging and this causes a change of the texture from the typical shear texture of high γ_{SFE} materials to the dominance of the *C* component. In addition, the grain size and the fraction of HAGBs of the T6-aged sample are very small compared to the as-cast condition which contains large particles, where this is due to the pinning effect of the nano-size precipitates. At large strains, the texture, grain size, HAGBs and even the microhardness values of AA6082 and Cu-0.86Cr alloys are very similar in both conditions. Thus, the texture is similar to that reported at high shear strain in high (weak) and medium (stable texture) γ_{SFE} materials as discussed in section 2.1.2.1 and this indicates that the effect of particles is negligible at this stage of processing since most of these particles are dissolved under the high shear strain.

2.1.3. HPT processing deformation conditions

The fundamental parameters that can be modified during HPT processing are the applied pressure, rotation speed, deformation temperature and the number of HPT turns (which may be denoted also as the accumulated shear strain). At present, no investigations were carried out in order to highlight the effects of the applied pressure or the rotation speed on the texture evolution in FCC materials. Nevertheless, experimental results show that there is only a minor difference in the microstructure and mechanical properties evolution as a function of the applied pressure [15, 145, 161]. There is also evidence that the microstructural and mechanical properties variation of the HPT-processed materials originate from a combination of the shearing strain achieved in torsion and the compressive strain introduced by the imposed pressure [145].

In HPT processing, the dimensions of the disc sample also affect the microstructural and textural evolution since the accumulated shear strain is strongly dependent upon the thickness of the disc as shown in Figure 1c.

2.1.3.1.Effect of accumulated shear strain

Generally, and as discussed in section 2.1.2.1, the texture evolution of Al, Fe and high entropy alloys look similar with increasing shear strain. First, the shear texture starts gradually to form at low shear strain. Then, the shear texture weakens at high shear strain [54, 116-121, 129, 136]. By contrast, the texture of Ni and Cu-based alloys at high shear strain remains stable and exhibits no weakening with further increasing shear stain [72, 123, 127, 128].

The instability of the shear texture during the early stage of deformation is related to the complicated nature of the torsional deformation. In fact, the disc sample is continuously rotating during the entire torsional deformation and this causes an

instability and oscillation of the texture [162, 163]. For example, the initial A_2^* component of single crystal Ni transforms to the *C* component after HPT processing at ε_{eq} = 2–5 and then the *C* component transforms to A_1^* when ε_{eq} > 5 [125, 126]. Also, in polycrystalline materials (CP Al alloy) it is found that the $A/\bar{A}$ and A_1^*/A_2^* components rotate gradually to *C* and/or *B* components with increasing strain or numbers of HPT turns, as demonstrated in Figure 9 [116, 117]. The texture may further strengthen with increasing shear strain. In practice, the texture of the torsional deformation is very weak compared to other SPD processes such as ECAP [122]. At high shear strain, the texture of materials with high γ_{SFE} become weak due to grain fragmentation [116] where this fragmentation leads to the formation of sub-grains with different orientations from the parent grains and thus it should produce a texture weakening. In addition, decreasing the grain size to the nanometer scale favors the activation of GBS instead of dislocation slip and this tends to cause a randomization of the texture [127, 133, 134, 164].

As described in section 2.1.2.1, the stabilization of the texture at high shear strains for Ni and Cu-based alloys is related to their low stacking fault energy and slow recovery rate. In practice, the microstructural homogeneity in these materials requires the imposition of a higher shear strain than in materials having a high stacking fault energy [145]. To date, the maximum shear strain for which the texture was investigated in materials with medium γ_{SFE} is $\varepsilon_{eq} \approx 204$ (N = 10 turns) [127, 150]. Therefore, it will be interesting to investigate the texture and the corresponding microstructure produced above this strain for this category of materials.

The effect of the texture evolution on the mechanical properties was investigated in commercially pure Al after HPT processing at RT up to ε_{eq} = 25.1 (N = 3 turns) [138]. The results show the dominance of the *C* component causes a lowering of the fracture strain along the radial direction. As can be seen in Figures 10a and 10b, the

elongation to failure decreases with an increase in the volume fraction of the *C* component when the CP Al is processed by HPT up to ε_{eq} = 4.2 (N = 1/2 turn). It is apparent also that the texture weakening reduces the anisotropy along the radial and thickness directions as is readily evident from inspection of Figures 10c and 10d [138].

Several investigations attempted to correlate the texture evolution with the stored energy during HPT processing. Thus, there are some reports on HPT-processed Al and Ni materials indicating that the Taylor factor in grains with different shear texture components increase in the order of $A/\bar{A} < A_1^*/A_2^* < B/\bar{B} < C$ [116, 124, 138, 165]. It is accepted that a grain with a high Taylor factor has a higher dislocation density and consensually a high stored energy. However, it is necessary to emphasize that this hierarchy was first and only estimated for FCC materials deformed by simple shear [162] and to date there is no direct correlation between the stored energy and the Taylor factor. Generally, the Taylor factor may be regarded as an instantaneous measure of the dissipation of the plastic power per orientation and any selected strain mode and therefore technically it is valid only as an estimate of the stored energy if it is reasonable to assume that the strain path and texture remain constant [166].

The first direct correlation between the stored energy and the different shear texture components was recently reported for the Cu-.5Ni-0.6Si and Fe-36Ni alloys after HPT processing at RT up to N = 10 turns using the Kernel Average Misorientation (KAM) approach [157]. The results presented in Figure 11 demonstrate that HPT processing produces the same amount of stored energy in the different shear texture components (~24 J/mol) for the Fe-36Ni alloy and higher values (~35 J/mol) for the Cu-2.5Ni-0.6Si alloy. This is a consequence of the occurrence of CDRX in which the dislocation substructures develop homogenously and do not vary from grain to grain.

2.1.3.2.Effect of the examination position

An heterogeneity of the shear texture is observed with increasing distance from the disc center at low numbers of HPT turns in the Cu-2.5Ni-0.6Si (wt. %) alloy as shown in Figure 12 [72]. The shear texture is not developed near the centers of the HPT discs up to N = 1 turn due to the low strain. In practice, the equivalent strain imposed by HPT processing is heterogeneous across the HPT disc and increases with increasing radial distance from the center of the disc (see equation in Figure 1c). It worth noting also that most of the published texture results were obtained for HPT-processed materials under quasi-constrained conditions [167, 168].

In the constrained HPT disc, the torsion deformation is well defined in the region between 0.05 and about 0.9 of the radius of the HPT disc. At the edge of the disc (in the region of about 0.9 to 1), the axial direction experiences a very inhomogeneous deformation due to the constraining role of the anvils. In the center region, it is difficult to calculate an exact applied strain because of the inaccuracy of the determination of the exact center of the disc. It follows therefore that experimental data at the disc center must always be considered with caution.

However, the texture became more homogeneous and reaches a steady-state across the cross-sections of the HPT discs at high numbers of HPT turns up to N = 5 turns as shown in Figure 12. As can be seen from Figure 13, the texture homogeneity is consistent with the homogeneity of the microstructure and the mechanical properties as a function of distance from the disc center and the number of HPT turns [72, 150].

A similar texture tendency with increasing numbers of HPT turns is reported for HPT-processed pure Cu [128]. In addition, the volume fractions of the shear texture components are similar near the mid-radius and edge of HPT-processed pure Cu at N = 10 turns [127]. The occurrence of shear texture depends strongly on the measurement

position of the processed sample. For example, a typical shear texture is first developed at the edge of an Al processed sample shortly after N = 1/12 turn which corresponds to an equivalent strain of only ε_{eq} = 0.9 [117] whereas it is observed in the central area of the Al processed sample at N = 1/8 turn (ε_{eq} = 0.75) [116].

Several investigations report an independence of the microstructure and microhardness evolution with the distance from the center of the disc after a small number of HPT turns in several FCC materials including Cu [72, 169], Al [170] and Ni [171]. However, it is interesting to note that the texture and grain refinement reaches a steady-state at essentially the same high strain level as indicated in Figures 12 and 13. The evolution of the texture, microstructure and mechanical properties are a direct consequence of the character of the strain gradient due to the non-homogeneity of the HPT-processed samples which produces differences in the dislocation densities [172-174].

It should be noted that a net texture homogeneity across the disc was reported at low strains in commercially pure Al (N = 1/8 turn) [116] and in the AA 6082 alloy (N = 1 turn) processed by HPT [137] and this appears to be due to the effect of the high γ_{SFE}.

By contrast, a strong texture heterogeneity is observed along the axial direction, and therefore in the through thickness, of the Al (A5086) alloy, after HPT processing up to a rotation of 270° (N = 3/4 turn) with P = 1.2 GPa [175] as shown in Figure 14. The heterogeneity of the texture across the disc thickness was investigated also for pure Mg as an HCP material under the same HPT processing conditions [175] and the results are documented in section 2.3.4. It is worth noting that a strain heterogeneity through the HPT disc thickness is reported in relatively thick disc samples which are ten times thicker (8 mm) [176] and four times thicker (3 mm) [175] than the disc samples usually employed in HPT processing (0.8 mm). In thin HPT discs (0.8 mm), the microhardness

of pure Al is stable through the thickness even at low strains (N = 1/4 turn) [177]. In the case of thicker HPT discs, the strain heterogeneity is essentially localized in the middle plane section [175, 176]. It is claimed that homogenous mechanical properties are achieved when using a suitable geometric ratio in terms of the thickness to diameter of the HPT disc [32]. Although a systematic study was not performed on texture evolution, it is generally believed that a texture homogeneity may be achieved together with the mechanical properties.

2.1.3.3.Effect of deformation temperature

Only limited information is available at present documenting the effect of deformation temperature on texture development in the Fe-36Ni (% wt.) alloy [54] and pure Ni after HPT processing [124]. The Fe-36Ni alloy was processed at RT and 523 K for N= 1/2, 1, 5 and 10 turns and the texture was measured at the mid-radius of the discs using EBSD measurements [54]. The results show that almost all shear components except the A_2^* component start gradually to form at RT between N = 1/2 and 1 turn corresponding to ε_{eq} = 5–10. The texture is weak and stable upon increasing the amount of processing to N = 5 and 10 turns equivalent to ε_{eq} = 50–100 and this is associated with the enforcement of the *B* component but nevertheless a strong typical shear texture develops soon after N = 1/2 (ε_{eq} = 5) when the alloy is processed at 523 K. At this temperature, increasing processing from N = 1 to 10 turns causes a weakening of the shear texture except for the dominance of the *C* component. This texture difference is attributed to dynamic recovery rather than dynamic recrystallization at 523 K [54] where dynamic recrystallization is excluded for two reasons. First, a temperature of 523 K (~$0.3T_m$) is lower than the effective temperature of ~873 K (~$0.5T_m$) for recrystallization and grain growth [178]. Second, it is expected that the *A* and $\bar{A}$

components strengthen by consuming the *C* component during the occurrence of dynamic recrystallization [127, 179] and this is not observed in the present case.

The texture difference was also discussed in terms of the evolution of the texture index as a function of the numbers of HPT turns as shown in Figure 15 [54] which presents the evolution of texture strength of the Fe-36Ni alloy under both conditions as a function of the number of HPT turns.

In practice, the alloys exhibit significantly different behaviors. Thus, the texture of the alloy processed at RT first decreases because of the gradual formation of a shear texture at low strain and then increases after N = 5 and slightly decreases after N = 10 turns due to the grain refinement. The texture index of the Fe-36Ni alloy processed at 523 K continually decreases with increasing numbers of HPT turns and this indicates that the texture weakens. It is noted that between N = 1/2 and 1 turn the texture of the alloy processed at 523 K is stronger than for the alloy processed at RT. This tendency is reversed after higher numbers of HPT turns, for example up to N = 5 turns. These differences are mainly attributed to the different microstructural evolutions in grain size and grain boundary misorientation during deformation in these two deformation conditions as presented in Table 6 [54].

In practice, the grain refinement mechanism as given by the activation of dislocations and their accumulation and rearrangement to form sub-grain boundaries (CDRX) is slower in the alloy processed at RT as demonstrated in Table 6 [54]. The grain size is smaller and the fraction of HAGBs is higher after processing at 523 K than at RT. These differences account for the rapid formation of a typical shear texture in the alloy processed at 523 K at lower numbers of HPT turns as at N = 1/2 versus N = 5 turns at RT, and thereafter there is a continuous weakening of the texture with

increasing numbers of HPT turns [54]. The gradual transformation of LAGBs into HAGBs creates a larger spread in orientations between the neighboring grains [123].

In pure Ni processed by HPT at T = 77 and 300 K ($0.17T_m$) for N = 10 turns, a typical shear texture composed of a weak *A*-fiber, a full *B*-fiber and a strong *C* component is formed [124]. Increasing the deformation temperature to 523 and 673 K ($0.3T_m$ to $0.38T_m$) leads to the disappearance of the *C* component and the formation of a new component named the Oblique Cube, as demonstrated in Figure 16 [124].

In addition, isothermal annealing at 448 K of the disc processed at 300 K shows that the Oblique Cube component is related specifically to the abnormal growth of grains [124]. The main conclusions of this latter work are that the stored energy and oriented nucleation provide the source for recrystallized grains while the oriented migration of grain boundaries determines the sharpening or weakening of the different texture components [124].

2.1.4. Recrystallization texture of HPT-processed FCC materials

Investigations of the static recrystallization process and thermal stability of HPT-processed materials are of great interest because it is important to retain the ultra-grain refinement and high strength during the annealing treatment. In practice, static recrystallization can take place by discontinuous or continuous mechanisms [180]. The discontinuous static recrystallization (DSR) consists of the formation of nuclei and their subsequent growth which is characterized by a heterogeneous microstructural evolution and a rapid softening during annealing. Continuous static recrystallization (CSR) includes the continuous transformation of LAGBS into HAGBs and this leads to homogeneous microstructural coarsening and a continuous decrease in strength during annealing. In SPD-processed materials, HAGBs already form during deformation due to

the occurrence of CDRX. However, these HAGBs formed during SPD processing are in a non-equilibrium state and they may be transformed into equilibrium HAGBs by recovery and short-range migration of boundaries with further application of an annealing treatment [106]. In this case, the static recrystallization of SPD-processed materials is a continuous type (CSR) [106]. However, a transition from CRS to DSR is reported in HPT-processed BCC materials under annealing conditions as will be shown in section 2.2.3.

Even if the thermal stability and the evolution of mechanical properties after isothermal or isochronal annealing of HPT-processed FCC materials were more widely examined and reported, it is important to note that only very limited data are at present available concerning the recrystallization texture in HPT-processed Ni alloys [139, 181].

In the first report on this topic, it is claimed that the shear texture formed during HPT processing at RT through N = 5 turns of pure Ni transforms into four different fibers designated as (001), (111), (112) and (103) during isothermal annealing at 573 K ($0.33T_m$) for 1, 10 and 30 minutes in an Ar atmosphere [139]. In fact, these four fibers were not critically defined in this report but nevertheless it is important to recognize that this is the first report dealing with the evolution of texture after HPT processing and it was published at a time when the evolution of texture after HPT processing was not generally studied and it was not understood.

The second report investigated the evolution of the recrystallization texture of HPT-processed Ni (99.967% (4N) and 99.5% (2N) purity) after isochronal annealing from 373 to 873 K (from $0.21T_m$ to $0.5T_m$) for 1 hour [181]. First, the alloys were HPT-processed at RT to ε_{eq} = 100 without any indication of the precise numbers of HPT turns. Then the effect of impurities was investigated by measuring the microstructure,

microhardness and texture at different stages of softening: in the as-deformed state, the recovered state, the recrystallized state and after grain growth as summarized in Table 7. The similarities in the deformation textures of both alloys demonstrates that the impurities have only a minor influence during HPT processing. However, their effect is more pronounced during recrystallization and grain growth processes where the recrystallization texture of the 4N Ni alloy changes from a typical shear to a near-random texture while the recrystallization texture of the 2N Ni alloy is retained. The evolution of microstructure and microhardness are also different in both of these samples. The recovery and recrystallization kinetics are significantly delayed in the 2N Ni alloy due to the presence of impurities and their effect on the dislocation annihilation and grain boundary migration [181]. Moreover, the presence of impurities significantly modifies the static recrystallization mechanisms. The modification of the texture and microstructural parameters during isochronal annealing of the 4N Ni alloy is an indication of the occurrence of DSR and the retained texture and the change of the microstructural parameters and microhardness values after the grain growth process in the 2N Ni alloy demonstrates that the alloy undergoes a discontinuous and continuous static recrystallization simultaneously [181].

Considering the limitations on the available data, it would be interesting to focus more directly on the evolution of the recrystallization texture for different FCC materials in order to develop a reasonably comprehensive analysis of the static recrystallization mechanism.

2.2.Texture evolution after HPT processing of BCC materials

2.2.1. Ideal shear texture components for materials with a BCC structure

The main ideal shear texture components for BCC materials are listed in Table 8 [114, 182] and they are illustrated by ODF sections at φ_2 = 0° and 45° and {110} pole figures projected onto the SD-RD, SD-CD and CD-RD planes as shown in Figure 17.

The shear texture for BCC materials is characterized by the formation of two fibers. The first fiber is {110}//SP or SD-RD plane and contains the *F*, *J*, $\bar{J}$, *E* and $\bar{E}$ components. The second fiber is {hkl}<111> and contains D_1, D_2, *E* and $\bar{E}$ components. In some reports the *J*, $\bar{J}$, *E* and $\bar{E}$ components are designated as J_1, J_2, E_1 and E_2, respectively [183, 184].

Only limited investigations on the evolution of BCC materials after HPT processing are available at present. Nevertheless, in the following the evolution of the texture is discussed as a function of the deformation conditions such as the deformation temperature and shear strain, the measurement position and finally there is a discussion and more detailed analysis of the recrystallization texture of HPT-processed BCC materials.

2.2.2. HPT processing deformation conditions

2.2.2.1.Effect of deformation temperature

It is remarkable to note that the majority of the HPT processing of BCC materials was conducted at a high temperature [184-186] and/or the texture evolution was investigated as a function of increasing deformation temperature [187-191] where this is mainly due to the brittle character of these materials which arises from the lack of easy dislocation movement at low deformation temperatures. In these high temperature conditions, dynamic recrystallization and phase transformations play an increasingly

important role during the texture development [187-191]. For example, the textures at the edge of an intermetallic NiAl disc HPT-processed at RT and at 373 ($0.2T_m$), 573 ($0.3T_m$) and 773 K ($0.4T_m$) for N = 2 turns, equivalent to ε_{eq} = 34.6, are reported as very different [188, 189]. Thus, at RT all shear components (the F, J, $\bar{J}$, E, $\bar{E}$, D_1 and D_2 components) are developed and they lead to the formation of a typical shear texture in BCC materials as shown in Figure 18. At a high deformation temperature an Oblique Cube component dominates the texture with a weak *F* component. As noted earlier, the Oblique Cube is a Cube component that undergoes a rotation around the radial direction and then develops through discontinuous dynamic recrystallization [158].

This texture difference at different temperatures may be explained by the activation of different secondary slip systems during processing at RT which causes the formation of different shear texture components whereas the onset of dynamic recrystallization during hot processing leads to the formation of an Oblique Cube component. However, the Oblique Cube component is observed in the YCu intermetallic [189] and in a Ti-45Nb (wt. %) alloy processed by HPT at RT [192]. Furthermore, the Oblique Cube component is also reported in the central region of an $Ni_{50}Mn_{90}Ga_{21}$ disc after HPT processing at ε_{eq} = 3 at temperatures below 973 K [187]. It is noted that the texture transforms to strong Cube and weak *F* components above 973 K where this corresponds to the phase transition $B_2 \rightarrow L_{21}$ (1020 K).

Pure materials such as tungsten (W) [190] and tantalum (Ta) [191] exhibit similar texture evolution as a function of deformation temperature. Figure 19 shows that all shear components of BCC materials are formed in the HPT processing of pure Ta for N = 10 turns, equivalent to ε_{eq} = 136, at all of the deformation temperatures of 77 ($0.02T_m$), 298 ($0.09T_m$), 673 ($0.2T_m$) and 773 K ($0.23T_m$) and it is also observed that their intensity decreases with increasing deformation temperature due to the recovery

process [191]. Nevertheless, an increased spread of the components is reported at elevated deformation temperatures. This behavior is explained by the change in the recovery processes from predominantly mechanically-induced boundary migration to a thermally-induced boundary migration [124, 191].

By contrast, the addition of 1 wt.% of La_2O_3 particles in pure W (W-1La_2O_3, WL10) gives a different texture evolution [190]. Thus, HPT processing for N = 2 turns, equivalent to ε_{eq} = 22, between 473 (0.12T_m) and 673 K (0.18T_m) of W-1La_2O_3 leads to the formation of a γ-fiber containing *E* {111}<110> to *F* {111}<112>. Increasing the deformation temperature between 673 and 973 K (0.26T_m) causes a considerable decrease in the γ-fiber and the formation of *A* {112}<111>, *J* {110}<112> and *G* {110}<001> components [190]. This is explained by firstly noting that the γ-fiber forms at a low deformation temperature through the effect of the La_2O_3 particles on the dislocation motion and by lowering the γ_{SFE} the DRX is retarded and secondly by developing a particle-stimulated nucleation (PSN) mechanism [186, 190]. Increasing the deformation temperature renders dynamic recrystallization easier which explains the formation of the *A* {112}<111>, *J* {110}<112> and *G* {110}<001> components.

2.2.2.2.Effect of hydrostatic pressure

The influence of applied hydrostatic pressure on the texture evolution was investigated near the edge of an NiAl disc after HPT processing at RT and 773 K (~0.5T_m) up to N = 2 turns, equivalent to ε_{eq} = 34.6 [193]. The results demonstrate that the volume fraction of all shear components except the D_2 component form in the disc processed at RT and increase with increasing applied hydrostatic pressure from 4 to 8 GPa. However, the volume fraction of the Oblique Cube formed in the disc processed at 773 K decreases continuously with an increase of the applied hydrostatic pressure from

2 to 8 GPa. It appears that the change in volume fraction of the shear texture components at RT may be attributed to the change in activity of the different secondary slip systems with changes in the applied pressure, whereas at a high deformation temperature an increase in the applied pressure effectively delays the onset of recrystallization or grain growth [193].

2.2.2.3.Effect of accumulated shear strain

The intensity of the *A* {112}<111>, *J* {110}<112> and *G* {110}<001> components increases with increasing shear strain from ε_{eq} = 5.43 for N = 1/2 turn to ε_{eq} = 21.7 for N = 2 turns and then decreases after ε_{eq} = 43.5–87 for N = 4–8 turns in HPT-processed pure W at 673 K ($0.18T_m$) [186]. Furthermore, the texture of HPT-processed WL10 exhibits different trends with increasing shear strain [186]. In these experiments the *A* {112}<111> and *G* {110}<001> components form first after ε_{eq} = 5.43 and, by increasing the shear strain to 10.8–21.7 for N = 1–2 turns, there is the formation of a γ-fiber. Finally, the γ-fiber disappears and the *A* {112}<111>, *J* {110}<112> and *G* {110}<001> components appear again after ε_{eq} = 43.5 for N = 4 turns [186]. In this latter work a scheme is proposed composed of the three deformation stages, as shown in Figure 20, to explain the microstructural and textural changes during HPT processing of W and WL10 alloys at 673 K [186].

A work hardening occurs at stage I, where this is $\varepsilon_{eq} < 9$ for a W alloy and $\varepsilon_{eq} <$ 24 for a WL10 alloy, and this leads to a lamellar microstructure, the generation of dislocations and rapid grain refinement. During this stage, HPT processing changes the initial texture of both alloys and this leads to the formation of typical shear components of *A* {112}<111>, *J* {110}<112> and *G* {110}<001> due to the shear nature of the HPT processing. In addition, a *γ*-fiber forms in the WL10 alloy due to the occurrence of PSN

near La_2O_3 particles. A softening occurs during stage II, corresponding to $9 < \varepsilon_{eq} < 68$ for the W alloy and $24 < \varepsilon_{eq} < 68$ for the WL10 alloy, owing to dislocation annihilation in both alloys which is associated with the operation of DRX. At this stage, the elongated grains transform to an equiaxed shape which is related to the transformation of LAGBs to HAGBs. The texture of the W alloy is maintained through the presence of the *A*, *J* and *G* components due to the occurrence of continuous DRX [194]. A texture transition is observed in the WL10 alloy with the dominance of the γ-fiber, thereby demonstrating the occurrence of discontinuous DRX [194].

At stage III where $68 > \varepsilon_{eq}$, there is a clear difference between the W and WL10 alloys. Thus, the W alloy exhibits a saturation state including a saturation in the grain refinement. Nevertheless, grain rotation is possible and this leads to texture weakening in the W alloy. A flow localization composed of nanocrystalline arrays and microstructure coarsening in the adjacent areas is observed at high shear stains in the W alloy as is evident in Figure 20 and this is explained by the presence of impurities, nano-cracks, and/or through the presence of a plastic instability. It is found also that the *γ*-fiber dominates the texture of this nanocrystalline array due to the change in slip plane of the dislocations from {110} and {112} to {111}. For the WL10 alloy, the La_2O_3 particles undergo a refinement at stage III which leads to the activation of dispersion hardening, the disappearance of the *γ*-fiber and the dominance again of the *A*, *J* and *G* components.

2.2.2.4.Effect of the measurement position

It is readily evident from inspection of Figure 21 that the use of HPT processing to compact Fe powder into a solid disc causes the formation of three regions throughout the thickness. These regions may be defined as (1) an undeformed region (named U-

zone) corresponding to the top part from the disc in contact with the fixed punch, (2) an intermediate or transition region (named T-zone) where the shear strain increases and (3) a severely deformed region (named S-zone) which is the part of the disc in contact with the lower rotating anvil in the bottom part of the HPT processing facility. The texture of the undeformed region is very weak and nearly random and gradually it transforms to a typical shear texture with increasing shear strain in the T and S-zones. It is obvious that the evolution of the microhardness throughout the thickness follows similar trends as for the texture evolution as shown in Figure 21. However, there is unfortunately an overall lack of any systematic evaluations of the texture, microstructural and mechanical properties in BCC materials after HPT processing and this demonstrates that further investigations are needed to correlate the grain refinement, mechanical properties and the overall texture evolution.

2.2.3. Recrystallization texture of HPT-processed BCC materials

A transition of the static recrystallization from a continuous to a discontinuous manner above 873 K (~$0.5T_m$) was demonstrated in an Fe-9Cr (wt.%) alloy processed by HPT at 573 K ($0.3T_m$) for N = 10 turns, equivalent to ε_{eq} = 120, during isochronal annealing from 773 to 973 K for 48 hours [195]. The φ_2 = 45° ODF section shown in Figure 22 demonstrates that all BCC shear components developed during HPT processing disappear except for the dominance of the $J/\bar{J}$ components during annealing at 873 K for 6 and 24 hours [184].

The results presented in Figure 23 demonstrate that grains with the $J/\bar{J}$ orientation have the highest stored energy and they are surrounded by special coincidence site lattice (CSL) boundaries such as Σ9 (20.1°<110>) and Σ33a (38.9°<110>), as illustrated in Figure 23b, that lead to their rapid and fast

recrystallization and growth by comparison with other oriented grains during annealing [184].

The evolution of recrystallization below 873 K was not reported in this investigation but nevertheless it is generally expected that the deformation texture will be retained. This is confirmed by the retained texture reported for HPT-processed W and WL10 at 673 K for N = 4 turns after annealing at 1273 K up to 6 hours [186]. This is a consequence of the high melting temperature of the materials where the recovery of defects and recrystallization processes require relatively high temperatures [191]. In addition, the texture during the annealing treatment is more stable in the WL10 alloy than in pure W. It is worth noting that the stabilization of texture and microstructure during the annealing treatment results from a continuous static recrystallization mechanism due to the high fraction of HAGBs in the as-deformed W and WL10 alloy. The pinning effect of the La_2O_3 particles on the grains boundaries is also a significant factor in stabilizing the texture of the processed WL10 alloy.

2.3.Texture evolution after HPT processing of HCP materials

2.3.1. Ideal shear texture components for materials with HCP structure

The ideal positions and fibers of materials with HCP structure subjected to simple shear were recently evaluated using the Viscoplastic Full Constraints Crystal Plasticity Approach [196]. Five fibers were identified and labeled *B*, *P*, *Y*, C_1 and C_2. Their ideal positions in the ODF sections at $\varphi_2 = 0°$ and 30° and {0002} and $\{10\bar{1}0\}$ pole figures projected on the SD-RD, SD-CD and CD-RD planes are shown in Figure 24 and Table 9. It is found that the persistence and the stability of these fibers depend strongly on the activation of different slip and twinning systems and hence on the c/a ratio of the material, where *c* and *a* are the fundamental lattice parameters. For example,

the presence of *B*, *P* and *Y* fibers corresponds with a high activation of the <a> basal slip system while the activation of the <c+a> pyramidal slip system leads to the formation of C_1 and C_2 fibers [196].

It appears that HPT processing is the only SPD processing technique that may be used effectively to produce excellent grain refinement in difficult-to-deform HCP materials such as Mg-based alloys by processing at room temperature [197]. Thus, processing by HPT may be used to prevent the cracking and to suppress the development of internal fragmentation which are inherent fracturing processes occurring in other SPD processing techniques such as ECAP [198, 199]. There are several investigations dealing with the evolution of microstructure, the mechanical properties and the texture of HPT-processed HCP materials, especially for a range of Mg-based alloys. In the following section, the evolution of the texture in HCP materials is discussed as a function of the initial condition of the material, the deformation conditions and finally the evolution of the recrystallization texture.

2.3.2. Effect of initial conditions of HCP materials

2.3.2.1.Effect of c/a parameter and alloying elements

It is well established that the deformation textures of HCP materials are different after processing by conventional rolling where these differences depend upon the c/a ratios of the material. The results may be divided into 3 distinct categories: 1) c/a < 1.633 such as Ti where c/a = 1.587, 2) c/a ≈ 1.633 such as Mg where c/a =1.624 and 3) c/a > 1.633 such as Zn where c/a = 1.856 [200].

In general, the c/a ratio reveals the activation of the different slip and twinning systems. The resulting texture for materials with c/a > 1.633 is attributed to a combination of basal <a> slip and mechanical twinning while the prismatic <a> and

pyramidal <c+a> slip systems are responsible for texture formation in materials with values of c/a lower than 1.633 [200].

A comparison of the texture formation in pure Ti [201], Mg [202] and Zn [203] after similar HPT processing at N = 5 turns is shown in Figure 25. It is readily apparent that the three pure materials exhibit essentially the same typical *B*-fiber even though their c/a ratios are different. Nevertheless, it appears that the sharpness of the *B*-fiber increases with increasing c/a ratio.

In practice, the majority of HCP materials processed by HPT exhibit a *B*-fiber due to the easy activation of the <a> basal slip system at RT compared to the other non-basal systems and the basal planes oriented parallel to the shear plane produce a typical basal *B*-fiber texture. By contrast, the presence of alloying elements may have a significant influence on the distribution of the basal poles and their intensity. For example, HPT processing at RT up N = 10 turns for the Mg-1.44Ce and Mg-1.43Nd (wt. %) alloys leads to the formation of a weak and asymmetric basal texture (*B*-fiber) having a "crescent" form unilaterally shifted about 15° towards SD [204]. Another example concerns the texture of the ZK60A (Mg-6Zn-0.5Zr, wt.%) alloy which is characterized by a shift of the basal poles towards SD which leads to the formation of a *Y*-fiber after HPT processing at RT through N = 1/2 turn [205]. However, increasing the numbers of HPT turns up to N = 5 turns permits the formation of a typical *B*-fiber texture in the ZK60A alloy [206].

The general weakening and the altering of the texture with the presence of alloying elements such as rare earth (RE) elements is associated with the grain boundary pinning effects caused by solute segregation and precipitate particles and by the activation of non-basal slip through a modification of the stacking fault energy of the Mg matrix [10, 204, 207, 208].

2.3.2.2.Effect of initial texture

The effect of the initial texture on the texture development during HPT processing was first investigated in Mg single crystals [209]. Two Mg single crystals were prepared from two different orientations: <10$\bar{1}$2>//CD and <11$\bar{2}$2>//CD. The samples were then processed under a pressure of 1.5 GPa through N = 0.1, 0.2, 0.3 and 1/2 turn and the texture was recorded using X-ray diffraction (XRD) across the disc radius [209]. The results demonstrate that the <10$\bar{1}$2>//CD named as the soft orientation transforms rapidly to a *B*-fiber with increasing shear strain while the <11$\bar{2}$2>//CD is named as the hard orientation because this orientation remains stable and unchanged with increasing shear strain [209].

The effect of the initial texture on the texture evolution after HPT processing was also investigated in two types of polycrystalline CP Mg [67]. The first was CP Mg in an as-cast condition where the microstructure exhibits coarse grains larger than 1 mm and a random texture. The second was CP Mg in an as-extruded condition where the microstructure is more refined with a grain size of ~50 μm and where this material exhibits a typical extrusion texture where the <0002>//ED (where ED is defined as the extrusion direction) [67]. The texture was measured using neutron diffraction at the center, middle and edge of the HPT-processed discs to N = 1/8, 1/4, 1/2, 1, 4 and 8 turns and the results show that in all HPT-processed discs a typical shear texture is formed of *B*-fiber (basal texture) with a 15° deviation from their ideal position [67]. However, there are some differences in the texture evolution because the *B*-fiber is formed rapidly after N = 1/8 (disc center) in the as-extruded CP Mg compared with after N = 1 turn (disc center) in the as-cast CP Mg. In addition, the texture intensity is weak in the as-extruded CP Mg compared to the as-cast condition. The rapid formation of the *B*-fiber in the as-extruded CP Mg is attributed to the activation of tensile twins that produce a

rotation about 86.3° of the basal plane which is perpendicular to the shear direction in the initial texture and to a direction parallel to the shear direction after N = 1/8 turn of HPT. The presence of twins is readily evident from microstructural observations. Furthermore, the evolution of the texture in the early stage of deformation in the as-cast CP Mg is explained by the presence of the pyramidal <c + a> slip systems. It is claimed that the formation of a double texture shown in the {0002} pole figure of the as-cast PC Mg processed at N = 1/8 turn (as presented in Figure 26) is an indication of the activation of the pyramidal <c + a> slip together with basal slip [67].

2.3.2.3.Effect of heat treatment before HPT processing

The resulting texture after HPT processing at RT for N = 3 turns of an Mg-Dy-Al-Zn-Zr alloy is strongly dependent on the pre-heating treatment before HPT processing [210]. The EBSD measurements show that the HPT processing leads to the formation of a *P*-fiber in the un-aged disc. Aging at 523 K for 16 hours causes the formation of *P*-fiber, *B*-fiber and C_2-fiber. By contrast, the texture of the processed disc aged at 573 K for 16 hours shows the presence only of the C_2-fiber [210]. It is interesting to note that all samples exhibit a random texture before HPT processing [210]. It is claimed that the formation of the *P*-fiber is a result of the activation of <a> basal slip and the C_2-fiber is formed due to the activation of only the <c+a> pyramidal slip system. Hence, the formation of these three fibers corresponds to the activation of various slips systems such as <a> basal and <c+a> pyramidal slip during HPT processing. The change in the activation of the slip systems is related to the grain refinement and to the formation of precipitates during annealing before HPT processing. Although results are presented for the distribution of the precipitates ($Mg_{30}DyZn$ and $Al_6Mg_2Dy_3$ phases) in the as-cast (un-aged) sample, nevertheless there is no

presentation of the microstructural changes and precipitate evolution as a function of the annealing treatment.

2.3.3. HPT processing deformation conditions

2.3.3.1.Effect of deformation temperature

The texture evolution of an as-extruded AZ31 alloy was investigated after HPT processing at 296 ($0.3T_m$), 373 ($0.4T_m$) and 473 K ($0.5T_m$) for N = 1 and 5 turns using the XRD technique [211]. The {0002} pole figures and ODF at the φ_2 = 30° section show the formation of the *B*-fiber with some deviations from their ideal positions and a second fiber, tentatively identified as the C_1-fiber, for discs processed at 296 and 373 K for N = 1 and 5 turns. It is interesting to note that this second fiber vanishes with increasing numbers of HPT turns when the discs are processed at 373 K, as demonstrated in Figure 27. The presence of the second fiber is considered as the transformation state from the as-extrusion texture to the basal due to the activation of tension twinning $\{10\bar{1}2\}<10\bar{1}\bar{1}>$ [211]. Processing at 473 K leads to the formation of a typical *B*-fiber with a complete disappearance of the second fiber in both processed samples after N = 1 and 5 turns. In addition, it is observed that the deviations of the basal fiber from their ideal position decrease with increasing deformation temperature [211]. The formation of a stable basal texture at a high deformation temperature is attributed to a recovery process and the activation of non-basal slip systems such as <c + a> pyramidal slip since their critical resolved shear stress (CRSS) decreases with increasing temperature [212].

2.3.3.2.Effect of hydrostatic pressure

The influence of applied hydrostatic pressure on the texture evolution was investigated across the radius in the CD-SD plane of pure Mg with two different initial textures of a random and extrusion texture after HPT processing at RT up to N = 4 turns [209]. Another investigation showed the evolution of the texture of as-extruded pure Mg as a function of the applied hydrostatic pressure after HPT processing to different shear strain levels [213]. The results demonstrate that, whatever the initial texture and the shear level, a basal fiber is formed and the applied hydrostatic pressures of 1, 2 and 4 GPa produce only a minor effect on the texture intensity in which the texture weakens with increasing applied hydrostatic pressure [209, 213] (as shown in Figure 28).

In the case of Ti-based alloys, increasing hydrostatic pressure during HPT processing induces a phase transformation such as the α→ω phase transition [201, 214]. The orientation relationship between the α-phase and HPT-induced ω-phase is given as: $(0001)_\alpha \| (11\bar{2}0)_\omega ; [11\bar{2}0]_\alpha \| [0001]_\omega$ [201]. A phase transformation under HPT processing should significantly affect the texture evolution. However, until now there is no reports dealing with the evolution of the texture under such conditions. Furthermore, it is found that the formation of a basal fiber in the α- phase facilitates the α→ω phase transition under HPT processing [201, 214].

2.3.3.3.Effect of accumulated shear strain (number of HPT turns)

From a general point of view, the evolution of the texture in HCP materials is expressed as a function of the number of HPT turns rather than the equivalent shear strain. Table 10 summarizes the evolution of the texture as measured in the centers of some HCP-processed alloys as a function of the numbers of HPT turns [67, 68, 202-204, 215]. For any accurate comparison, it is important to note that the presently

discussed texture features relate to the centers of the processed discs. Obviously, the deformation texture is a *B*-fiber in most alloys formed in the early stages of deformation and this appears to saturate with increasing numbers of HPT turns. An HPT-processed pure Zn develops a very sharp *B*-fiber compared to Mg-based alloys [203] because of its low recrystallization temperature (~261 K) [216]. The intensity and the distribution of the basal texture may be altered with increasing shear strain as in the AM60 alloy caused by the precipitation of the $Mg_{17}Al_{12}$ phase during HPT processing [215]. The changes in the texture distributions have an apparent effect on the shear stress maxima of the stress-strain curves as indicated in Figure 29. In this case, the texture is presented by means of inverse pole figures in the normal direction of the disk surface (compression direction). The formation of the *B*-fiber during tensile testing after HPT produces a very low Schmid factor for basal slip and hence non-basal slip systems with significantly higher CRSS necessarily operate and this leads to an obvious increase in the yield stress.

Figure 30 presents the evolution of microhardness and texture as a function of equivalent strain for pure Ti [217], Mg-0.41Dy [68] and a Zn-0.5Cu (wt.%) [218] alloy in order to verify any correlation between the hardening models and texture evolution as described for FCC materials in section 2.1.2. It is noted that no information is available concerning the evolution of the texture as a function of the number of HPT turns in Ti-based alloys. However, based on the X-ray diffraction patterns for HPT processed Ti-6Al-7Nb alloy a basal fiber may form after N = 1 and 3 turns and a decrease of the intensity of the (0002) peak is evident after N = 5 turns indicating a change in the texture [219].

Figure 30 shows that the c/a ratio strongly affects the hardening behavior of HCP materials. Thus, the Zn-0.5Cu alloy with c/a > 1.63 undergoes a strain softening

rather than strengthening due to recrystallization and grain growth during HPT processing (Figure 30d). The increase of grain size in Zn-based alloys during HPT processing is similar with an increase in the *B*-fiber intensity [203, 218]. By contrast, the evolution of the *B*-fiber as a function of the equivalent strain, or the numbers of HPT turns, is independent of the hardening behavior. The increase in the texture intensity in both the Mg-0.41Dy and Zn-0.5Cu alloys (Figures 30c and 30e) is essentially a consequence of the contribution of the dynamic recrystallized grains which have the same texture as the deformed grains. However, the direct relationship between the texture evolution and the hardening behavior of materials with high c/a value requires further investigations.

Very recently, it was demonstrated that texture strengthening contributes strongly in the rapid strengthening of HCP materials, especially in the early stage of SPD processing as in ECAP, HPT and multi-directional forging (MDF) [67, 68, 81, 203, 215]. In addition to the contribution of grain size hardening and dislocation hardening to the yield strengthening, σ_y, texture strengthening was recently added as a correction factor (M_t/M_R) as in the following relationship [81]:

$$\sigma_y = \frac{M_T}{M_R}\left(\sigma_0 + \alpha_1 M_R G b\sqrt{\rho} + \frac{k_{HP}}{\sqrt{d}}\right) \quad (3)$$

where M_T is the Taylor factor estimated for the deformed sample, M_R is the Taylor factor for a random texture, σ_0 is the friction stress, α_1 is a constant, G is the shear modulus, b is the average Burgers vector, ρ is the dislocation density, k_{HP} is the Hall–Petch constant and d is the mean grain size.

Figure 31 compares the calculated yield strength from equation (3) with the measured value for the AM60 alloy processed by ECAP, MDF and HPT [215] and for the Mg-0.41Dy (wt.%) alloy processed by HPT [68]. A good correlation is obtained between the calculated and the measured yield strength values for the Mg-0.41Dy alloy

but there is a less good correlation for the AM60 alloy after HPT processing probably due to the occurrence of precipitation strengthening of the $Mg_{17}Al_{12}$ phase during HPT [215]. In addition, the determination of the Taylor factor M_t was simplified by considering only the <a> basal slip system although it is known that other slip systems may contribute to the deformation during testing [215]. This means that careful attention must be directed to simulating the Taylor factor and the extent used in equation (3) for various HCP materials and even correspondingly for FCC and BCC materials.

2.3.3.4. Effect of the measurement position

Figure 32 presents the basal {0002} pole figures near the center, middle and the edge of discs of the Mg-0.41Dy (wt. %) alloy processed by HPT at RT to N = 1, 5 and 15 turns [68]. It is observed that the texture is not homogenously distributed across the disc radius. Thus, the *B*-fiber deviates by about 15° from CD with increasing distance from the centers of the discs and it is observed that the texture of pure Mg is more homogenous across the disc radius with increasing numbers of HPT turns [67, 202]. Moreover, the texture is not homogenously distributed in the Mg-0.41Dy alloy even at high numbers of HPT turns where N = 15 turns. This difference is attributed to the effect of alloying elements on the deformation mechanisms as discussed in section 2.3.2.1.

In earlier reports [209, 213, 220], the deviation of the basal pole is explained by the occurrence of dynamic recrystallization during HPT processing and static recrystallization after HPT processing as in natural aging. However, Figure 33 shows clearly that recrystallization is not the main reason for this deviation since the microstructure of an Mg-0.41Dy disc processed to N = 1/2 turn shows a very weak

fraction of DRX, denoted by the blue grains, and the observed deviation remains even after N = 5 turns where 58% of the grains are dynamically recrystallized [68]. Furthermore, the corresponding {0002} pole figures indicate that the orientations of the deformed grains have already deviated from the ideal *B*-fiber position shortly after N = 1/2 turn.

This deviation of the basal texture can be attributed to the shear deformation or torsional straining that is imposed by the rotation of the anvil during HPT processing. As demonstrated in Figure 34b, the basal fiber is formed in the as-extruded AZ60A alloy (Figure 34a) during compression without torsion straining whereas HPT processing at N = 1/2 turn causes a deviation of the basal pole away from its ideal position (Figure 34c) [205].

It is expected that the texture of HCP materials will be heterogeneously distributed along the axial direction and across the thickness of HPT-processed discs even when the discs are very thin (~0.8 mm) since there are variations in the microhardness in the through-thickness directions of the AZ31 (Mg-3Al-1Zn, wt.%) alloy after processing at RT (296 K) and 463 K up to 5 turns with an applied pressure of P = 6.0 GPa [221, 222]. The microhardness distributions shown in Figure 35 demonstrate that the strain is localized towards the bottom of the discs. These observations are different from those reported for pure Al [177] and this is attributed to the difference in the grain refinement mechanisms in FCC and HCP materials [221, 222]. In practice, grain refinement in FCC materials occurs by the gradual transformation of LAGBs into HAGBs upon subsequent increases in the strain whereas in HCP materials the nucleation of new fine grains is located along the existing grain boundaries of the initial coarser structure leading to the development of a bimodal grain structure known as a necklace-like structure [52, 223, 224]. With a further increase in

strain, the new fine grains gradually consume the larger grains and thereby produce an ultrafine microstructure [52]. Changing the grain refinement mechanisms involve producing changes in the microstructural morphologies and the strain hardening behavior during processing which and this produces a change in the texture evolution [175].

In addition, Figure 36 shows a net heterogeneity of microstructure, texture and microhardness across the axial direction in a pure Mg disc of high thickness (3 mm) processed at RT up to N = 3/4 turn [175] and this is similar to a thick Al disc processed by HPT (Figure 14) [175]. A typical B-fiber is formed in the central region due to the occurrence of dynamic recrystallization where the value of the shear strain is a maximum (Figure 36e). The advent of DRX explains the low value of the microhardness in the central position compared to the top and bottom of the disc (Figure 36f). The texture at the top of the disc arises from the presence of extensive twinning, especially extension twins which produce a rotation of about 90° from the initial texture [225]. The texture at the bottom of the disc is also different and in this position the disc appears to experience a larger shear strain since there is more grain refinement (Figure 36d). The variation in the texture between the top and bottom of the disc is strongly related to the deformation mechanism in HCP materials. Thus, at low strains the deformation is controlled by mechanical twining and then changes to slip deformation with increasing strain. It is important, therefore, to now investigate the heterogeneity in thick HPT discs after high shear strains.

2.3.4. Recrystallization texture of HPT-processed HCP materials

Until now, the evolution of the recrystallization texture after HPT processing of HCP materials is not widely reported [10, 11]. The texture of the HPT-processed Mg-

0.41Dy (wt.%) alloy after N = 5 turns forms a *B*-fiber with a second fiber, probably a C_2-fiber, located at $\varphi_1 = 180°$, $\Phi = 60°$ and $\varphi_2 = 0–90°$ where this is generally retained after annealing treatments at 473 ($0.5T_m$) and 673 K ($0.7T_m$) for 1 hour although the second fiber disappears in the sample annealed at 473 K. The stabilization of the texture during isochronal annealing is confirmed by the good thermal stability of the microstructure and the microhardness values [11]. However, the disappearance of the second fiber in the sample annealed at 473 K is not satisfactorily explained but it appears to be associated with the recrystallization at shear bands that lead to the formation of recrystallized grains with a variety of orientations [11, 226].

The evolution of texture of an Mg-1.43Nd (wt.%) alloy was investigated after HPT processing at N = 5 turns and isochronal annealing for 1 hour at 423 ($0.45T_m$), 523 ($0.56T_m$), 623 ($0.67T_m$) and 723 K ($0.78T_m$) using EBSD measurements [10]. The results show that the deformation texture is a *B*-fiber shifted by 60° towards SD and this is retained during annealing up to 523 K as shown in Figure 37 [10]. By increasing the annealing temperature to 623 and 723 K, the recrystallization texture changes to a *B*-fiber with symmetrical splitting towards SD as shown in Figure 37. Similar to the Mg-0.41Dy alloy already cited, the mean grain size of the Mg-1.43Nd alloy remains stable on annealing up to 523 K but there is major grain growth after annealing at 723 K. A change in the precipitation sequence during the annealing treatment and the pinning effect of the precipitates are responsible for the texture and microhardness variations [10]. By performing a comparison between the texture evolution in the Mg-0.41Dy and Mg-1.43Nd alloys, it is observed that the recrystallization texture of Mg-0.41Dy appears more stable than Mg-1.43Nd at a higher annealing temperature of 673 K. This difference is attributed to the occurrence of extensive DRX during HPT processing in the Mg-0.41Dy alloy and less DRX in the Mg-1.43Nd alloy [10, 68]. The absence of

DRX during conventional deformation processing such as rolling is also found responsible for the modification or weakening of the recrystallization texture in Mg-based alloys [227, 228]. The presence of $Mg_{12}Nd$ and $Mg_{24}Nd_5$ second phases in the Mg-1.43Nd alloy is the main cause for the restriction of DRX and hence this leads to a texture modification during a substitution treatment [10].

The formation of nanoscale $MgZn_2$ and Mg_2Zn_{11} intermetallics during annealing at 473 K for 1 hour is reported also as the main factor causing texture changes in the hybrid counterpart based on a series of Zn/Mg/Zn discs synthesized using HPT processing at P = 6.0 GPa for N = 30 turns [48].

3. Texture simulation during HPT processing for different materials

Over the last two or three decades, complex polycrystalline models for numerical prediction of the deformation processes and texture evolution have undergone a significant progression. Thus, models for texture prediction are now used as effective tools to connect the texture development to the deformation mechanisms and this assists in understanding the evolution of microstructure and mechanical properties. The models frequently used to predict the texture evolution during SPD, where the deformation is mainly by simple shear, are the full constraints (FC) Taylor model [229] and the visco-plastic self-consistent (VPSC) model [230, 231]. A complete description of these models, together with their formulation, is available in several reports [77, 229, 230, 232].

Briefly, it is assumed in the FC model that the local strain in the grains is equal to the imposed macroscopic strain [71, 233] but this is not suitable for large strain deformation modeling [234, 235]. By contrast, the VPSC model allows each grain to deform differently, depending specifically on its directional properties and the strength

of the interaction with its surroundings [71, 233]. Numerous reports demonstrated that the VPSC model has successfully delineated the experimental texture during SPD processing especially when processing by ECAP [233, 236-241]. An example of texture modeling is presented in Figure 38 and Table 11 by considering different approaches and hypotheses on the deformation history: thus, there is simple shear (SS) [242] or finite element (FE) [236] models and different grain refinement mechanisms; grain co-orientation (GCR) [243] and/or grain subdivision (GSD) [244].

The results demonstrate that the VPSC model with a grain co-rotation scheme and a simple shear deformation simulated by finite element (SCRD/FE) provides the best agreement with the experimental texture evolution during ECAP processing [233]. It is noted also that grain subdivision (GSD) is an important parameter in the models that tends to improve the agreements between the experimental and predicted textures during SPD processing [245-248] as is evident from inspection of Figure 39.

Nevertheless, it is important to recognize that the VPSC model with different applied combinations does not take into account the interaction of the grain with its neighbors as in grain-to-grain interactions and this leads inevitably to a predicted texture that is too strong [249]. A crystal plasticity finite element (CPFE) method was proposed as a possible solution for this VPSC limitation where the polycrystalline plasticity constitutive equations in the CPFE method are implemented into FE software [250, 251]. In this approach, the grains are characterized by finite elements and the deformation of the individual grains takes into account the macroscopic boundary conditions and also the grain-to-grain interactions [252]. The CPFE method provides a significant improvement for texture predictions in various deformation modes [249, 253-261] but nevertheless VPSC with grain co-rotation remains a good model which is

capable of generally predicting well the overall texture. The VPSC model is also very widely used due to its simplicity compared to the CPFE method [249].

Very recently, a 3D polycrystal simulation using a 3D cellular automaton model was developed [97, 98] and used successfully to confirm the effect of texture evolution on grain coarsening in FCC materials during SPD processing [96]. Figure 40 presents an example of the evolution of microstructure with different initial textures after shear deformation [98]. The results indicate that there is a texture-induced coarsening effect in SPD which should be introduced in grain refinement analyses.

Limited investigations are available dealing with the texture prediction during HPT processing for FCC [116, 126, 136, 262] and BCC [188] metals and there are no similar investigations for HCP materials. For single crystal FCC metals, the texture evolution for Ni and Al after HPT processing was predicted using a crystal plasticity finite element (CPFEM) model and the results are in good agreement with the experiments [126, 262]. The simulations confirm the instability of the shear texture components and their dependency on the amount of shear strain during HPT processing. It is worth noting also that, unlike polycrystalline samples, the texture simulation of single crystals is not complicated because it is not necessary to incorporate into the analysis the effects of grain boundaries and inherent grain-grain interactions.

For polycrystalline materials, the results for CP Al shown in Figure 41 indicate that at low shear strain the full constraint Taylor model gives a good agreement between the experimental and simulated texture compared to the VPSC model [116]. However, both models fail to produce the experimental texture at relatively large shear strains because the effect of grain fragmentation and the occurrence of DRX are not considered in the simulation procedures [116]. In addition, the Oblique Cube component (see section 2.2.2.1) is not predicted by the VPSC model for BCC NiAl processed by HPT at

a high temperature [188]. Despite these limitations, the VPSC model is helpful in elucidating and explaining the texture difference between the Fe-36Ni and Cu-2.5Ni-0.6Si alloys processed by HPT to low shear strains by simulating the effect of the initial texture [157].

In summary, the results show that the different proposed models of FC, VPSC and CPFEM can correctly predict the texture evolution after SPD processing in general and after HPT processing in particular. However, refinements should be introduced into the models to improve the simulations and especially that of the appearance of the Oblique Cube component at high temperatures. This suggests the need to incorporate restoration and DRX into the current models.

4. Texture comparison with some HPT processing variants

Several modified HPT processing methods were proposed over the last decade mostly due to the apparent limitations in HPT processing such as the inhomogeneity of the shear strain across the disc radius or the generally relatively small size of the HPT samples. The schemes of these HPT variant processing methods and their investigations of texture evolution are depicted schematically in Figure 42 a-c.

4.1. Texture evolution after HPDT vs. HPT

The high pressure double torsion (HPDT) method was first introduced in 2014 [263]. In HPDT processing both sides of the disk are rotated in opposite directions instead of only one side as in the standard HPT processing (see Figure 42a). The HPDT processing was first proposed as an alternative solution to decrease the inhomogeneity of the strain distributions as produced in the conventional HPT process [264]. However,

the results demonstrate that the gradient in grain structure as a function of radial direction is similar for both processing methods [264].

Theoretically, HPDT can introduce twice as much plastic strain per revolution compared with conventional HPT and this leads to finer grain sizes such as ~350 nm versus ~650 nm measured at the edge of a Cu disc processed through N = 4 turns [263]. The difference between the texture evolution after HPT and HPDT processing was investigated at the mid-radius and at the edge of the top and bottom surfaces of CP Cu discs processed for N = 1, 2 and 4 turns at RT. The results show that HPDT processing leads to the formation of typical shear components similar to HPT processing (see Figure 43). First, the texture of both processing methods sharpens with increasing strain and then weakens with additional grain refinement [263]. However, the texture is more homogenous across the HPDT disks than in HPT and this is explained because a saturation of the grain size is reached more rapidly in HPDT than in HPT processing [263].

The difference between the texture evolution after HPT and after HPDT processing was also investigated at the mid-radius and at the edge of metal-matrix composites of CP Cu and silicon carbide (SiC) processed under N = 2, 4, and 6 turns at RT [129]. In this report the texture of the metal-matrix composite is compared with that of the CP Cu alloy and a slight gradient in the shear texture is reported for the composite with increasing disc radius. More importantly, the texture of the composite is very much weakened by comparison with the bulk Cu alloy regardless of the numbers of turns. The weakening of the texture even after a low strain is attributed to the presence of the SiC particles. Thus, if the SiC particles in the metal matrix are sufficiently hard they will act as obstacles for the movement of dislocations and thereby reduce the activation of slip systems and this will slow the texture formation [129, 265].

By contrast, each particle forms its own deformation zone and lattice rotations within these zones increase with increasing strain leading to a weak or even a near-random texture [129, 266].

4.2.Texture evolution after RHPT vs. HPT

The reversal high pressure torsion (RHPT) procedure was first proposed in 2005 [169] where samples are either strained in one direction as in conventional monotonic processing (m-HPT) or the straining direction is reversed periodically as in cyclic processing (c-HPT). Later, the technique of reversing the straining direction during HPT processing was used by several investigators [38, 118, 267-281] in order to highlight the effect of loading path on grain refinement and texture evolution in HPT.

In one set of experiments [38, 118] a cycle of RHPT processing consisted of deforming a CP Al sample to 12° rotation, equivalent to N ≈ 1/16 turn, in a clockwise direction followed by counterclockwise rotation up to the same rotation (12°) to produce a total of 24° of rotation which is then equivalent to N = 1/8 turn during conventional or monotonic HPT processing. In addition, the Al sample was processed to four reversal cycles that were equivalent to 96° of their monotonic counterpart so that N ≈ 1 HPT turn. The texture was measured in the central region and the edge of the processed discs. The results are shown in Figure 44 and they demonstrate that m-HPT leads to the formation of a typical shear texture for a high γ_{SFE} material through an equivalent strain range of 1–4 consisting of a partial *A*-fiber and a full *B*-fiber with the dominance of the *C* component, and then a weakening up to $\varepsilon_{eq} = 8$.

By contrast, the formation of the texture after RHPT processing was significantly different where only some components belonging to the *A*-fiber, such as the $A/\bar{A}$, A_1^* and A_2^* components, appear and disappear periodically with increasing

equivalent strain. The texture difference between m-HPT and c-HPT, and the instability of the RHPT texture, was a consequence of the nature of the reversal deformation path. Thus, the free isolated dislocations contained within the cells or sub-grains are able to accumulate and annihilate during the reversed motion which retards the generation of the HAGBs. Moreover, even the sub-boundaries and cell walls are not sufficiently stable against the reversal strain which directly affects the lattice rotation and thus the texture formation. Unusually, a Cube component, and therefore a recrystallization texture component, was detected at the edge of both RHPT samples after 1 and 4 RHPT cycles [38, 118]. The presence of a Cube texture is not expected since the microstructural evolution demonstrates that the edge of the RHPT samples continue to contain dislocations within the subgrains and in the vicinity of the subgrain boundaries [282].

It is noted that the texture evolution revealed by this latter investigation corresponds only to {111} pole figures which in practice are not sufficient for an accurate identification of the texture components. Moreover, the achieved accumulated strain used in this investigation is relatively weak at $\varepsilon_{eq} = 8$ compared to the much higher strains usually reported where, typically, $\varepsilon_{eq} \approx 100$. In addition, it must be noted that the resulting grain refinement and grain boundary distributions are very sensitive to the applied strain amplitude (strain increment) in RHPT processing [110, 267]. It is expected, therefore, that the texture evolution may be significantly affected by the applied strain amplitude but to date there have been no investigations to evaluate this possibility.

4.3.Texture evolution after HPTT vs. HPT

Processing by High Pressure Tube Twisting (HPTT) was first proposed in 2009 [283] as an efficient new SPD processing method and later it was further developed [35, 36, 284]. HPTT is a variant of HPT processing wherein instead of a disk there is a thin-walled tube which is exposed to very large shear strain levels in a single operation, as shown schematically in Figure 42c. As in conventional HPT processing, the shear strain is not constant within the tube walls. In practice, however, the shear gradient in HPTT processing is the opposite to the gradient produced during HPT processing. Thus, the inner wall of the tube sample undergoes a maximum strain level and this strain decreases monotonically towards the external wall [283] whereas in HPT processing the shear strain increases with increasing radius. The average shear strain can be calculated from the equation [34]:

$$\bar{\gamma} = \frac{\theta}{ln\,(a/b)} \tag{2}$$

where θ is the rotation angle and a and b are the internal and external radii of the tube sample, respectively.

Experiments show that HPTT processing can introduce larger strains than in conventional HPT processing. For example, the equivalent strain for N = 1 HPTT turn and for a geometry of b/a = 10/9 is about ε_{eq} = 34.43 whereas the equivalent strain is ε_{eq} = 20.14 at the edge of a disc sample with a radius of 10 mm after the same number of HPT turns.

Among the various methods of modified HPT processing, the microstructures and mechanical properties of various metals were investigated after HPTT processing, such as Al, Cu, Fe, brass and Mg-based alloys, and the results are documented comprehensively in a recent review [285].

The evolution of the texture after HPTT processing was investigated in detail for CP Al and AA5086 alloys [34, 285]. The results show that the texture after HPTT is very similar to that reported for Al alloys processed by HPT processing where the texture is a typical shear texture of *A*-fiber and *B*-fiber with the dominance of the *C* component and it exhibits a gradient distributions within the cross-section of the tube sample as shown in Figure 45. The results also reveal a similar texture evolution as a function of increasing strain where the texture weakens and the *C* component continues to dominate [34, 285].

4.4.Texture evolution after HPCS vs. HPT

High pressure compressive shearing (HPCS) was introduced in 2019 [39] and it is essentially a modified version of high pressure shearing (HPS) as first proposed in 2009 [37]. Processing by HPS entails applying a large shear strain by displacing sheet or rod samples by pushing a plunger from one side to the other under high pressure (see Figure 42d) [37]. Numerous investigations were performed to explore the effect of this process on grain refinement and superplasticity in various materials (Al, Ni, Mg and Ti) [37, 286-292] but there are no comprehensive reports on the texture evolution.

As shown schematically in Figure 42e, HPCS processing is basically similar to HPS but with the addition of a confining pressure and further compressive straining to increase the shear strain [39]. At the present time, the evolution of texture after HPCS was investigated only in the BCC material of ARMCO steel [39]. Figure 46 shows that all BCC ideal shear components are formed after 1 pass and they persist after 3 passes with some changes in their intensities. It is claimed that the texture intensity is low and this indicates a small anisotropy. However, it is known that the shear texture is usually weak compared to other texture types. It is interesting to note that the grain size,

crystallographic disorientation and texture appear to be uniformly distributed throughout the thicknesses of the samples [39].

4.5.Combinations of HPT processing with other SPD processing techniques

A combination of different types of deformation processing is often used in order to optimize the microstructure and the mechanical properties of materials [122].

Generally, the texture is very similar, composed of a weak *A*-fiber, a strong *B*-fiber with the dominance of the *C* component, in pure Ni subjected to HPT processing at N = 5 turns and for a sample firstly processed by ECAP through 8 passes using processing route *Bc* and subsequently processed again by HPT at N = 5 turns [122]. The similarity in the texture is ascribed to the same shear deformation imposed in ECAP and HPT processing. By contrast, HPT processing of the Cu-layers of nanolayered Cu-Nb composites fabricated by ARB processing exhibit a very different texture evolution [131] by comparison with that reported for pure Cu [127, 128]. First, the texture is random at equivalent strains ε_{eq} ranging between 2.42 and 6.23, then a complete *A*-fiber forms when ε_{eq} is increased to 10.8 and 165.1. Finally, the A_1^* component dominates the texture at a very high shear strain of ε_{eq} = 1437–2592. It is interesting to note that the presence of a sharp A-fiber is also reported in an HPT-processed Cu-2.5Ni-0.6Si alloy [72]. The texture evolution of an Nb layer which is a BCC metal is found also to be different and more complex than the textures usually reported in BCC materials [131].

5. Summary and conclusions

The evolution of the deformation textures of FCC, BCC, and HCP materials after HPT processing and the resultant recrystallization texture during different heat

treatments are reviewed in this report based on the published data available to date. The main findings may be summarized as follows:

- For FCC materials, HPT processing leads to the formation of two texture fibers: an *A*-fiber containing *A*, $\bar{A}$, A_1^* and A_2^* components and a *B*-fiber with *A*, $\bar{A}$, *B*, $\bar{B}$ and *C* components. The sharpness of the individual texture components depends strongly on the value of the stacking fault energy of the material. For example, the *C* component dominates the deformation texture of materials with high γ_{SFE} while the *B*/$\bar{B}$ components are dominant in medium and low γ_{SFE} materials. Furthermore, the initial grain size and the presence of second phase particles play a major role in the development of the deformation texture. For the majority of FCC materials, it appears that the texture is unstable and heterogeneous across the disc radius during the earlier stages of deformation but becomes more homogenous with increasing shear strain. However, the texture is much weaker than in other SPD processes due to the extreme grain refinement and the activation of grain boundary sliding. The recrystallization texture after HPT processing is not yet well explored in FCC materials but it should be emphasized that the deformation shear texture is retained during the recrystallization and grain growth processes.
- For BCC materials, HPT processing leads to the formation of *F*, *J*, $\bar{J}$, *E*, $\bar{E}$, D_1 and D_2 components. However, most of the results for BCC metals were obtained after processing by HPT at a high deformation temperature where dynamic recrystallization occurs and this leads also to the formation of the Oblique Cube. The deformation texture is retained after an annealing treatment in W pure metal but changes in an annealed Fe-9Cr alloy depending on the static recrystallization mechanism. However, more research is now needed to fully correlate the grain refinement mechanism, mechanical properties and texture evolution and also to obtain a more complete

understanding of the mechanisms responsible for the formation of the recrystallization texture.

- For HCP materials, five fibers of *B, P, Y,* C_1 and C_2 are expected to form during HPT processing. Nevertheless, the published data demonstrate that the *B*-fiber, known also as a basal texture, is developed in the majority of HCP-processed materials whatever the initial condition of the material and their respective *c/a* ratios. Furthermore, the distribution of the basal pole and the deviation of the basal texture from its ideal position in Mg-based alloys depend strongly on the alloying elements and the presence of second phases. In practice, the presence of second phases also control the texture modification observed during an annealing treatment by the restriction of DRX during HPT processing.
- The texture development during the alternative procedures of processing by HPDT, RHPT, HPTT and HPSC are reported to be generally similar to those formed during conventional HPT processing mostly due to the presence of the same shear deformation.

Overall, this review confirms that HPT processing induces considerable changes in the texture and microstructure for different material systems. Crucial information about the mechanisms of plastic flow and strain-induced changes in the mechanical properties are directly linked and arise from these results. Therefore, a serious challenge is now to conduct thorough research investigations on the topics of dislocation microstructures, sub-grain sizes after fragmentation, second phase particle distributions and sizes and the consequent effect of alloying elements. It is important to note that the effects on the texture evolution of most of these metallurgical parameters has not yet been satisfactorily quantified.

It is also of primary importance to develop model calculations of texture which, when judiciously combined with comprehensive experimental analyses, can provide valuable and decisive information concerning the deformation mechanisms and the correlations between the texture, flow stress and anisotropy. To date, there are only limited reports dealing with texture simulation. This means that special subroutines and procedures must be dedicated to HPT processing and then implemented in model calculations and in simulations such as the Self-Consistent or Finite Element codes.

As a final comment, it would be beneficial to more deeply explore the evolution of the recrystallization textures and thermal stability after HPT processing in FCC, BCC and HCP materials in order to obtain a more complete understanding of their occurrence and mechanisms.

Acknowledgements

The work of one of us was supported by the European Research Council under Grant Agreement No. 267464-SPDMETALS (TGL).

References

[1] Straumal BB, Mazilkin AA, Baretzky B, Schütz G, Rabkin E, Valiev RZ. Accelerated Diffusion and Phase Transformations in Co–Cu Alloys Driven by the Severe Plastic Deformation. Materials Transactions. 2012;53:63-71.

[2] Valiev RZ, Zhilyaev AP, Langdon TG. Bulk nanostructured materials: Fundamentals and applications. TMS/Wiley, Hoboken, NJ, USA2013.

[3] Azzeddine H, Mehdi B, Hennet L, Thiaudière D, Alili B, Kawasaki M, et al. An in situ synchrotron X-ray diffraction study of precipitation kinetics in a severely deformed Cu–Ni–Si alloy. Materials Science and Engineering: A. 2014;597:288-94.

[4] Sauvage X, Enikeev N, Valiev R, Nasedkina Y, Murashkin M. Atomic-scale analysis of the segregation and precipitation mechanisms in a severely deformed Al–Mg alloy. Acta Materialia. 2014;72:125-36.

[5] Azzeddine H, Harfouche M, Hennet L, Thiaudiere D, Kawasaki M, Bradai D, et al. An X-ray absorption spectroscopy investigation of the local atomic structure in Cu–Ni–Si alloy after severe plastic deformation and ageing. Philosophical Magazine. 2015;95:2482-90.

[6] Straumal BB, Kilmametov AR, Ivanisenko Y, Mazilkin AA, Kogtenkova OA, Kurmanaeva L, et al. Phase transitions induced by severe plastic deformation: steady-state and equifinality. International Journal of Materials Research. 2015;106:657-64.

[7] Bourezg YI, Azzeddine H, Hennet L, Thiaudière D, Huang Y, Bradai D, et al. The sequence and kinetics of pre-precipitation in Mg-Nd alloys after HPT processing: A synchrotron and DSC study. Journal of Alloys and Compounds. 2017;719:236-41.

[8] Nasedkina Y, Sauvage X, Bobruk EV, Murashkin MY, Valiev RZ, Enikeev NA. Mechanisms of precipitation induced by large strains in the Al-Cu system. Journal of Alloys and Compounds. 2017;710:736-47.

[9] Straumal BB, Pontikis V, Kilmametov AR, Mazilkin AA, Dobatkin SV, Baretzky B. Competition between precipitation and dissolution in Cu–Ag alloys under high pressure torsion. Acta Materialia. 2017;122:60-71.

[10] Tighiouaret S, Lachhab R, Hanna A, Azzeddine H, Huang Y, Baudin T, et al. Thermal Stability of an Mg–Nd Alloy Processed by High-Pressure Torsion. Advanced Engineering Materials. 2019;21:1900801.

[11] Hanna A, Azzeddine H, Huang Y, Bradai D, Cabrera JM, Langdon TG. An investigation of the thermal stability of an MgDy alloy after processing by high-pressure torsion. Materials Characterization. 2019;151:519-29.

[12] Edalati P, Mohammadi A, Tang Y, Floriano R, Fuji M, Edalati K. Phase transformation and microstructure evolution in ultrahard carbon-doped AlTiFeCoNi high-entropy alloy by high-pressure torsion. Materials Letters. 2021;302:130368.

[13] Valiev RZ, Langdon TG. Principles of equal-channel angular pressing as a processing tool for grain refinement. Progress in Materials Science. 2006;51:881-981.

[14] Saito Y, Tsuji N, Utsunomiya H, Sakai T, Hong RG. Ultra-fine grained bulk aluminum produced by accumulative roll-bonding (ARB) process. Scripta Materialia. 1998;39:1221-7.

[15] Zhilyaev AP, Langdon TG. Using high-pressure torsion for metal processing: Fundamentals and applications. Progress in Materials Science. 2008;53:893-979.

[16] Iwahashi Y, Wang J, Horita Z, Nemoto M, Langdon TG. Principle of equal-channel angular pressing for the processing of ultra-fine grained materials. Scripta Materialia. 1996;35:143-6.

[17] Tsuji N, Saito Y, Lee S-H, Minamino Y. ARB (Accumulative Roll-Bonding) and other new Techniques to Produce Bulk Ultrafine Grained Materials. Advanced Engineering Materials. 2003;5:338-44.

[18] Valiev RZ, Ivanisenko YV, Rauch EF, Baudelet B. Structure and deformaton behaviour of Armco iron subjected to severe plastic deformation. Acta Materialia. 1996;44:4705-12.

[19] Furukawa M, Iwahashi Y, Horita Z, Nemoto M, Langdon TG. The shearing characteristics associated with equal-channel angular pressing. Materials Science and Engineering: A. 1998;257:328-32.

[20] Valiev RZ, Islamgaliev RK, Alexandrov IV. Bulk nanostructured materials from severe plastic deformation. Progress in Materials Science. 2000;45:103-89.

[21] Langdon TG. Twenty-five years of ultrafine-grained materials: Achieving exceptional properties through grain refinement. Acta Materialia. 2013;61:7035-59.

[22] Kaneko S, Fukuda K, Utsunomiya H, Sakai T, Saito Y, Furushiro N. Ultra Grain Refinement of Aluminium 1100 by ARB with Cross Rolling. Materials Science Forum. 2003;426-432:2649-54.

[23] Alizadeh M. Processing of Al/B4C composites by cross-roll accumulative roll bonding. Materials Letters. 2010;64:2641-3.

[24] Verstraete K, Helbert AL, Brisset F, Baudin T. Comparison between ARB and CARB processes on an AA5754/AA6061 composite. IOP Conference Series: Materials Science and Engineering. 2014;63:012090.

[25] Verstraete K, Helbert AL, Brisset F, Benoit A, Paillard P, Baudin T. Microstructure, mechanical properties and texture of an AA6061/AA5754 composite fabricated by cross accumulative roll bonding. Materials Science and Engineering: A. 2015;640:235-42.

[26] Tirsatine K, Azzeddine H, Baudin T, Helbert AL, Brisset F, Bradai D. Microstructure and Microtexture Evolution of Invar Alloy after Cross Accumulative Roll Bonding (CARB) Compared to ARB. Materials Science Forum. 2017;879:744-9.

[27] Habila W, Azzeddine H, Mehdi B, Tirsatine K, Baudin T, Helbert A-L, et al. Investigation of microstructure and texture evolution of a Mg/Al laminated composite elaborated by accumulative roll bonding. Materials Characterization. 2019;147:242-52.

[28] Ding C, Xu J, Li X, Shan D, Guo B, Langdon TG. Microstructural Evolution and Mechanical Behavior of Cu/Nb Multilayer Composites Processed by Accumulative Roll Bonding. Advanced Engineering Materials. 2020;22:1900702.

[29] Zhang R, Acoff VL. Processing sheet materials by accumulative roll bonding and reaction annealing from Ti/Al/Nb elemental foils. Materials Science and Engineering: A. 2007;463:67-73.

[30] Rahmatabadi D, Tayyebi M, Hashemi R, Faraji G. Microstructure and mechanical properties of Al/Cu/Mg laminated composite sheets produced by the ARB proces. International Journal of Minerals, Metallurgy, and Materials. 2018;25:564-72.

[31] Bridgman PW. Effects of High Shearing Stress Combined with High Hydrostatic Pressure. Physical Review. 1935;48:825-47.

[32] Hohenwarter A, Bachmaier A, Gludovatz B, Scheriau S, Pippan R. Technical parameters affecting grain refinement by high pressure torsion. International Journal of Materials Research. 2009;100:1653-61.

[33] Edalati K, Horita Z. A review on high-pressure torsion (HPT) from 1935 to 1988. Materials Science and Engineering: A. 2016;652:325-52.

[34] Arzaghi M, Fundenberger JJ, Toth LS, Arruffat R, Faure L, Beausir B, et al. Microstructure, texture and mechanical properties of aluminum processed by high-pressure tube twisting. Acta Materialia. 2012;60:4393-408.

[35] Wang JT, Li Z, Wang J, Langdon TG. Principles of severe plastic deformation using tube high-pressure shearing. Scripta Materialia. 2012;67:810-3.

[36] Li Z, Zhang PF, Yuan H, Lin K, Liu Y, Yin DL, et al. Principle of one-step synthesis for multilayered structures using tube high-pressure shearing. Materials Science and Engineering: A. 2016;658:367-75.

[37] Fujioka T, Horita Z. Development of High-Pressure Sliding Process for Microstructural Refinement of Rectangular Metallic Sheets. Materials Transactions. 2009;50:930-3.

[38] Orlov D, Bhattacharjee PP, Todaka Y, Umemoto M, Tsuji N. Reversal Straining to Manage Structure in Pure Aluminum under SPD. Materials Science Forum. 2008;584-586:133-8.

[39] Toth LS, Vu VQ, Dhinwal SS, Zhao Y, Massion R, Chen C, et al. The mechanics of High Pressure Compressive Shearing with application to ARMCO® steel. Materials Characterization. 2019;154:127-37.

[40] Pippan R, Scheriau S, Hohenwarter A, Hafok M. Advantages and Limitations of HPT: A Review. Materials Science Forum. 2008;584-586:16-21.

[41] Jenei P, Gubicza J, Yoon EY, Kim HS. X-ray diffraction study on the microstructure of a Mg–Zn–Y alloy consolidated by high-pressure torsion. Journal of Alloys and Compounds. 2012;539:32-5.

[42] Wen H, Islamgaliev RK, Nesterov KM, Valiev RZ, Lavernia EJ. Dynamic balance between grain refinement and grain growth during high-pressure torsion of Cu powders. Philosophical Magazine Letters. 2013;93:481-9.

[43] Borchers C, Garve C, Tiegel M, Deutges M, Herz A, Edalati K, et al. Nanocrystalline steel obtained by mechanical alloying of iron and graphite subsequently compacted by high-pressure torsion. Acta Materialia. 2015;97:207-15.

[44] Kawaski M, Langdon TG. Fabrication of high strength hybrid materials through the application of high-pressure torsion. Acta Physica Polonica A. 2018;134:615-22.

[45] Han J-K, Liss K-D, Langdon TG, Kawasaki M. Synthesis of a bulk nanostructured metastable Al alloy with extreme supersaturation of Mg. Scientific Reports. 2019;9:17186.

[46] Han J-K, Liss K-D, Langdon TG, Jang J-i, Kawasaki M. Mechanical properties and structural stability of a bulk nanostructured metastable aluminum-magnesium system. Materials Science and Engineering: A. 2020;796:140050.

[47] Kawasaki M, Jung SH, Park J-M, Lee J, Jang J-i, Han J-K. Mechanical Bonding of Aluminum Hybrid Alloy Systems through High-Pressure Torsion. Advanced Engineering Materials. 2020;22:1900483.

[48] Hernández-Escobar D, Unocic RR, Kawasaki M, Boehlert CJ. High-pressure torsion processing of Zn–3Mg alloy and its hybrid counterpart: A comparative study. Journal of Alloys and Compounds. 2020;831:154891.

[49] Tirsatine K, Azzeddine H, Baudin T, Helbert A-L, Brisset F, Alili B, et al. Texture and microstructure evolution of Fe–Ni alloy after accumulative roll bonding. Journal of Alloys and Compounds. 2014;610:352-60.

[50] Zhilyaev AP, Kim BK, Nurislamova GV, Baró MD, Szpunar JA, Langdon TG. Orientation imaging microscopy of ultrafine-grained nickel. Scripta Materialia. 2002;46:575-80.

[51] Zhilyaev AP, Nurislamova GV, Kim BK, Baró MD, Szpunar JA, Langdon TG. Experimental parameters influencing grain refinement and microstructural evolution during high-pressure torsion. Acta Materialia. 2003;51:753-65.

[52] Figueiredo RB, Langdon TG. Grain refinement and mechanical behavior of a magnesium alloy processed by ECAP. Journal of Materials Science. 2010;45:4827-36.

[53] Serre P, Figueiredo RB, Gao N, Langdon TG. Influence of strain rate on the characteristics of a magnesium alloy processed by high-pressure torsion. Materials Science and Engineering: A. 2011;528:3601-8.

[54] Tirsatine K, Azzeddine H, Huang Y, Baudin T, Helbert A-L, Brisset F, et al. An EBSD analysis of Fe-36%Ni alloy processed by HPT at ambient and a warm temperature. Journal of Alloys and Compounds. 2018;753:46-53.

[55] Wongsa-Ngam J, Kawasaki M, Langdon TG. A comparison of microstructures and mechanical properties in a Cu–Zr alloy processed using different SPD techniques. Journal of Materials Science. 2013;48:4653-60.

[56] Azzeddine H, Baudin T, Helbert AL, Brisset F, Larbi FH, Tirsatine K, et al. Grain boundary character distribution of CuNiSi and FeNi alloys processed by severe plastic deformation. IOP Conference Series: Materials Science and Engineering. 2015;82:012076.

[57] Lowe TC, Valiev RZ, Li X, Ewing BR. Commercialization of bulk nanostructured metals and alloys. MRS Bulletin. 2021;46:265-72.

[58] Huang Y, Figueiredo RB, Baudin T, Brisset F, Langdon TG. Evolution of Strength and Homogeneity in a Magnesium AZ31 Alloy Processed by High-Pressure Torsion at Different Temperatures. Advanced Engineering Materials. 2012;14:1018-26.

[59] Figueiredo RB, Aguilar MTP, Cetlin PR, Langdon TG. Processing magnesium alloys by severe plastic deformation. IOP Conference Series: Materials Science and Engineering. 2014;63:012171.

[60] Edalati K, Horita Z. Application of high-pressure torsion for consolidation of ceramic powders. Scripta Materialia. 2010;63:174-7.

[61] Jenei P, Yoon EY, Gubicza J, Kim HS, Lábár JL, Ungár T. Microstructure and hardness of copper–carbon nanotube composites consolidated by High Pressure Torsion. Materials Science and Engineering: A. 2011;528:4690-5.

[62] Cubero-Sesin JM, Horita Z. Powder consolidation of Al–10wt% Fe alloy by High-Pressure Torsion. Materials Science and Engineering: A. 2012;558:462-71.

[63] Li P, Wang X, Xue K-M, Tian Y, Wu Y-C. Microstructure and recrystallization behavior of pure W powder processed by high-pressure torsion. International Journal of Refractory Metals and Hard Materials. 2016;54:439-44.

[64] Zhilyaev AP, Ringot G, Huang Y, Cabrera JM, Langdon TG. Mechanical behavior and microstructure properties of titanium powder consolidated by high-pressure torsion. Materials Science and Engineering: A. 2017;688:498-504.

[65] Castro MM, Pereira PHR, Isaac A, Figueiredo RB, Langdon TG. Development of a magnesium-alumina composite through cold consolidation of machining chips by high-pressure torsion. Journal of Alloys and Compounds. 2019;780:422-7.

[66] Castro MM, Pereira PHR, Isaac A, Langdon TG, Figueiredo RB. Inverse Hall–Petch Behaviour in an AZ91 Alloy and in an AZ91–Al2O3 Composite Consolidated by High-Pressure Torsion. Advanced Engineering Materials. 2020;22:1900894.

[67] Qiao XG, Zhao YW, Gan WM, Chen Y, Zheng MY, Wu K, et al. Hardening mechanism of commercially pure Mg processed by high pressure torsion at room temperature. Materials Science and Engineering: A. 2014;619:95-106.

[68] Hanna A, Azzeddine H, Lachhab R, Baudin T, Helbert A-L, Brisset F, et al. Evaluating the textural and mechanical properties of an Mg-Dy alloy processed by high-pressure torsion. Journal of Alloys and Compounds. 2019;778:61-71.

[69] Randle V, Engler O. Introduction to texture analysis: macrotexture, microtexture, and orientation mapping: Amsterdam : Gordon & Breach; 2000.

[70] Suwas S, Mondal S. Texture Evolution in Severe Plastic Deformation Processes. Materials Transactions. 2019;60:1457-71.

[71] Beyerlein IJ, Tóth LS. Texture evolution in equal-channel angular extrusion. Progress in Materials Science. 2009;54:427-510.

[72] Khereddine AY, Hadj Larbi F, Azzeddine H, Baudin T, Brisset F, Helbert A-L, et al. Microstructures and textures of a Cu–Ni–Si alloy processed by high-pressure torsion. Journal of Alloys and Compounds. 2013;574:361-7.

[73] Azzeddine H, Tirsatine K, Baudin T, Helbert A-L, Brisset F, Bradai D. Texture evolution of an Fe–Ni alloy sheet produced by cross accumulative roll bonding. Materials Characterization. 2014;97:140-9.

[74] Tomé C, Agnew SR, Bourke MAM, Blumenthal WR, Brown DW, Kaschner GC, et al. The Relation between Texture, Twinning and Mechanical Properties in Hexagonal Aggregates. Materials Science Forum. 2002;408-412:263-8.

[75] Brown DW, Agnew SR, Abeln SP, Blumenthal WR, Bourke MAM, Mataya MC, et al. The Role of Texture, Temperature and Strain Rate in the Activity of Deformation Twinning. Materials Science Forum. 2005;495-497:1037-42.

[76] Kocks UF, Stout MG, Rollett AD. The Influence of Texture on Strain Hardening††Work supported by the U.S. Department of Energy, Basic Energy Sciences. In: Kettunen PO, Lepistö TK, Lehtonen ME, editors. Strength of Metals and Alloys (ICSMA 8). Oxford: Pergamon; 1989. p. 25-34.

[77] Kocks F, Tomé C, Wenk HR. Texture and Anisotropy: Preferred Orientations in Polycrystals and Their Effect on Material Properties: Cambridge University Press; 1998.

[78] Friedman PA, Liao KC, Pan J, Barlat F. Texture development and hardening characteristics of steel sheets under plane-strain compression. Journal of Materials Engineering and Performance. 1999;8:225-35.

[79] Lopes AB, Barlat F, Gracio JJ, Ferreira Duarte JF, Rauch EF. Effect of texture and microstructure on strain hardening anisotropy for aluminum deformed in uniaxial tension and simple shear. International Journal of Plasticity. 2003;19:1-22.

[80] Sarker D, Chen DL. The Orientation Dependence of Strain Hardening and Texture Development in an Extruded Magnesium Alloy. Materials Science Forum. 2014;783-786:363-8.

[81] Salevati MA, Akbaripanah F, Mahmudi R, Fekete KH, Heczel A, Gubicza J. Comparison of the effects of isothermal equal channel angular pressing and multi-directional forging on mechanical properties of AM60 magnesium alloy. Materials Science and Engineering: A. 2020;776:139002.

[82] Azzeddine H, Abdessameud S, Alili B, Boumerzoug Z, Bradai D. Effect of grain boundary misorientation on discontinuous precipitation in an AZ91 alloy. Bulletin of Materials Science. 2011;34:1471-6.

[83] Nagy E, Mertinger V, Tranta F, Sólyom J. Deforming Texture Effect on Phase Transformation in Stainless Steels. Materials Science Forum. 2002;414-415:281-8.

[84] Li X, Yang P, Meng L. Orientational Analysis on Static Recrystallization at Tension Twins in AZ31 Magnesium Alloy. Advanced Materials Research. 2011;299-300:778-84.

[85] Zhao ZB, Wang QJ, Hu QM, Liu JR, Yu BB, Yang R. Effect of β (110) texture intensity on α-variant selection and microstructure morphology during β→α phase transformation in near α titanium alloy. Acta Materialia. 2017;126:372-82.

[86] Qin DH, Wang MJ, Sun CY, Su ZX, Qian LY, Sun ZH. Interaction between texture evolution and dynamic recrystallization of extruded AZ80 magnesium alloy during hot deformation. Materials Science and Engineering: A. 2020;788:139537.

[87] Lee K-M, Huh M-Y, Park S, Engler O. Effect of Texture Components on the Lankford Parameters in Ferritic Stainless Steel Sheets. ISIJ International. 2012;52:522-9.

[88] Tamimi S, Sivaswamy G, Violatos I, Moturu S, Rahimi S, Blackwell P. Modelling and experimentation of the evolution of texture in an Al-Mg alloy during earing cupping test. Procedia Engineering. 2017;207:1-6.

[89] Kodukula S, Manninen T, Porter D. Estimation of Lankford Coefficients of Austenitic and Ferritic Stainless Steels using Mean Grain Orientations from Micro-texture Measurements. ISIJ International. 2021;61:401-7.

[90] Williams HJ. Magnetic Properties of Single Crystals of Silicon Iron. Physical Review. 1937;52:747-51.

[91] Subramanya Sarma V, Eickemeyer J, Schultz L, Holzapfel B. Recrystallisation texture and magnetisation behaviour of some FCC Ni–W alloys. Scripta Materialia. 2004;50:953-7.

[92] Bhattacharjee PP, Ray RK, Upadhyaya A. Nickel base substrate tapes for coated superconductor applications. Journal of Materials Science. 2007;42:1984-2001.

[93] Xin R, Li B, Li L, Liu Q. Influence of texture on corrosion rate of AZ31 Mg alloy in 3.5wt.% NaCl. Materials & Design. 2011;32:4548-52.

[94] Chen XP, Sun HF, Chen D, Wang LX, Liu Q. On recrystallization texture and magnetic property of Cu-Ni alloys. Materials Characterization. 2016;121:149-56.

[95] Sabbaghian M, Mahmudi R, Shin KS. Effect of texture and twinning on mechanical properties and corrosion behavior of an extruded biodegradable Mg–4Zn alloy. Journal of Magnesium and Alloys. 2019;7:707-16.

[96] Gu CF, Toth LS, Rusz S, Bova M. Texture induced grain coarsening in severe plastic deformed low carbon steel. Scripta Materialia. 2014;86:36-9.

[97] Zhang C, Toth LS. Polycrystal Simulation of Texture-Induced Grain Coarsening during Severe Plastic Deformation. Materials. 2020;13:5834.

[98] Zhang C, Toth LS. 3D simulation of texture evolution induced grain coarsening in FCC polycrystals during severe plastic deformation. IOP Conference Series: Materials Science and Engineering. 2021;1121:012045.

[99] Song R, Ponge D, Raabe D, Speer JG, Matlock DK. Overview of processing, microstructure and mechanical properties of ultrafine grained bcc steels. Materials Science and Engineering: A. 2006;441:1-17.

[100] Meyers MA, Mishra A, Benson DJ. Mechanical properties of nanocrystalline materials. Progress in Materials Science. 2006;51:427-556.

[101] Figueiredo RB, Langdon TG. Fabricating Ultrafine-Grained Materials through the Application of Severe Plastic Deformation: a Review of Developments in Brazil. Journal of Materials Research and Technology. 2012;1:55-62.

[102] Zhu YT, Liao XZ, Wu XL. Deformation twinning in nanocrystalline materials. Progress in Materials Science. 2012;57:1-62.

[103] Estrin Y, Vinogradov A. Extreme grain refinement by severe plastic deformation: A wealth of challenging science. Acta Materialia. 2013;61:782-817.

[104] Sabirov I, Murashkin MY, Valiev RZ. Nanostructured aluminium alloys produced by severe plastic deformation: New horizons in development. Materials Science and Engineering: A. 2013;560:1-24.

[105] Huang Y, Langdon TG. Advances in ultrafine-grained materials. Materials Today. 2013;16:85-93.

[106] Sakai T, Belyakov A, Kaibyshev R, Miura H, Jonas JJ. Dynamic and post-dynamic recrystallization under hot, cold and severe plastic deformation conditions. Progress in Materials Science. 2014;60:130-207.

[107] Alaneme KK, Okotete EA. Enhancing plastic deformability of Mg and its alloys—A review of traditional and nascent developments. Journal of Magnesium and Alloys. 2017;5:460-75.

[108] Cao Y, Ni S, Liao X, Song M, Zhu Y. Structural evolutions of metallic materials processed by severe plastic deformation. Materials Science and Engineering: R: Reports. 2018;133:1-59.

[109] Ovid'ko IA, Valiev RZ, Zhu YT. Review on superior strength and enhanced ductility of metallic nanomaterials. Progress in Materials Science. 2018;94:462-540.

[110] Pippan R, Scheriau S, Taylor A, Hafok M, Hohenwarter A, Bachmaier A. Saturation of Fragmentation During Severe Plastic Deformation. Annual Review of Materials Research. 2010;40:319-43.

[111] Azzeddine H, Tirsatine K, Baudin T, Helbert A-L, Mathond MH, Brisset F, et al. Neutron diffraction versus EBSD analysis of the texture in Fe-36%Ni alloy after accumulative roll bonding. Indian Journal of Engineering and Materials Sciences. 2017;24:35-44.

[112] Bunge HJ. 2 - Orientation of Individual Crystallites. In: Bunge HJ, editor. Texture Analysis in Materials Science: Butterworth-Heinemann; 1982. p. 3-41.

[113] Canova GR, Kocks UF, Jonas JJ. Theory of torsion texture development. Acta Metallurgica. 1984;32:211-26.

[114] Montheillet F, Cohen M, Jonas JJ. Axial stresses and texture development during the torsion testing of Al, Cu and α-Fe. Acta Metallurgica. 1984;32:2077-89.

[115] Montheillet F, Gilormini P, Jonas JJ. Relation between axial stresses and texture development during torsion testing: A simplified theory. Acta Metallurgica. 1985;33:705-17.

[116] Naghdy S, Kestens L, Hertelé S, Verleysen P. Evolution of microstructure and texture in commercial pure aluminum subjected to high pressure torsion processing. Materials Characterization. 2016;120:285-94.

[117] Liu Y, Lu C, Wang H, Tieu AK, Liu B. Microstructure evolution, lattice rotation retardation and grain orientation fragmentation in commercial purity aluminium deformed by high pressure torsion. Journal of Materials Research and Technology. 2020;9:6642-54.

[118] Orlov D, Bhattacharjee PP, Todaka Y, Umemoto M, Tsuji N. Texture evolution in pure aluminum subjected to monotonous and reversal straining in high-pressure torsion. Scripta Materialia. 2009;60:893-6.

[119] Loucif A, Baudin T, Figueiredo RB, Brisset F, Helbert A-L, Chemam R, et al. Microstructure and microtexture evolution with aging treatment in an Al–Mg–Si alloy severely deformed by HPT. Journal of Materials Science. 2013;48:4573-81.

[120] Cepeda-Jiménez CM, Castillo-Rodríguez M, Molina-Aldareguia JM, Huang Y, Langdon TG, Pérez-Prado MT. Controlling the high temperature mechanical behavior of Al alloys by precipitation and severe straining. Materials Science and Engineering: A. 2017;679:36-47.

[121] Kong Y, Pu Q, Jia Z, Liu M, Roven HJ, Jia J, et al. Microstructure and property evolution of Al-0.4Fe-0.15Zr-0.25Er alloy processed by high pressure torsion. Journal of Alloys and Compounds. 2020;824:153949.

[122] Zhilyaev AP, Baró MD, Langdon TG, McNelley TR. An examination of microtexture and microstructure in ultrafine-grained nickel. Reviews on Advanced Materials Science. 2004;7:41-9.

[123] Korznikova EA, Mironov SY, Korznikov AV, Zhilyaev AP, Langdon TG. Microstructural evolution and electro-resistivity in HPT nickel. Materials Science and Engineering: A. 2012;556:437-45.

[124] Ghosh P, Renk O, Pippan R. Microtexture analysis of restoration mechanisms during high pressure torsion of pure nickel. Materials Science and Engineering: A. 2017;684:101-9.

[125] Hafok M, Pippan R. High-pressure torsion applied to nickel single crystals. Philosophical Magazine. 2008;88:1857-77.

[126] Wei P, Lu C, Tieu K, Su L, Deng G, Huang W. A study on the texture evolution mechanism of nickel single crystal deformed by high pressure torsion. Materials Science and Engineering: A. 2017;684:239-48.

[127] Enikeev NA, Schafler E, Zehetbauer M, Alexandrov IV, Valiev R. Observations of Texture in Large Scale HPT-Processed Cu. Materials Science Forum. 2008;584-586:367-74.

[128] Al-Fadhalah KJ, Alhajeri SN, Almazrouee AI, Langdon TG. Microstructure and microtexture in pure copper processed by high-pressure torsion. Journal of Materials Science. 2013;48:4563-72.

[129] Jahedi M, Paydar MH, Knezevic M. Enhanced microstructural homogeneity in metal-matrix composites developed under high-pressure-double-torsion. Materials Characterization. 2015;104:92-100.

[130] Korneva A, Straumal B, Kilmametov A, Chulist R, Straumal P, Zięba P. Phase transformations in a CuCr alloy induced by high pressure torsion. Materials Characterization. 2016;114:151-6.

[131] Ekiz EH, Lach TG, Averback RS, Mara NA, Beyerlein IJ, Pouryazdan M, et al. Microstructural evolution of nanolayered Cu–Nb composites subjected to high-pressure torsion. Acta Materialia. 2014;72:178-91.

[132] Chulist R, Czerny M, Panigrahi A, Zehetbauer M, Schell N, Skrotzki W. Texture and microstructure of HPT-processed Fe-based shape memory alloys. IOP Conference Series: Materials Science and Engineering. 2018;375:012006.

[133] Ivanisenko Y, Skrotzki W, Chulist R, Lippmann T, Yang K, Kurmanaeva L, et al. Information on deformation mechanisms in nanocrystalline Pd–10% Au inferred from texture analysis. Journal of Materials Science. 2010;45:4571-7.

[134] Skrotzki W, Eschke A, Jóni B, Ungár T, Tóth LS, Ivanisenko Y, et al. New experimental insight into the mechanisms of nanoplasticity. Acta Materialia. 2013;61:7271-84.

[135] Skrotzki W, Pukenas A, Joni B, Odor E, Ungar T, Hohenwarter A, et al. Microstructure and texture evolution during severe plastic deformation of CrMnFeCoNi high-entropy alloy. IOP Conference Series: Materials Science and Engineering. 2017;194:012028.

[136] Sonkusare R, Biswas K, Al-Hamdany N, Brokmeier HG, Kalsar R, Schell N, et al. A critical evaluation of microstructure-texture-mechanical behavior heterogeneity in high pressure torsion processed CoCuFeMnNi high entropy alloy. Materials Science and Engineering: A. 2020;782:139187.

[137] Murugesan AP, Rajinikanth V, Mahato B, Wegner M, Witte M, Wilde G, et al. Concurrent precipitation and associated texture evolution in AA 6082 alloy during high

pressure torsion (HPT) processing. Materials Science and Engineering: A. 2017;700:487-94.

[138] Lanjewar H, Naghdy S, Vercruysse F, Kestens LAI, Verleysen P. Severe plastically deformed commercially pure aluminum: Substructure, micro-texture and associated mechanical response during uniaxial tension. Materials Science and Engineering: A. 2019;764:138195.

[139] Kim BK, Szpunar JA, Zhilyaev AP. Annealing Texture in Thermal Stability of Ultrafine-Grained Ni. Materials Science Forum. 2002;408-412:943-8.

[140] Zhilyaev AP, Kim BK, Szpunar JA, Baró MD, Langdon TG. The microstructural characteristics of ultrafine-grained nickel. Materials Science and Engineering: A. 2005;391:377-89.

[141] Dillamore IL, Smallman RE, Roberts WT. A determination of the stacking-fault energy of some pure F.C.C. metals. The Philosophical Magazine: A Journal of Theoretical Experimental and Applied Physics. 1964;9:517-26.

[142] Okamoto NL, Fujimoto S, Kambara Y, Kawamura M, Chen ZMT, Matsunoshita H, et al. Size effect, critical resolved shear stress, stacking fault energy, and solid solution strengthening in the CrMnFeCoNi high-entropy alloy. Scientific Reports. 2016;6:35863.

[143] Liu SF, Wu Y, Wang HT, He JY, Liu JB, Chen CX, et al. Stacking fault energy of face-centered-cubic high entropy alloys. Intermetallics. 2018;93:269-73.

[144] Hughes DA, Lebensohn RA, Wenk HR, Kumar A. Stacking Fault Energy and Microstructure Effects on Torsion Texture Evolution. Proceedings: Mathematical, Physical and Engineering Sciences. 2000;456:921-53.

[145] Xu C, Horita Z, Langdon TG. The evolution of homogeneity in processing by high-pressure torsion. Acta Materialia. 2007;55:203-12.

[146] Kawasaki M. Different models of hardness evolution in ultrafine-grained materials processed by high-pressure torsion. Journal of Materials Science. 2014;49:18-34.

[147] Jiang H, Zhu YT, Butt DP, Alexandrov IV, Lowe TC. Microstructural evolution, microhardness and thermal stability of HPT-processed Cu. Materials Science and Engineering: A. 2000;290:128-38.

[148] Zhao YH, Liao XZ, Zhu YT, Horita Z, Langdon TG. Influence of stacking fault energy on nanostructure formation under high pressure torsion. Materials Science and Engineering: A. 2005;410-411:188-93.

[149] Skrotzki W, Pukenas A, Odor E, Joni B, Ungar T, Völker B, et al. Microstructure, Texture, and Strength Development during High-Pressure Torsion of CrMnFeCoNi High-Entropy Alloy. Crystals. 2020;10:336.

[150] Khereddine AY, Larbi FH, Kawasaki M, Baudin T, Bradai D, Langdon TG. An examination of microstructural evolution in a Cu–Ni–Si alloy processed by HPT and ECAP. Materials Science and Engineering: A. 2013;576:149-55.

[151] Harai Y, Ito Y, Horita Z. High-pressure torsion using ring specimens. Scripta Materialia. 2008;58:469-72.

[152] Furukawa M, Horita Z, Nemoto M, Valiev RZ, Langdon TG. Fabrication of submicrometer-grained Zn–22% Al by torsion straining. Journal of Materials Research. 1996;11:2128-30.

[153] Mazilkin AA, Straumal BB, Rabkin E, Baretzky B, Enders S, Protasova SG, et al. Softening of nanostructured Al–Zn and Al–Mg alloys after severe plastic deformation. Acta Materialia. 2006;54:3933-9.

[154] Mazilkin AA, Straumal BB, Borodachenkova MV, Valiev RZ, Kogtenkova OA, Baretzky B. Gradual softening of Al–Zn alloys during high-pressure torsion. Materials Letters. 2012;84:63-5.

[155] Zhang NX, Kawasaki M, Huang Y, Langdon TG. Microstructural evolution in two-phase alloys processed by high-pressure torsion. Journal of Materials Science. 2013;48:4582-91.

[156] Wang CT, He Y, Langdon TG. The significance of strain weakening and self-annealing in a superplastic Bi–Sn eutectic alloy processed by high-pressure torsion. Acta Materialia. 2020;185:245-56.

[157] Azzeddine H, Baudin T, Helbert A-L, Brisset F, Huang Y, Kawasaki M, et al. A stored energy analysis of grains with shear texture orientations in Cu-Ni-Si and Fe-Ni alloys processed by high-pressure torsion. Journal of Alloys and Compounds. 2021;864:158142.

[158] Kloeden B, Oertel CG, Skrotzki W, Rybacki E. Microstructure Development During High Strain Torsion of NiAl. Journal of Engineering Materials and Technology. 2009;131:0111011-9.

[159] Ivanisenko Y, Kurmanaeva L, Weissmueller J, Yang K, Markmann J, Rösner H, et al. Deformation mechanisms in nanocrystalline palladium at large strains. Acta Materialia. 2009;57:3391-401.

[160] Jahedi M, Beyerlein IJ, Paydar MH, Knezevic M. Effect of Grain Shape on Texture Formation during Severe Plastic Deformation of Pure Copper. Advanced Engineering Materials. 2018;20:1600829.

[161] Wetscher F, Vorhauer A, Pippan R. Strain hardening during high pressure torsion deformation. Materials Science and Engineering: A. 2005;410-411:213-6.

[162] Tóth LS, Neale KW, Jonas JJ. Stress response and persistence characteristics of the ideal orientations of shear textures. Acta Metallurgica. 1989;37:2197-210.

[163] Tóth LS, Jonas JJ, Daniel D, Bailey JA. Texture Development and Length Changes in Copper Bars Subjected to Free End Torsion. Textures and Microstructures. 1992;19:245-62.

[164] Esquivel EV, Murr LE. Grain boundary contributions to deformation and solid-state flow in severe plastic deformation. Materials Science and Engineering: A. 2005;409:13-23.

[165] Naghdy S, Percq LL, Serret R, Petrov R, Hertelé S, Kestens L, et al. Microstructural evolution study of severely deformed commercial aluminium by transmission Kikuchi diffraction. Materials Science and Technology. 2017;33:678-87.

[166] Shore D, Van Bael A, Sidor J, Roose D, Van Houtte P, Kestens L. Modelling the stored energy of plastic deformation for individual crystal orientations. IOP Conference Series: Materials Science and Engineering. 2015;82:012052.

[167] Figueiredo RB, Pereira PHR, Aguilar MTP, Cetlin PR, Langdon TG. Using finite element modeling to examine the temperature distribution in quasi-constrained high-pressure torsion. Acta Materialia. 2012;60:3190-8.

[168] Figueiredo RB, Cetlin PR, Langdon TG. Using finite element modeling to examine the flow processes in quasi-constrained high-pressure torsion. Materials Science and Engineering: A. 2011;528:8198-204.

[169] Horita Z, Langdon TG. Microstructures and microhardness of an aluminum alloy and pure copper after processing by high-pressure torsion. Materials Science and Engineering: A. 2005;410-411:422-5.

[170] Zhilyaev AP, Oh-ishi K, Langdon TG, McNelley TR. Microstructural evolution in commercial purity aluminum during high-pressure torsion. Materials Science and Engineering: A. 2005;410-411:277-80.

[171] Zhilyaev AP, Lee S, Nurislamova GV, Valiev RZ, Langdon TG. Microhardness and microstructural evolution in pure nickel during high-pressure torsion. Scripta Materialia. 2001;44:2753-8.

[172] Estrin Y, Molotnikov A, Davies CHJ, Lapovok R. Strain gradient plasticity modelling of high-pressure torsion. Journal of the Mechanics and Physics of Solids. 2008;56:1186-202.

[173] Yoon SC, Horita Z, Kim HS. Finite element analysis of plastic deformation behavior during high pressure torsion processing. Journal of Materials Processing Technology. 2008;201:32-6.

[174] Lee DJ, Yoon EY, Ahn D-H, Park BH, Park HW, Park LJ, et al. Dislocation density-based finite element analysis of large strain deformation behavior of copper under high-pressure torsion. Acta Materialia. 2014;76:281-93.

[175] Panda S, Toth LS, Fundenberger J-J, Perroud O, Guyon J, Zou J, et al. Analysis of heterogeneities in strain and microstructure in aluminum alloy and magnesium processed by high-pressure torsion. Materials Characterization. 2017;123:159-65.

[176] Sakai G, Nakamura K, Horita Z, Langdon TG. Developing high-pressure torsion for use with bulk samples. Materials Science and Engineering: A. 2005;406:268-73.

[177] Kawasaki M, Figueiredo RB, Langdon TG. An investigation of hardness homogeneity throughout disks processed by high-pressure torsion. Acta Materialia. 2011;59:308-16.

[178] Tirsatine K, Azzeddine H, Baudin T, Helbert A-L, Brisset F, Bradai D. On the recrystallization and texture of Fe-36%Ni alloy after accumulative roll bonding and annealing at 600 °C. Materials Engineering. 2017;24:56-66.

[179] Jonas JJ, Tóth LS. Modelling oriented nucleation and selective growth during dynamic recrystallization. Scripta Metallurgica et Materialia. 1992;27:1575-80.

[180] Doherty RD, Hughes DA, Humphreys FJ, Jonas JJ, Jensen DJ, Kassner ME, et al. Current issues in recrystallization: a review. Materials Science and Engineering: A. 1997;238:219-74.

[181] Zhang HW, Huang X, Pippan R, Hansen N. Thermal behavior of Ni (99.967% and 99.5% purity) deformed to an ultra-high strain by high pressure torsion. Acta Materialia. 2010;58:1698-707.

[182] Li S, Beyerlein IJ, Bourke MAM. Texture formation during equal channel angular extrusion of fcc and bcc materials: comparison with simple shear. Materials Science and Engineering: A. 2005;394:66-77.

[183] Zhao Y, Massion R, Grosdidier T, Toth LS. Gradient Structure in High Pressure Torsion Compacted Iron Powder. Advanced Engineering Materials. 2015;17:1748-53.

[184] Duan J, Wen H, Zhou C, Islamgaliev R, Li X. Evolution of microstructure and texture during annealing in a high-pressure torsion processed Fe-9Cr alloy. Materialia. 2019;6:100349.

[185] Chulist R, Skrotzki W, Oertel CG, Böhm A, Lippmann T, Rybacki E. Microstructure and texture in Ni50Mn29Ga21 deformed by high-pressure torsion. Scripta Materialia. 2010;62:650-3.

[186] Wang Y, Aktaa J. Microstructural evolution, textural evolution and thermal stabilities of W and W – 1 wt% La2O3 subjected to high-pressure torsion. Materialia. 2018;2:46-52.

[187] Chulist R, Böhm A, Rybacki E, Lippmann T, Oertel CG, Skrotzki W. Texture Evolution of HPT-Processed Ni50Mn29Ga21. Materials Science Forum. 2012;702-703:169-72.

[188] Tränkner C, Chulist R, Skrotzki W, Beausir B, Lippmann T, Horky J, et al. Influence of deformation temperature on texture evolution in HPT deformed NiAl. IOP Conference Series: Materials Science and Engineering. 2014;63:012154.

[189] Tränkner C, Pukenas A, Horky J, Zehetbauer M, Skrotzki W. Peculiarities in the Texture Formation of Intermetallic Compounds Deformed by High Pressure Torsion. MRS Proceedings. 2015;1760:mrsf14-1760-yy02-06.

[190] Wang Y, Aktaa J. Microstructure and texture in W and W-1wt%La2O3 processed by high-pressure torsion. Scripta Materialia. 2017;139:22-5.

[191] Renk O, Ghosh P, Pippan R. Generation of extreme grain aspect ratios in severely deformed tantalum at elevated temperatures. Scripta Materialia. 2017;137:60-3.

[192] Panigrahi A, Sulkowski B, Waitz T, Ozaltin K, Chrominski W, Pukenas A, et al. Mechanical properties, structural and texture evolution of biocompatible Ti–45Nb alloy processed by severe plastic deformation. Journal of the Mechanical Behavior of Biomedical Materials. 2016;62:93-105.

[193] Tränkner C, Chulist R, Skrotzki W, Lippmann T, Horky J, Zehetbauer M. Influence of hydrostatic pressure on texture evolution in HPT deformed NiAl. IOP Conference Series: Materials Science and Engineering. 2015;82:012026.

[194] Humphreys FJ, Hatherly M. Chapter 14 - Continuous Recrystallization During and after Large Strain Deformation. In: Humphreys FJ, Hatherly M, editors. Recrystallization and Related Annealing Phenomena (Second Edition). Oxford: Elsevier; 2004. p. 451-67.

[195] Duan J, Wen H, Zhou C, He X, Islamgaliev R, Valiev R. Annealing behavior in a high-pressure torsion-processed Fe–9Cr steel. Journal of Materials Science. 2020;55:7958-68.

[196] Beausir B, Tóth LS, Neale KW. Ideal orientations and persistence characteristics of hexagonal close packed crystals in simple shear. Acta Materialia. 2007;55:2695-705.

[197] Figueiredo RB, Langdon TG. Processing Magnesium and Its Alloys by High-Pressure Torsion: An Overview. Advanced Engineering Materials. 2019;21:1801039.

[198] Figueiredo RB, Cetlin PR, Langdon TG. Stable and Unstable Flow in Materials Processed by Equal-Channel Angular Pressing with an Emphasis on Magnesium Alloys. Metallurgical and Materials Transactions A. 2010;41:778-86.

[199] Cetlin PR, Aguilar MTP, Figueiredo RB, Langdon TG. Avoiding cracks and inhomogeneities in billets processed by ECAP. Journal of Materials Science. 2010;45:4561-70.

[200] Wang YN, Huang JC. Texture analysis in hexagonal materials. Materials Chemistry and Physics. 2003;81:11-26.

[201] Ivanisenko Y, Kilmametov A, Rösner H, Valiev RZ. Evidence of α → ω phase transition in titanium after high pressure torsion. International Journal of Materials Research. 2008;99:36-41.

[202] Ahmadkhaniha D, Huang Y, Jaskari M, Järvenpää A, Sohi MH, Zanella C, et al. Effect of high-pressure torsion on microstructure, mechanical properties and corrosion resistance of cast pure Mg. Journal of Materials Science. 2018;53:16585-97.

[203] Srinivasarao B, Zhilyaev AP, Langdon TG, Pérez-Prado MT. On the relation between the microstructure and the mechanical behavior of pure Zn processed by high pressure torsion. Materials Science and Engineering: A. 2013;562:196-202.

[204] Bourezg YI, Azzeddine H, Baudin T, Helbert A-L, Huang Y, Bradai D, et al. Texture and microhardness of Mg-Rare Earth (Nd and Ce) alloys processed by high-pressure torsion. Materials Science and Engineering: A. 2018;724:477-85.

[205] Lee H-J, Lee SK, Jung KH, Lee GA, Ahn B, Kawasaki M, et al. Evolution in hardness and texture of a ZK60A magnesium alloy processed by high-pressure torsion. Materials Science and Engineering: A. 2015;630:90-8.

[206] Torbati-Sarraf SA, Sabbaghianrad S, Figueiredo RB, Langdon TG. Orientation imaging microscopy and microhardness in a ZK60 magnesium alloy processed by high-pressure torsion. Journal of Alloys and Compounds. 2017;712:185-93.

[207] Jung I-H, Sanjari M, Kim J, Yue S. Role of RE in the deformation and recrystallization of Mg alloy and a new alloy design concept for Mg–RE alloys. Scripta Materialia. 2015;102:1-6.

[208] Sun WT, Qiao XG, Zheng MY, Xu C, Gao N, Starink MJ. Microstructure and mechanical properties of a nanostructured Mg-8.2Gd-3.8Y-1.0Zn-0.4Zr supersaturated solid solution prepared by high pressure torsion. Materials & Design. 2017;135:366-76.

[209] Bonarski BJ, Mikulowski B, Schafler E, Holzleithner C, Zehetbauer MJ. Crystallographic textures of single and polycrystalline pure Mg and Cu subjected to HPT deformation. Archives of Metallurgy and Materials. 2008;53:117-23.

[210] Kocich R, Kunčická L, Král P, Lowe TC. Texture, deformation twinning and hardening in a newly developed Mg–Dy–Al–Zn–Zr alloy processed with high pressure torsion. Materials & Design. 2016;90:1092-9.

[211] Huang Y, Figueiredo RB, Baudin T, Helbert A-L, Brisset F, Langdon TG. Microstructure and texture evolution in a magnesium alloy during processing by high-pressure torsion. Materials Research. 2013;16:577-85.

[212] Máthis K, Nyilas K, Axt A, Dragomir-Cernatescu I, Ungár T, Lukáč P. The evolution of non-basal dislocations as a function of deformation temperature in pure magnesium determined by X-ray diffraction. Acta Materialia. 2004;52:2889-94.

[213] Bonarski BJ, Schafler E, Mingler B, Skrotzki W, Mikulowski B, Zehetbauer MJ. Texture evolution of Mg during high-pressure torsion. Journal of Materials Science. 2008;43:7513-8.

[214] Kilmametov AR, Ivanisenko Y, Mazilkin AA, Straumal BB, Gornakova AS, Fabrichnaya OB, et al. The α→ω and β→ω phase transformations in Ti–Fe alloys under high-pressure torsion. Acta Materialia. 2018;144:337-51.

[215] Khaleghi AA, Akbaripanah F, Sabbaghian M, Máthis K, Minárik P, Veselý J, et al. Influence of high-pressure torsion on microstructure, hardness and shear strength of AM60 magnesium alloy. Materials Science and Engineering: A. 2021;799:140158.

[216] Bednarczyk W, Wątroba M, Kawałko J, Bała P. Can zinc alloys be strengthened by grain refinement? A critical evaluation of the processing of low-alloyed binary zinc alloys using ECAP. Materials Science and Engineering: A. 2019;748:357-66.

[217] Chen W, Xu J, Liu D, Bao J, Sabbaghianrad S, Shan D, et al. Microstructural Evolution and Microhardness Variations in Pure Titanium Processed by High-Pressure Torsion. Advanced Engineering Materials. 2020;22:1901462.

[218] Bednarczyk W, Kawałko J, Wątroba M, Gao N, Starink MJ, Bała P, et al. Microstructure and mechanical properties of a Zn-0.5Cu alloy processed by high-pressure torsion. Materials Science and Engineering: A. 2020;776:139047.

[219] Pinheiro TS, Gallego J, Bolfarini C, Kiminami CS, Jorge Jr. AM, Botta Filho WJ. Microstructural evolution of Ti-6Al-7Nb alloy during high pressure torsion. Materials Research. 2012;15:792-5.

[220] Bonarski BJ, Schafler E, Mikulowski B, Zehetbauer MJ. Effects of recrystallization on texture, microstructure and mechanical properties in HPT-deformed pure Mg. Journal of Physics: Conference Series. 2010;240:012133.

[221] Figueiredo RB, Langdon TG. Development of structural heterogeneities in a magnesium alloy processed by high-pressure torsion. Materials Science and Engineering: A. 2011;528:4500-6.

[222] Kawasaki M, Figueiredo RB, Langdon TG. Twenty-five years of severe plastic deformation: recent developments in evaluating the degree of homogeneity through the thickness of disks processed by high-pressure torsion. Journal of Materials Science. 2012;47:7719-25.

[223] Figueiredo RB, Langdon TG. The nature of grain refinement in equal-channel angular pressing: a comparison of representative fcc and hcp metals. International Journal of Materials Research. 2009;100:1638-46.

[224] Figueiredo RB, Langdon TG. Principles of grain refinement in magnesium alloys processed by equal-channel angular pressing. Journal of Materials Science. 2009;44:4758-62.

[225] Agnew SR, Tomé CN, Brown DW, Holden TM, Vogel SC. Study of slip mechanisms in a magnesium alloy by neutron diffraction and modeling. Scripta Materialia. 2003;48:1003-8.

[226] Basu I, Al-Samman T, Gottstein G. Shear band-related recrystallization and grain growth in two rolled magnesium-rare earth alloys. Materials Science and Engineering: A. 2013;579:50-6.

[227] Tighiouaret S, Hanna A, Azzeddine H, Rabahi L, Dakhouche A, Brisset F, et al. On the evolution of microstructure, texture and corrosion behavior of a hot-rolled and annealed AZ31 alloy. Materials Chemistry and Physics. 2021;267:124598.

[228] Su J, Yue S. Texture Weakening and Grain Refinement by High Speed Rolling and Annealing of an AZ31 Magnesium Alloy. In: Solanki KN, Orlov D, Singh A, Neelameggham NR, editors. Magnesium Technology 2017. Cham: Springer International Publishing; 2017. p. 547-54.

[229] Taylor GI. Plastic Strain in Metals. Journal of the Institute of Metals. 1938;62:307-24.

[230] Lebensohn RA, Tomé CN. A self-consistent anisotropic approach for the simulation of plastic deformation and texture development of polycrystals: Application to zirconium alloys. Acta Metallurgica et Materialia. 1993;41:2611-24.

[231] Molinari A, Tóth LS. Tuning a self consistent viscoplastic model by finite element results—I. Modeling. Acta Metallurgica et Materialia. 1994;42:2453-8.

[232] Molinari A, Canova GR, Ahzi S. A self consistent approach of the large deformation polycrystal viscoplasticity. Acta Metallurgica. 1987;35:2983-94.

[233] Li S, Beyerlein IJ, Alexander DJ, Vogel SC. Texture evolution during multi-pass equal channel angular extrusion of copper: Neutron diffraction characterization and polycrystal modeling. Acta Materialia. 2005;53:2111-25.

[234] Baik SC, Estrin Y, Hellmig RJ, Jeong HT, Brokmeier HG, Kim HS. Modeling of texture evolution in copper under equal channel angular pressing. Z Metallk. 2003;94:1189-98.

[235] Ferrasse S, Segal VM, Kalidindi SR, Alford F. Texture evolution during equal channel angular extrusion: Part I. Effect of route, number of passes and initial texture. Materials Science and Engineering: A. 2004;368:28-40.

[236] Li S, Beyerlein IJ, Necker CT, Alexander DJ, Bourke M. Heterogeneity of deformation texture in equal channel angular extrusion of copper. Acta Materialia. 2004;52:4859-75.

[237] Tóth LS, Arruffat Massion R, Germain L, Baik SC, Suwas S. Analysis of texture evolution in equal channel angular extrusion of copper using a new flow field. Acta Materialia. 2004;52:1885-98.

[238] Suwas S, Arruffat-Massion R, Tóth LS, Eberhardt A, Fundenberger J-J, Skrotzki W. Evolution of crystallographic texture during equal channel angular extrusion of copper: The role of material variables. Metallurgical and Materials Transactions A. 2006;37:739-53.

[239] Bolmaro RE, Renzetti RA, Sandim MJR, Sandim HRZ, Signorelli JW, Ferrante M. ECAP of Fe. Experiments and simulations of the in-elbow textures. Z Kristallogr Suppl. 2009;30:117-22.

[240] Basu S, Ravi Shankar M. Crystallographic Textures Resulting from Severe Shear Deformation in Machining. Metallurgical and Materials Transactions A. 2015;46:801-12.

[241] Beausir B, Suwas S, Tóth LS, Neale KW, Fundenberger J-J. Analysis of texture evolution in magnesium during equal channel angular extrusion. Acta Materialia. 2008;56:200-14.

[242] Segal VM. Materials processing by simple shear. Materials Science and Engineering: A. 1995;197:157-64.

[243] Tomé CN, Necker CT, Lebensohn RA. Mechanical anisotropy and grain interaction in recrystallized aluminum. Metallurgical and Materials Transactions A. 2002;33:2635-48.

[244] Beyerlein IJ, Lebensohn RA, Tomé CN. Modeling texture and microstructural evolution in the equal channel angular extrusion process. Materials Science and Engineering: A. 2003;345:122-38.

[245] Tóth LS, Beausir B, Gu CF, Estrin Y, Scheerbaum N, Davies CHJ. Effect of grain refinement by severe plastic deformation on the next-neighbor misorientation distribution. Acta Materialia. 2010;58:6706-16.

[246] Gu CF, Tóth LS. Texture development and grain refinement in non-equal-channel angular-pressed Al. Scripta Materialia. 2012;67:33-6.

[247] Gu CF, Tóth LS, Lapovok R, Davies CHJ. Texture evolution and grain refinement of ultrafine-grained copper during micro-extrusion. Philosophical Magazine. 2011;91:263-80.

[248] Vinogradov A, Estrin Y. Analytical and numerical approaches to modelling severe plastic deformation. Progress in Materials Science. 2018;95:172-242.

[249] Li S, Kalidindi SR, Beyerlein IJ. A crystal plasticity finite element analysis of texture evolution in equal channel angular extrusion. Materials Science and Engineering: A. 2005;410-411:207-12.

[250] Mathur KK, Dawson PR. On modeling the development of crystallographic texture in bulk forming processes. International Journal of Plasticity. 1989;5:67-94.

[251] Kalidindi SR, Bronkhorst CA, Anand L. Crystallographic texture evolution in bulk deformation processing of FCC metals. Journal of the Mechanics and Physics of Solids. 1992;40:537-69.

[252] Anand L, Kalidindi SR. The process of shear band formation in plane strain compression of fcc metals: Effects of crystallographic texture. Mechanics of Materials. 1994;17:223-43.

[253] Beaudoin AJ, Dawson PR, Mathur KK, Kocks UF. A hybrid finite element formulation for polycrystal plasticity with consideration of macrostructural and microstructural linking. International Journal of Plasticity. 1995;11:501-21.

[254] Li S, Houtte PV, Kalidindi SR. A quantitative evaluation of the deformation texture predictions for aluminium alloys from crystal plasticity finite element method. Modelling and Simulation in Materials Science and Engineering. 2004;12:845-70.

[255] Li S, Donohue BR, Kalidindi SR. A crystal plasticity finite element analysis of cross-grain deformation heterogeneity in equal channel angular extrusion and its implications for texture evolution. Materials Science and Engineering: A. 2008;480:17-23.

[256] Kalidindi SR, Donohue BR, Li S. Modeling texture evolution in equal channel angular extrusion using crystal plasticity finite element models. International Journal of Plasticity. 2009;25:768-79.

[257] Lu C, Deng GY, Tieu AK, Su LH, Zhu HT, Liu XH. Crystal plasticity modeling of texture evolution and heterogeneity in equal channel angular pressing of aluminum single crystal. Acta Materialia. 2011;59:3581-92.

[258] Pinna C, Lan Y, Kiu MF, Efthymiadis P, Lopez-Pedrosa M, Farrugia D. Assessment of crystal plasticity finite element simulations of the hot deformation of metals from local strain and orientation measurements. International Journal of Plasticity. 2015;73:24-38.

[259] Sheikh H, Ebrahimi R, Bagherpour E. Crystal plasticity finite element modeling of crystallographic textures in simple shear extrusion (SSE) process. Materials & Design. 2016;109:289-99.

[260] Sheikh H, Ebrahimi R. Modeling the effect of strain reversal on grain refinement and crystallographic texture during simple shear extrusion. International Journal of Solids and Structures. 2017;126-127:175-86.

[261] Li J, Yu R, Chen J, Li F, Liang S, Zhang M. Influence of Load Modes on the Characteristics of Severe Plastic Deformation Based on Crystal Plasticity Finite Element Method. Journal of Materials Engineering and Performance. 2021;30:1981-93.

[262] Wei PT, Lu C, Tieu K, Deng GY, Zhang J. Modelling of Texture Evolution in High Pressure Torsion by Crystal Plasticity Finite Element Method. Applied Mechanics and Materials. 2015;764-765:56-60.

[263] Jahedi M, Paydar MH, Zheng S, Beyerlein IJ, Knezevic M. Texture evolution and enhanced grain refinement under high-pressure-double-torsion. Materials Science and Engineering: A. 2014;611:29-36.

[264] Jahedi M, Knezevic M, Paydar MH. High-Pressure Double Torsion as a Severe Plastic Deformation Process: Experimental Procedure and Finite Element Modeling. Journal of Materials Engineering and Performance. 2015;24:1471-82.

[265] Poudens A, Bacroix B, Bretheau T. Influence of microstructures and particle concentrations on the development of extrusion textures in metal matrix composites. Materials Science and Engineering: A. 1995;196:219-28.

[266] Hirsch J, Nes E, Lücke K. Rolling and recrystallization textures in directionally solidified aluminium. Acta Metallurgica. 1987;35:427-38.

[267] Wetscher F, Pippan R. Cyclic high-pressure torsion of nickel and Armco iron. Philosophical Magazine. 2006;86:5867-83.

[268] Wetscher F, Tian BH, Stock R, Pippan R. High Pressure Torsion of Rail Steels. Materials Science Forum. 2006;503-504:455-60.

[269] Todaka Y, Umemoto M, Yamazaki A, Sasaki J, Tsuchiya K. Effect of Strain Path in High-Pressure Torsion Process on Hardening in Commercial Purity Titanium. Materials Transactions. 2008;49:47-53.

[270] Kawasaki M, Langdon TG. The significance of strain reversals during processing by high-pressure torsion. Materials Science and Engineering: A. 2008;498:341-8.

[271] Wetscher F, Pippan R. Hardening and Softening Behavior by Cyclic High-Pressure Torsion. Metallurgical and Materials Transactions A. 2009;40:3258.

[272] Kawasaki M, Ahn B, Langdon TG. Effect of strain reversals on the processing of high-purity aluminum by high-pressure torsion. Journal of Materials Science. 2010;45:4583-93.

[273] Kawasaki M, Ahn B, Langdon TG. Significance of strain reversals in a two-phase alloy processed by high-pressure torsion. Materials Science and Engineering: A. 2010;527:7008-16.

[274] Zhang J, Gao N, Starink MJ. Microstructure development and hardening during high pressure torsion of commercially pure aluminium: Strain reversal experiments and a dislocation based model. Materials Science and Engineering: A. 2011;528:2581-91.

[275] Zhang J, Starink MJ, Gao N, Zhou W. Effect of Mg addition on strengthening of aluminium alloys subjected to different strain paths in high pressure torsion. Materials Science and Engineering: A. 2011;528:2093-9.

[276] Orlov D, Todaka Y, Umemoto M, Tsuji N. Formation of bimodal grain structures in high purity Al by reversal high pressure torsion. Scripta Materialia. 2011;64:498-501.

[277] Zhang JW, Starink MJ, Gao N, Zhou WL. Influence of Strain Reversals during High Pressure Torsion Process on Strengthening in Al-Cu-Mg(-Li) Alloy. Materials Science Forum. 2011;667-669:809-14.

[278] Chadha K, Bhattacharjee P, Jahazi M. The Effect of Strain Reversal during High Pressure Torsion on the Microstructure Evolution and Texture of Aluminum Alloys. In: Carpenter JS BC, Escobedo JP, Hwang JY, Ikhmayies S, Li B, Li J, Monteiro SN, Peng

Z, Zhang M, editor. Characterization of Minerals, Metals, and Materials 2015. Pittsburgh, PA, USA: TMS; 2015. p. 107-14.

[279] Ma X, Li F, Mao X, Yuan S, Wang J. Effect of strain reversal on microstructure and mechanical properties of Ti-6Al-4V alloy under cyclic torsion deformation. Procedia Engineering. 2017;207:1469-74.

[280] Montazerolghaem H, Mohammadzadeh M. Experimental study on effect of reverse rotation on micro-hardness value of high-pressure torsion processed samples. Procedia Manufacturing. 2018;15:1509-16.

[281] Sonkusare R, Khandelwal N, Ghosh P, Biswas K, Gurao NP. A comparative study on the evolution of microstructure and hardness during monotonic and cyclic high pressure torsion of CoCuFeMnNi high entropy alloy. Journal of Materials Research. 2019;34:732-43.

[282] Orlov D, Todaka Y, Umemoto M, Tsuji N. Role of strain reversal in grain refinement by severe plastic deformation. Materials Science and Engineering: A. 2009;499:427-33.

[283] Tóth LS, Arzaghi M, Fundenberger JJ, Beausir B, Bouaziz O, Arruffat-Massion R. Severe plastic deformation of metals by high-pressure tube twisting. Scripta Materialia. 2009;60:175-7.

[284] Lapovok R, Pougis A, Lemiale V, Orlov D, Toth LS, Estrin Y. Severe plastic deformation processes for thin samples. Journal of Materials Science. 2010;45:4554-60.

[285] Toth LS, Chen C, Pougis A, Arzaghi M, Fundenberger J-J, Massion R, et al. High Pressure Tube Twisting for Producing Ultra Fine Grained Materials: A Review. Materials Transactions. 2019;60:1177-91.

[286] Tazoe K, Honda S, Horita Z. Application of High-Pressure Sliding for Grain Refinement of Al and Mg Alloys. Materials Science Forum. 2011;667-669:91-6.

[287] Lee S, Tazoe K, Mohamed IF, Horita Z. Strengthening of AA7075 alloy by processing with high-pressure sliding (HPS) and subsequent aging. Materials Science and Engineering: A. 2015;628:56-61.

[288] Horita Z. Severe Plastic Deformation under High Pressure for Production of Superplastic Materials. Materials Science Forum. 2016;838-839:287-93.

[289] Takizawa Y, Masuda T, Fujimitsu K, Kajita T, Watanabe K, Yumoto M, et al. Scaling up of High-Pressure Sliding (HPS) for Grain Refinement and Superplasticity. Metallurgical and Materials Transactions A. 2016;47:4669-81.

[290] Takizawa Y, Kajita T, Kral P, Masuda T, Watanabe K, Yumoto M, et al. Superplasticity of Inconel 718 after processing by high-pressure sliding (HPS). Materials Science and Engineering: A. 2017;682:603-12.

[291] Takizawa Y, Sumikawa K, Watanabe K, Masuda T, Yumoto M, Kanai Y, et al. Incremental Feeding High-Pressure Sliding for Grain Refinement of Large-Scale Sheets: Application to Inconel 718. Metallurgical and Materials Transactions A. 2018;49:1830-40.

[292] Tang Y, Sumikawa K, Takizawa Y, Yumoto M, Otagiri Y, Horita Z. Multi-pass high-pressure sliding (MP-HPS) for grain refinement and superplasticity in metallic round rods. Materials Science and Engineering: A. 2019;748:108-18.

Figure captions

Figure 1: Illustrations showing the principles of ECAP, ARB and HPT processing.

Figure 2: Effect of different texture component on the R-value as a function of orientation with respect to the rolling direction of the sheet: a) Copper {112}<111> and Brass {110}<112> (deformation components, b) Cube {001}<100> and Goss {110}<100> (recrystallization components) and c) A{111}<110>, A* {111}<112> and C {001}<110> (shear components) [88].

Figure 3: ODF sections at φ_2 = 0 and 45 ° and {111} pole figures showing the positions of the ideal shear texture components on the SD-RD, SD-CD and CD-RD planes for materials with FCC structure.

Figure 4: ODF sections at φ_2 = 45° showing the texture difference between HPT-processed (a) pure Al for ε_{eq} = 7.97 (measured by EBSD) [116], (b) pure Cu for ε_{eq} = 254 (measured by XRD) [127], (c) CrMnFeCoNi alloy for ε_{eq} = 9.23 (measured by XRD) [135] and (d) ideal position of the shear texture components.

Figure 5: (a) Schematic illustration of hardening models: without recovery, with recovery and softening for materials processed by HPT [146], experimental example (b) of hardening with recovery of pure Al processed by HPT [151], (c) hardening without recovery of Cu-2.5Ni-Si alloy processed by HPT and ECAP [150] and (d) CrMnFeCoNi high entropy alloy processed by HPT [149].

Figure 6: Recalculated {111} pole figure of Cu-2.5Ni-0.6Si and Fe-36Ni alloys after HPT proceeding at RT through N = 1/2, 1, 5 and 10 turns [157]. Pole figures were presented in equal area projection.

Figure 7: Texture evolution of Pd-10Au alloy after HPT processing for N = ½ turn (ε_{eq}= 7.67) with different initial grain size: based on an earlier report [133].

Figure 8: ODF sections at φ_2 = 45° for as-quenched, aged at 473 K and aged at 523 K Al-0.6Mg-0.4Si alloy processed by HPT for N = 1, 5 and 20 turns, respectively [119]. Reproduced with permission.

Figure 9: Instability of the texture during earlier stage of processing showing by ODF sections at φ_2 = 45° of CP Al alloy after HPT processing at ε_{eq} of: (a) 0.45, (b) 0.90, (c) 1.34, (d) 2.69, (e) 5.38, (f) 10.76, (g) 21.51, (h) 32.27 and (i) 53.78 [117]. Reproduced with permission.

Figure 10: (a) Engineering stress-strain curves of annealed and HPT processed CP Al, (b) evolution of (c) shear texture components (c) radial and thickness strain and (d) texture index as a function of equivalent strain [138].

Figure 11 : Evolution of the stored energy in the shear texture components as a function of number of HPT turns of the: (a) Cu-2.5Ni-0.6Si and (b) Fe-36Ni alloy [157].

Figure 12: (a) Distribution of HPT-disc areas, where the texture measurements were performed and (b) ODF sections at φ_2 = 45° near the center, half-radius and near the edge of the disc of Cu-2.5Ni-0.6Si alloy after processing by HPT through 1/2, 1, 5 and 10 turns [72]. Reproduced with permission.

Figure 13: (a, b) evolution of the microstructure and mean grain size of Cu-2.5Ni-0.6Si alloy after HPT at the center, middle and near edge after processing through 1/2, 1, 5 and 10 turns [72] and (c) evolution of Vickers microhardness with distance from the center of the HPT processed discs [150].

Figure 14: (a) Schematic illustration of cross-sectional plane of one-half of an HPT-disc showing the positions selected for Vickers microhardness and EBSD measurements. EBSD orientation maps and the corresponding {111} pole figures measured at the edge of the disc: (b) top, (c) middle and (d) bottom sections. (e) Strain distribution across the through-thickness and (f) distributions of Vickers microhardness

in the radial direction across the through-thickness in Al (A5086) alloy processed at RT for 270° rotation (N = 3/4 turn) [175]. Reproduced with permission.

Figure 15: Evolution of the texture index value of Fe-36Ni alloy after HPT processing up 10 turns at RT and 523 K [54] . Reproduced with permission.

Figure 16: ODF sections at φ_2 = 0 and 45° of HPT processed pure Ni at 77, 300, 523 and 673 K, respectively [124]. Ideal positions of the shear texture components and Oblique Cube are also presented. Reproduced with permission.

Figure 17: ODF sections at φ_2 = 0 and 45 ° and {110} pole figures showing the position of ideal shear texture components on the SD-RD, SD-CD, CD-RD planes for materials with BCC structure.

Figure 18: ODF sections at φ_2 = 0 and 45° of NiAl intermetallic processed by HPT to $\varepsilon_{eq} \approx 34.6$ at: (a) RT and (b) 773 K [188].

Figure 19: ODF sections at φ_2 = 0 and 45° for pure tantalum HPT processed (ε_{eq} = 136) for different temperatures [191]. Reproduced with permission.

Figure 20: A schema illustrates the evolution of the microstructure and texture in W and WL10 alloys during HPT processing [186].

Figure 21: Variation of (a) shear strain, (b) microhardness, (c) Optical micrograph, across the thickness of the HPT Fe consolidated disc and (d) the corresponding {110} pole figure in the three distinct deformation zones: U, T and S-zones [183]. Pole figures were presented in stereographic projection Reproduced with permission.

Figure 22: φ_2 = 45° ODF sections of Fe-9Cr alloy: (a) processed by HPT at 573 K for N = 10 turns, followed by annealing at 873 K for (b) 6 h and (c) 24 h. (d) represents the key figure of ideal shear components of BCC materials [184]. Reproduced with permission.

Figure 23: (a-c) grain size distribution of Fe-9Cr alloy after HPT processing at 573 K for N = 10 turns and subsequent annealing at 873 °C for 6 and 24 h. EBSD maps showing grains with *J* orientation (highlighted in red color) having the larger average size, (a'- c') schematic illustrations of the changes in microstructure and texture in HPT-processed Fe-9Cr alloy during annealing [184].

Figure 24: ODF sections at φ_2 = 0 and 30 ° and {0002} and $\{10\bar{1}0\}$ pole figures showing the position of ideal shear texture components on SD-RD, SD-CD, CD-RD planes for materials with HCP structure.

Figure 25: {0002} pole figure of pure : (a) Ti [201], (b) Mg [202] and (c) Zn [203] after HPT processing at RT through N = 5 turns. Reproduced with permission for Zn.

Figure 26: Texture difference presented by the {0002} recalculated pole figures between the as-cast and as-extruded CP Mg after HPT processing at N = 1/8 turn [67]. Reproduced with permission.

Figure 27: {0002} recalculated pole figures of AZ31 alloy processed by HPT for N = 1 and 5 turns at RT, 373 and 473 K, respectively [211].

Figure 28: {0002} pole figure evolution in pure Mg as a function of the hydrostatic pressure and shear strain imposed during HPT processing: modified from [213].

Figure 29: Strain-stress curves and the corresponding texture evolution of AM60 alloy as a function of number of HPT turns [215].

Figure 30 : Evolution of microhardness and texture intensity as a function of equivalent strain for pure Ti (a) [217], Mg-0.41Dy (b, c) [68] and Zn-0.5Cu (d, e) [218] alloys.

Figure 31: The measured yield strength as a function of the calculated values for AM60 alloys processed by ECAP, MDF and HPT [215] and for Mg-0.41Dy alloy processed by HPT [68].

Figure 32: Basal {0002} pole figures near the center, middle and the edge of the discs of the Mg-0.41Dy (wt. %) alloy processed by HPT at RT to N = 1, 5 and 15 turns [68]. Reproduced with permission.

Figure 33: Grain orientation spread maps of the HPT processed Mg-0.41Dy alloy and the {0002} corresponding pole figures showing the orientation of the deformed and recrystallized grains obtained by grain orientation spread (GOS) approach [68].

Figure 34: {0002} pole figures of AZ60A alloy at edge position: (a) initial state (as-extruded), (b) after compression under 6.0 GPa without torsion straining and (c) after HPT processing for N =1/2 under P = 6.0 GPa [205]. Reproduced with permission.

Figure 35: Color-coded maps showing the microhardness distributions across the one-half cross-sections of discs of AZ31 alloy after processing by HPT at 296 and 463 K for 1/4, 1, and 5 turns, respectively [221, 222].

Figure 36: (a) Schematic illustration of cross-sectional plane of one-half of an HPT-disc showing the positions selected for Vickers microhardness and EBSD measurements. EBSD orientation maps and the corresponding {0002} pole figures measured at the edge of the disc: (b) top, (c) middle and (d) bottom sections. (e) Strain distribution across the through-thickness and (f) distributions of Vickers microhardness in the radial direction across the through-thickness in pure Mg processed at RT for 270° rotation (N = 3/4 turn) [175]. Reproduced with permission.

Figure 37: Evolution of texture, grain size and microhardness as a function of annealing temperature of the HPT processes at N = 5 turns [10].

Figure 38: Evolution of texture as a function of number of ECAP passes via route Bc. (a) experimental results and simulated resulted by: (b) FC/SS, (c) FC/FE, (d) SC/SS, (e) SCR/SS, (f) SCRD/SS and (g) SCRD/FE methods (see Table 11) [233]. Contours: 1/1.4/2.8/4/5.6/8/11/16/22. Reproduced with permission.

Figure 39: (a) Experimental and (b) predicted {100} pole figures for micro-extruded ultra-fine grains copper [247, 248]. Contours: 1.2/2/2.5/3/3.5/4/8/12/20. Reproduced with permission.

Figure 40: Typical morphologies for orientation evolution induced grain coarsening events obtained by 3D simulation [98].

Figure 41: Experimental and predicted texture evolution using VPSC and Taylor models after HPT processing of CP Al at ε_{eq} = 0.75 and 4 [116].

Figure 42: Scheme of: (a) high pressure double torsion (HPDT), (b) reversal high pressure torsion (RHPT), (c) high pressure tube twisting (HPTT), (d) high pressure shearing (HPS) and (e) high pressure compressive shearing (HPCS).

Figure 43: Evolution of the texture of CP Cu discs processed by HPT and HPDT as a function of the disk location and the numbers of turns [263]. Reproduced with permission.

Figure 44: {111} pole figures of the pure Al after monotonous (HPT) processing (a-d), RHPT processing (e-h) and the ideal position of the shear component in the {111} pole figure (i) [118]. Reproduced with permission.

Figure 45: ODF sections at φ_2 = 0 and 45 ° at (a) the internal and (b) external surfaces of the tube of CP Al alloy after HPTT processing for an average shear of 2 [34]. Reproduced with permission.

Figure 46: ODF sections at φ_2 = 0 and 45 ° of ARMCO steel (BCC) after HPCS processing at RT through: (a) pass and (b) 3 passes [39]. Reproduced with permission.

Table 1. Position of ideal shear texture components for FCC materials projected in the SD-RD, SD-CD and CD-RD planes.

Notation	**SD-RD plane**		**SD-CD plane**		**CD-RD plane**	
	Miller indice {hkl}<uvw>	Euler angles (°) (φ_1, Φ, φ_2)	Miller indice {hkl}<uvw>	Euler angles (°) (φ_1, Φ, φ_2)	Miller indice {hkl}<uvw>	Euler angles (°) (φ_1, Φ, φ_2)
A	{1$\bar{1}$1}<110>	(60, 54.7, 45)	{112}<1$\bar{1}$0>	(0, 35.2, 45)	{110}<1$\bar{1}$2>	(54.7, 90, 45)
$\bar{\boldsymbol{A}}$	{$\bar{1}$1$\bar{1}$}<$\bar{1}\bar{1}$0>	(120, 54.7, 45)	{211}<0$\bar{1}$1>	(50.7, 65.9, 63.4)	{101}<$\bar{1}\bar{2}$1>	(35.26, 45, 90)
$\boldsymbol{A_1^*}$	{11$\bar{1}$}<112>	(90, 54.7, 45)	{101}<$\bar{1}\bar{2}$1>	(35.26, 45, 90)	{121}<$\bar{1}$01>	(129.23, 65.9, 26.5)
$\boldsymbol{A_2^*}$	{11$\bar{1}$}<2$\bar{1}$1>	(30, 54.7, 45)	{011}<$\bar{2}\bar{1}$1>	(144.7, 45, 0)	{211}<0$\bar{1}$1>	(50.7, 65.9, 63.4)
B	{1$\bar{1}$2}<110>	(50.7, 65.9, 63.4)	{111}<1$\bar{1}$0>	(0, 54.7, 45)	{110}<1$\bar{1}$1>	(35.26, 90, 45)
$\bar{\boldsymbol{B}}$	{$\bar{1}$1$\bar{2}$}<$\bar{1}\bar{1}$0>	(0, 35.26, 45)	{111}<0$\bar{1}$1>	(60, 54.7, 45)	{101}<$\bar{1}\bar{1}$1>	(54.7, 45, 90)
C	{001}<110>	(45, 0, 0)	{110}<1$\bar{1}$0>	(0, 90, 45)	{011}<0$\bar{1}$1>	(90, 45, 0)

Table 2. Major texture observations in FCC materials as a function of HPT processing conditions.

Alloy	Experimental conditions	Major texture observations	Ref.
Commercial Purity (CP) Al	P= 2.5 GPa, V = 1 rpm, RT N = 1/8, 1/2, 1 and 5 turns EBSD at the mid-radius of the discs	ε_{eq}= 0.75–5.31: typical shear texture (weak *A*-fiber, strong *B*-fiber with *C* domination) ε_{eq}= 7.97–99: texture weakening	[116]
CP Al	P= 6 GPa, V = 0.5 rpm, RT N = 1/24,1/12, 1/8, 1/4, 1/2, 1, 2 and 5 turns EBSD at the mid-radius and edge of the discs	ε_{eq}= 0.45: no shear texture ε_{eq}= 0.9–21.51: gradual formation of typical shear texture ε_{eq}= 32.27–53.38: texture weakening	[117]
Pure Al (99.99%)	P= 5 GPa, V = 0.2 rpm, RT N = 1/8 and 1 turn EBSD at the mid-radius and edge of the discs	ε_{eq}= 1–4: gradual formation of typical shear texture ε_{eq}= 8: texture weakening	[118]
Al-Mg-Si	P= 6 GPa, V = 1 rpm, RT N = 1, 5, 10 and 20 turns EBSD at the mid-radius of the discs	As quenched condition: ε_{eq}= 11.3: presence of *C* and A_1^* ε_{eq}= 56.65–226.6: texture weakening Aged at 473K condition: ε_{eq}= 11.3–54.65: presence of *C* and A_1^* ε_{eq}= 56.65–226.6: Texture strength and domination of A_1^* Aged at 523K condition: ε_{eq}= 11.3–56.65: presence of *C* and *A*-fiber ε_{eq}= 226.6: texture weakening	[119]
AA6082	P= 2 GPa, V = 0.5 rpm, RT N = 1, 3 and 5 turns XRD at the center, mid-radius and edge of the discs	ε_{eq}= 1.81–108.77: stable texture with the presence of *C*, A_1^* and $A/\bar{A}$	[137]
AA6082	P= 6 GPa, V = 1 rpm, RT N = 5 turns EBSD at the center and edge of the disc	As cast condition: ε_{eq}= 3.6: typical shear texture (weak *A*-fiber, strong *B*-fiber with *C* domination) ε_{eq}= 81.4: weak to near random texture Aged T6 condition (803 K for 1h + 453 K for 6h): ε_{eq}= 3.6: domination of *C* ε_{eq}= 81.4: weak to near random texture	[120]

Al-Fe-Zr-Er	P= 6 GPa, V = 1 rpm, RT N = 1/4, 1/2, 1, 5 and 20 turns EBSD at the edge of the discs	ε_{eq}= 3.23: presence of C and $A/\bar{A}$ ε_{eq}= 6.47–258.9: formation of {112}<111> and texture weakening	[121]
Pure Ni	P= 6 GPa, V = 1 rpm, RT N = 5 turns (ε_{eq}= 4.53–113) EBSD measurement but without an indication of the position from the disc	HPT typical shear texture (weak *A*-fiber, strong *B*-fiber with *C* domination) ECAP+HPT Similar texture but with some deviation from their ideal position	[122]
Pure Ni	P= 4 GPa, V = 2.5 rpm, RT N = 1/10, 1/4, 1/2, 1 and 5 turns EBSD at the mid-radius of the discs	ε_{eq}= 4.53–11.33: gradual formation of typical shear texture (weak *A*-fiber, strong *B*-fiber with *C* domination) ε_{eq}= 22.66–226.6: stable texture	[123]
Pure Ni	P= 5GPa, V = 0.2 and 0.6 rpm, T = 77, 300, 523 and 673K N = 10 turns EBSD at the center of the discs	At 77–300 K Typical shear texture (weak *A*-fiber, strong *B*-fiber with C domination) At 523–673 K C disappears and Oblique Cube appears	[124]
Single crystal Ni	P= 2.3 GPa, V = 0.025 min^{-1}, RT Φ = 22.5°, 45°, 60° and 125° revolution angles EBSD at the edge of the discs	ε_{eq} < 1: the initial A_2^* component is stable ε_{eq}= 2–5: A_2^* transforms to *C* component ε_{eq} > 5: *C* transforms to A_1^* component	[125, 126]
Pure Cu	P = 6 GPa, RT, N = 10 turns XRD at the mid-radius and edge of the disc	ε_{eq}= 127: weak *A*-fiber, strong *B*-fiber with the domination of $B/\bar{B}$ ε_{eq}= 254: similar texture	[127]
Pure Cu	P= 6 GPa, V = 1 rpm, RT N = 1/4, 1/2 and 5 turns EBSD at the center, mid-radius and edge of the discs	ε_{eq}= 0.22–2.8: presence of *C*, A_1^* and A_2^* ε_{eq}= 5.66–11.3: domination of Cube ε_{eq}= 22.6–113: presence of *A* and *B* fibers and weak *C*	[128]
Pure Cu and Cu matrix composite	P= 3 GPa, V = 0.2 rpm, RT N = 2, 4 and 6 turns XRD at the mid-radius and edge of the discs	Composite ε_{eq}= 14.5–23.3: gradual formation of *A* and *B* fibers with the domination of $B/\bar{B}$ ε_{eq}= 46.7–72.5: texture weakening Pure Cu ε_{eq}= 29: presence of full of *A* and *B* fibers	[129]
Cu-Cr	P = 5GPa, V = 1 rpm, RT N = 5 turns	Annealed at 823 K for 2300h presence of *A* and *B* fibers with domination of A_2^* and $B/\bar{B}$	[130]

	EBSD at r = 3 mm from the center of the disc	Annealed at 1273 K for 384h presence of *A* and *B* fibers with domination of A_2^* and $B/\bar{B}$	
Cu-Ni-Si	P= 6 GPa, V = 1 rpm, RT N = 1/2, 1, 5 and 10 turns EBSD at the center, mid-radius and edge of the discs	ε_{eq}= 0.45–5.66: gradual formation of *A* and *B* fibers ε_{eq}= 11.3–56.65: stable texture ε_{eq}= 101–203: *A*-fiber with the domination of A_2^*	[72]
Cu/Nb composite	P = 4.5GPa, V = 1.2rpm, RT N = 50°, 210°, 5 turns and 20 turns XRD measurement a cross the radii of the discs	Cu layer ε_{eq}= 2.42–6.23: near-random texture ε_{eq}= 10.8–165.1: complete *A*-fiber ε_{eq}= 1437–2592: domination of A_1^*	[131]
Fe-Ni	P= 6 GPa, V = 1 rpm, RT and 523 K N = 1/2, 1, 5 and 10 turns EBSD at the mid-radius of the discs	At RT ε_{eq}= 5.66–56.6: presence of all shear components with the domination of *B* ε_{eq}= 113.3: stable texture At 523 K ε_{eq}= 5.66:–113.3: weakening of the texture but the presence of *C*	[54]
Fe-based shape memory	P = 8 GPa, RT, N = 2 turns synchrotron XRD at the mid-radius of the disc	ε_{eq}= 9.06: presence of *C*	[132]
Pd-Au	P= 4.5 GPa, V = π/2 per 18 s^{-1}, RT N = 1/2 turn synchrotron XRD at the mid-radius of the discs	Initial nano-grain ε_{eq}= 7.67: presence of A_2^* and Cube Initial coarse-grain ε_{eq}= 7.67: typical shear texture (weak *A*-fiber, strong *B*-fiber with *C* domination)	[133]
Pd-Au	P= 6 GPa, V = 6°s^{-1}, RT N = 7, 36 and 104° rotation angle XRD at the edge of the discs	ε_{eq}= 0–0.4: near-random texture ε_{eq}= 0.57–1.61: formation of A_2^*, $B/\bar{B}$ and *C* ε_{eq}= 2.42–9.69: domination of $B/\bar{B}$	[134]
CrMnFeCoNi high-entropy alloy	V = 0.2 rpm, RT N = 1 and 5 turns XRD at the mid-radius and the edge of the discs	ε_{eq}= 9.23–75: presence of A_1^*, A_2^* and strong $B/\bar{B}$	[135]
CoCuFeMnNi high entropy alloy	P = 5 GPa, RT, N = 5 turns synchrotron XRD across the whole radius of the discs	ε_{eq}= 0–22.6: gradual formation of shear texture ε_{eq}= 45.3–67.9: typical shear texture with the domination of *A* and A_1^* ε_{eq}= 90.6: texture weakening	[136]

Table 3. General texture observations correlated with deformation mechanisms and hardening models as a function of γ_{SFE} values for FCC materials.

	Texture observations	Deformation mechanisms	Hardening model
High γ_{SFE}	Formation weak A-fiber, strong B-fiber with the domination of *C* component which randomized with increasing shear strain	dislocation slip and grain refinement and/or grain boundary sliding at high shear strain	strain hardening with recovery
Medium γ_{SFE}	Formation of strong B-fiber with the domination of $B/\bar{B}$ components which keeps stable with increasing shear strain	dislocation slip and some twinning	strain hardening without recovery
Low γ_{SFE}	Formation of weak A_1^*, A_2^* and $B/\bar{B}$ components which keeps stable with increasing shear strain	twinning with partial dislocation slip and grain boundary sliding at high shear strain	strain hardening without recovery

Table 4. Evolution of fraction of different grain boundary misorientations in the shear components for Cu-2.5Ni-0.6Si and Fe-36Ni alloys after HPT processing for N = 10 turns [157].

	$\boldsymbol{A_1^*}$	$\boldsymbol{A_2^*}$	*A*	$\boldsymbol{\bar{A}}$	*B*	$\boldsymbol{\bar{B}}$	*C*
Cu-2.5Ni-0.6Si							
2–5° (%)	71.0	69.0	71.2	73.9	71.2	74.0	72.7
5–15°(%)	24.8	26.4	25.2	23	24.7	23.4	24.4
>15°(%)	4.2	4.6	3.7	3.2	4.1	2.6	2.9
Fe-36Ni							
2–5°(%)	69.9	75.3	72.1	74.8	63.8	63.8	68.6
5–15°(%)	15.1	11.6	13.2	12.2	18.5	18.1	17.0
>15°(%)	15.0	13.1	14.7	13.0	17.7	18.0	14.4

Table 5. Microstructural (grain size and HAGBs), microhardness and texture observations after HPT processing as a function of initial heat treatments.

		Before HPT processing	After HPT processing					
	Heat treatment	Microstructural observations		Texture observations	d (nm)	HAGBs (%)	Hv	Microstructural observation
Al [120]	As-cast	needle-shaped stable precipitates (Mg_2Si) of 500 nm in length	low strain (ε_{eq} = 3.63)	typical shear texture of high γ_{SFE}	786	43	107	-
			high strain (ε_{eq} = 81.4)	near-random texture	256	84	156	fragmented into many small precipitates having sizes ranging ~5 and 25 nm
	T6 (623K for 1 h + 453K for 6 h)	nanoscale particles with 10 nm of length	low strain (ε_{eq} = 3.63)	domination of *C* component	348	56	150	-
			high strain (ε_{eq} = 81.4)	near-random texture	251	76	158	sheared and partially dissolved
Cu-Cr [130]	Heating at 823K for 2300 h	large particle of 500 nm at boundaries and small particles of 70 nm uniformly distributed into the Cr matrix	High strain (ε_{eq} = 213)	typical shear texture of medium γ_{SFE}	450	92	159	partial dissolution of Cr precipitates
	Heating at 1273K for 384 h	small amount of large particle of 2 μm uniformly distributed into the Cr matrix	high strain (ε_{eq} = 213)	typical shear texture of medium γ_{SFE}	350	88	170	dissolution of residual Cr precipitates and weak decomposition of the supersaturated solid solution

Table 6. Evolution of mean grain size and HAGBs of Fe-36Ni alloy after HPT processing at RT and 523K [54].

Fe-36Ni	N = 1/2	N = 1	N = 5	N = 10
HPT at RT				
grain size (μm)	2.03	0.93	0.32	0.3
HAGBs (%)	23	29	56.8	58
HPT at 523K				
grain size (μm)	2.15	0.81	0.24	0.24
HAGBs (%)	24	28	66.1	66.5

Table 7. Evolution of microstructural parameters (grain size and HAGBs fraction), microhardness and texture of 2N and 4N Ni processed by HPT to ε_{eq} = 100 and isochronal annealed [181].

Condition	Temperature (K)		d(μm)		HAGBs (%)		Hv		Texture observations	
	2N	4N	2N	4N	2N	4N	2N	4N	2N	4N
deformed	293	293	0.17	0.19	80	83	365	319	typical shear texture for high γ_{SFE}	typical shear texture for high γ_{SFE}
recovered	623	423	0.17	0.29	79	83	315	300		
recrystallized	673	433	0.4	2.6	93	94	245	185		weak and near-random
grain growth	873	673	5.9	3.5	90	95	123	95		

Table 8. Position of ideal shear texture components for BCC materials projected in SD-RD, SD-CD and CD-RD planes.

Notation	SD-RD plane		SD-CD plane		CD-RD plane	
	Miller indice {hkl}<uvw>	Euler angles (°) (φ_1, Φ, φ_2)	Miller indice {hkl}<uvw>	Euler angles (°) (φ_1, Φ, φ_2)	Miller indice {hkl}<uvw>	Euler angles (°) (φ_1, Φ, φ_2)
$\boldsymbol{D_1}$	$\{\bar{1}\bar{1}2\}\langle 111\rangle$	(90, 35.2, 45)	$\{011\}\langle 1\bar{1}1\rangle$	(54.7, 45, 0)	$\{111\}\langle 1\bar{2}1\rangle$	(30, 54.7, 45)
$\boldsymbol{D_2}$	$\{11\bar{2}\}\langle 111\rangle$	(39.2, 65.9, 26.5)	$\{101\}\langle\bar{1}11\rangle$	(125.2, 45, 90)	$\{111\}\langle\bar{1}\bar{1}2\rangle$	(90, 54.7, 45)
J	$\{\bar{1}\bar{1}0\}\langle 112\rangle$	(54.7, 90, 45)	$\{111\}\langle\bar{1}\bar{1}2\rangle$	(90, 54.7, 45)	$\{111\}\langle 1\bar{1}0\rangle$	(129.23, 65.9, 26.5)
$\bar{\boldsymbol{J}}$	$\{0\bar{1}1\}\langle\bar{2}11\rangle$	(35.2, 45, 0)	$\{111\}\langle 1\bar{2}1\rangle$	(30, 54.7, 45)	$\{111\}\langle 0\bar{1}1\rangle$	(50.7, 65.9, 63.4)
E	$\{110\}\langle 1\bar{1}1\rangle$	(35.2, 90, 45)	$\{112\}\langle\bar{1}\bar{1}1\rangle$	(90, 35.2, 45)	$\{121\}\langle\bar{1}01\rangle$	(120, 54.7, 45)
$\bar{\boldsymbol{E}}$	$\{1\bar{1}0\}\langle\bar{1}1\bar{1}\rangle$	(54.7, 45, 0)	$\{111\}\langle 0\bar{1}1\rangle$	(39.2, 65.9, 26.5)	$\{211\}\langle 0\bar{1}1\rangle$	(60, 54.7, 45)
F	$\{110\}\langle 001\rangle$	(0, 45, 0)	$\{011\}\langle 100\rangle$	(0, 45, 0)	$\{001\}\langle 1\bar{1}0\rangle$	(45, 0, 0)

Table 9. Position of ideal shear texture components for HCP materials and alloys projected in the SD-RD, SD-CD and CD-RD planes.

Notation	**SD-RD plane**	**SD-CD plane**	**CD-RD plane**
	Euler angles (°)	Euler angles (°)	Euler angles (°)
	(φ_1, Φ, φ_2)	(φ_1, Φ, φ_2)	(φ_1, Φ, φ_2)
B-fiber	(0-60, 0, 0)	(0, 90, 0-60)	(360, 90, 0-60)
P-fiber	(180, 0-90, 30)	(0, 0-90, 30)	(90-180, 90, 0)
Y-fiber	(180, 60, 0-60)	(0, 30, 0-60)	(300, 90, 0-60)
C_1-fiber	(90, 60, 0-60)	(60, 90, 0-60)	(0, 30, 0-60)
C_2-fiber	(270, 60, 0-60)	(120, 90, 0-60)	(180, 30, 0-60)

Table 10. Evolution of the texture in the center of some HCP-processed alloys as a function of numbers of HPT turns

Alloy	Experimental conditions	Initial texture	Major texture observations	Ref.
Pure Zn	P= 1 GPa, V = 1 rpm, RT N = 1, 3 and 5 turns XRD at the center of the discs	Extrusion texture <$10\bar{1}0$>//ED	Formation of typical *B*-fiber after N =1 turn. The texture strength with increasing number of HPT turns.	[203]
Pure Mg	P= 6 GPa, V = 1 rpm, RT N = 1/8, 1/4, 1/2, 1, 2,4, 8 and 16 turns Neutron diffraction at center of the discs	Near-random and extrusion texture	Initial near-random texture Formation of typical *B*-fiber after N =1 turn. The texture saturated with increasing number of HPT turns. Initial extrusion texture Formation of typical B-fiber after N =1/8 turn. The texture saturated with increasing number of HPT turns.	[67]
Pure Mg	P= 6 GPa, V = 1 rpm, RT N = 1 and 5 turns EBSD at center of the discs	Near-random texture	Formation of typical *B*-fiber after N =1 turn. The texture saturated with increasing number of HPT turns.	[202]
Mg-1.44Ce	P= 6 GPa, V = 1 rpm, RT N = 1/2, 1, 5 and 10 turns	Near-random texture	Formation of asymmetric *B*-fiber after N = ½ turn. The texture saturated with increasing number of HPT turns.	[204]

	XRD at center of the discs			
Mg-1.43Nd	P= 6 GPa, V = 1 rpm, RT N = 1/2, 1, 5 and 10 turns XRD at center of the discs	Near-random texture	Formation of asymmetric *B*-fiber after N = ½ turn. The texture is weaker with increasing number of HPT turns.	[204]
Mg-0.41Dy	P= 6 GPa, V = 1 rpm, RT N = 1/2, 1, 5 and 10 turns XRD at center of the discs	Near-random texture	Formation of typical B-fiber after N =1 turn. The texture saturated with increasing number of HPT turns.	[68]
AM60	P= 6 GPa, V = 1 rpm, RT N = 1/2, 1, 3 and 10 turns EBSD at center of the discs	Extrusion texture <$10\bar{1}0$>//ED	Formation of typical *B*-fiber after N =1 turn and despaired after N = 10 turns.	[215]

Table 11. Different combinations and methods for texture simulation used by Li et al. [233]. Reproduced with permission.

Designation	Polycrystal model	Grain co-rotation (GCR)	Grain subdivision (GSD)	Deformation model
FC/SS	FC Taylor	-	-	SS
FC/FE	FC Taylor	-	-	FE
SC/SS	VPSC	Off	Off	SS
SCD/SS	VPSC	Off	On	SS
SCR/SS	VPSC	On	Off	SS
SCRD/SS	VPSC	On	On	SS
SCRD/FE	VPSC	On	On	FE

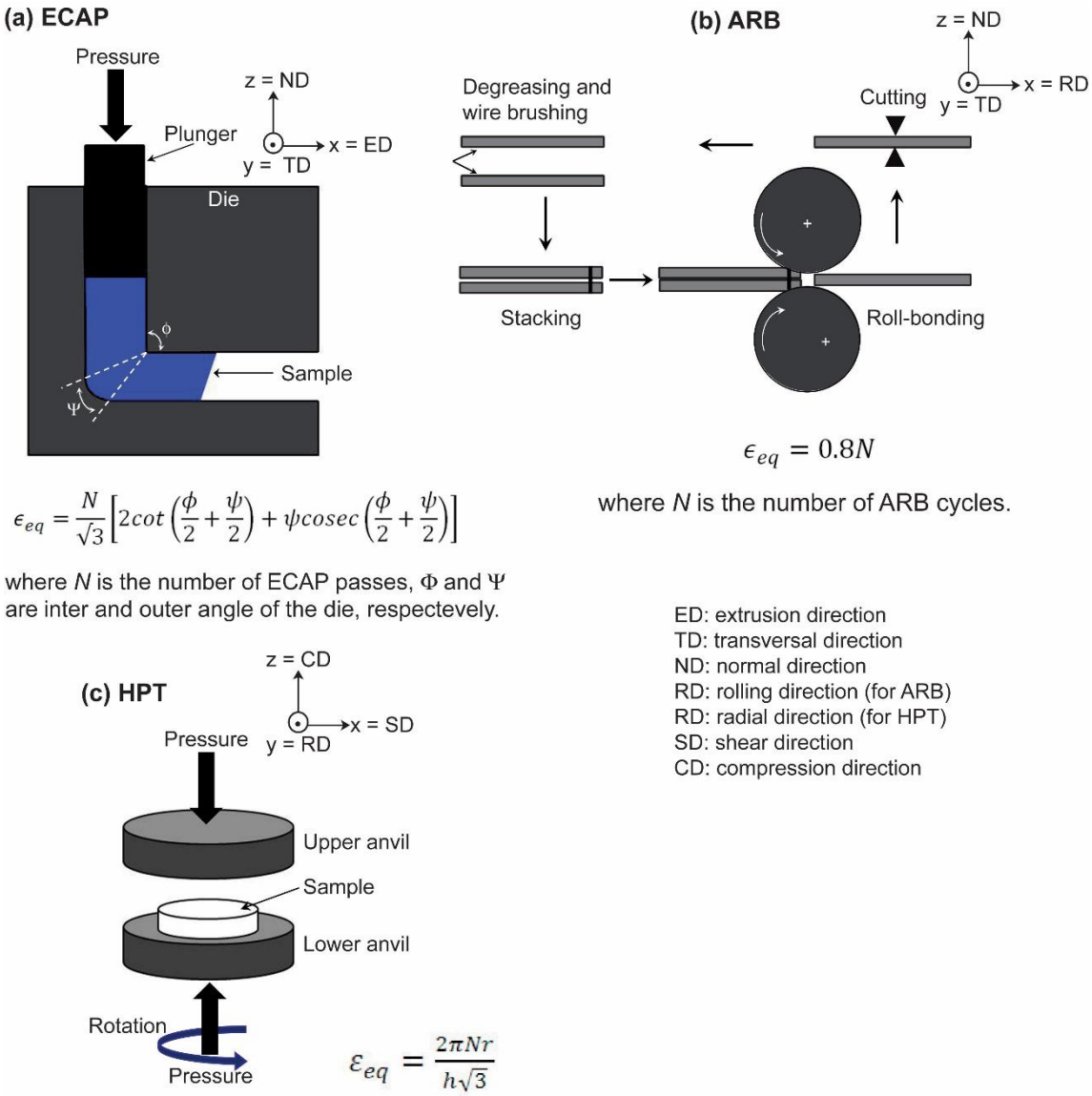

$$\epsilon_{eq} = \frac{N}{\sqrt{3}}\left[2cot\left(\frac{\phi}{2}+\frac{\psi}{2}\right)+\psi cosec\left(\frac{\phi}{2}+\frac{\psi}{2}\right)\right]$$

where *N* is the number of ECAP passes, Φ and Ψ are inter and outer angle of the die, respectevely.

$$\epsilon_{eq} = 0.8N$$

where *N* is the number of ARB cycles.

$$\varepsilon_{eq} = \frac{2\pi Nr}{h\sqrt{3}}$$

where *N* is the number of HPT turns, *r* the disc radius and *h* the disc thickness.

ED: extrusion direction
TD: transversal direction
ND: normal direction
RD: rolling direction (for ARB)
RD: radial direction (for HPT)
SD: shear direction
CD: compression direction

Figure 1: Illustrations showing the principles of ECAP, ARB and HPT processing.

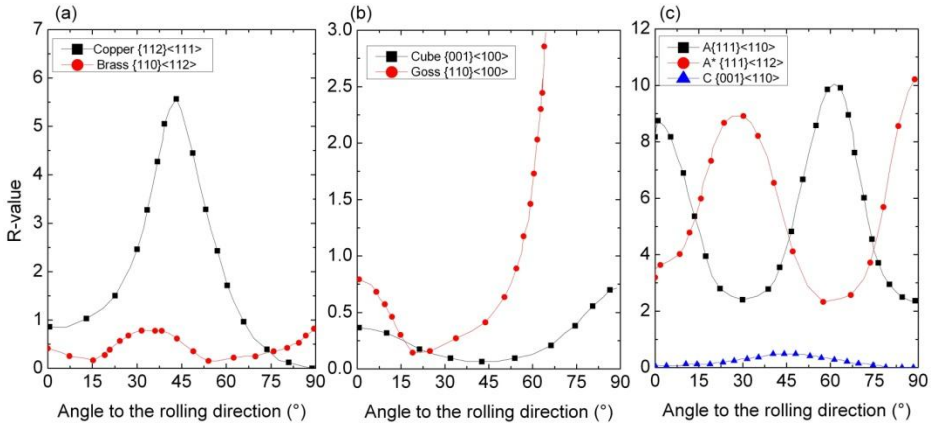

Figure 2: Effect of different texture component on the R-value as a function of orientation with respect to the rolling direction of the sheet: a) Copper {112}<111> and Brass {110}<112> (deformation components, b) Cube {001}<100> and Goss {110}<100> (recrystallization components) and c) A{111}<110>, A* {111}<112> and C {001}<110> (shear components) [88].

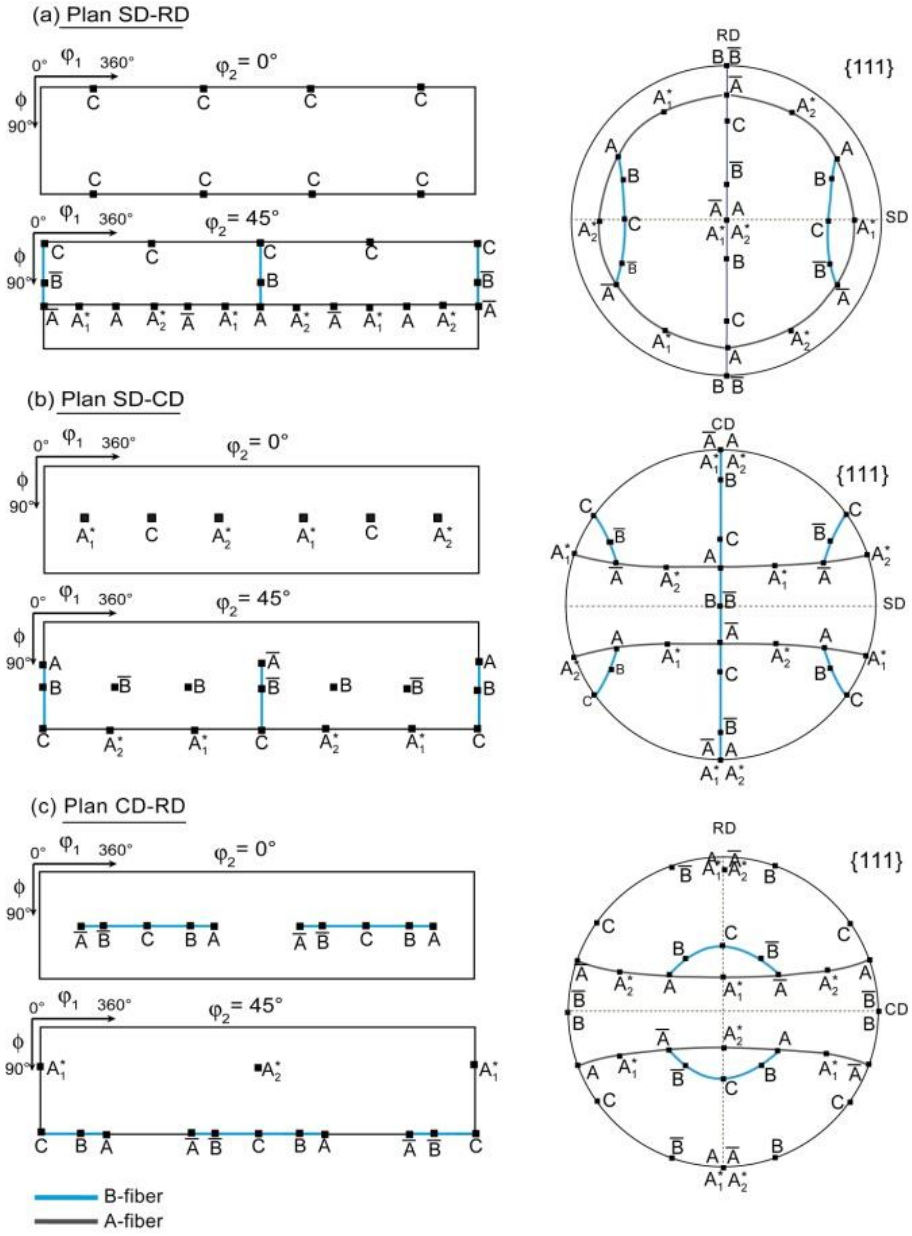

Figure 3: ODF sections at φ_2 = 0 and 45 ° and {111} pole figures showing the positions of the ideal shear texture components on the SD-RD, SD-CD and CD-RD planes for materials with FCC structure.

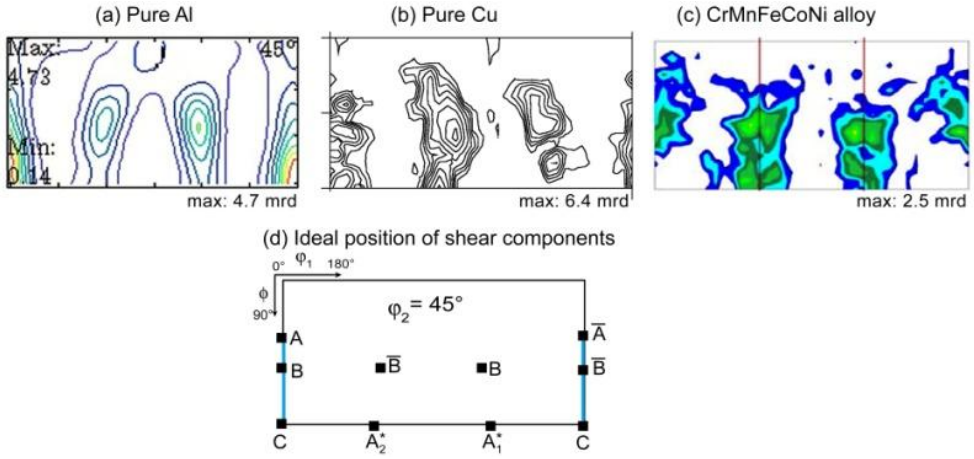

Figure 4: ODF sections at φ_2 = 45° showing the texture difference between HPT-processed (a) pure Al for ε_{eq} = 7.97 (measured by EBSD) [116], (b) pure Cu for ε_{eq} = 254 (measured by XRD) [127], (c) CrMnFeCoNi alloy for ε_{eq} = 9.23 (measured by XRD) [135] and (d) ideal position of the shear texture components.

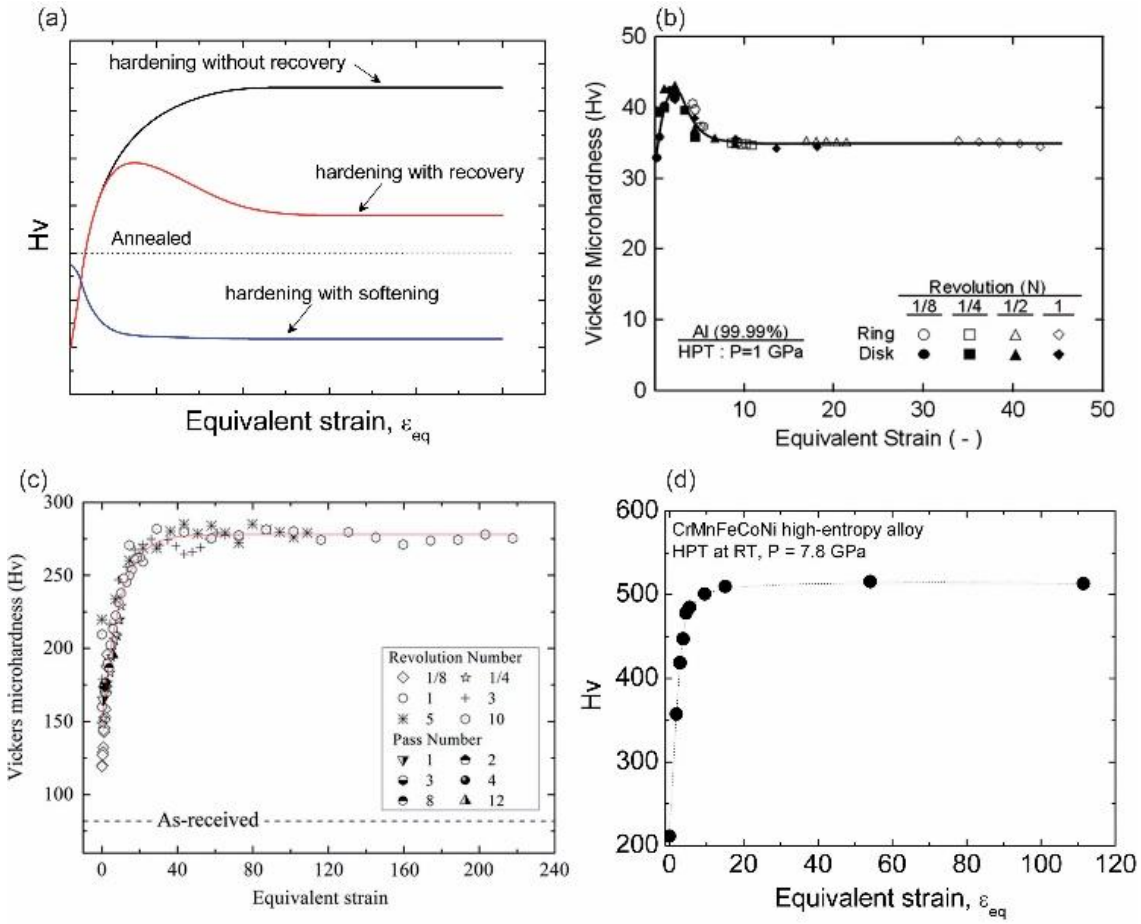

Figure 5: a) Schematic illustration of hardening models: without recovery, with recovery and softening for materials processed by HPT [146], experimental example (b) of hardening with recovery of pure Al processed by HPT [151], (c) hardening without recovery of Cu-2.5Ni-Si alloy processed by HPT and ECAP [150] and (d) CrMnFeCoNi high entropy alloy processed by HPT [149].

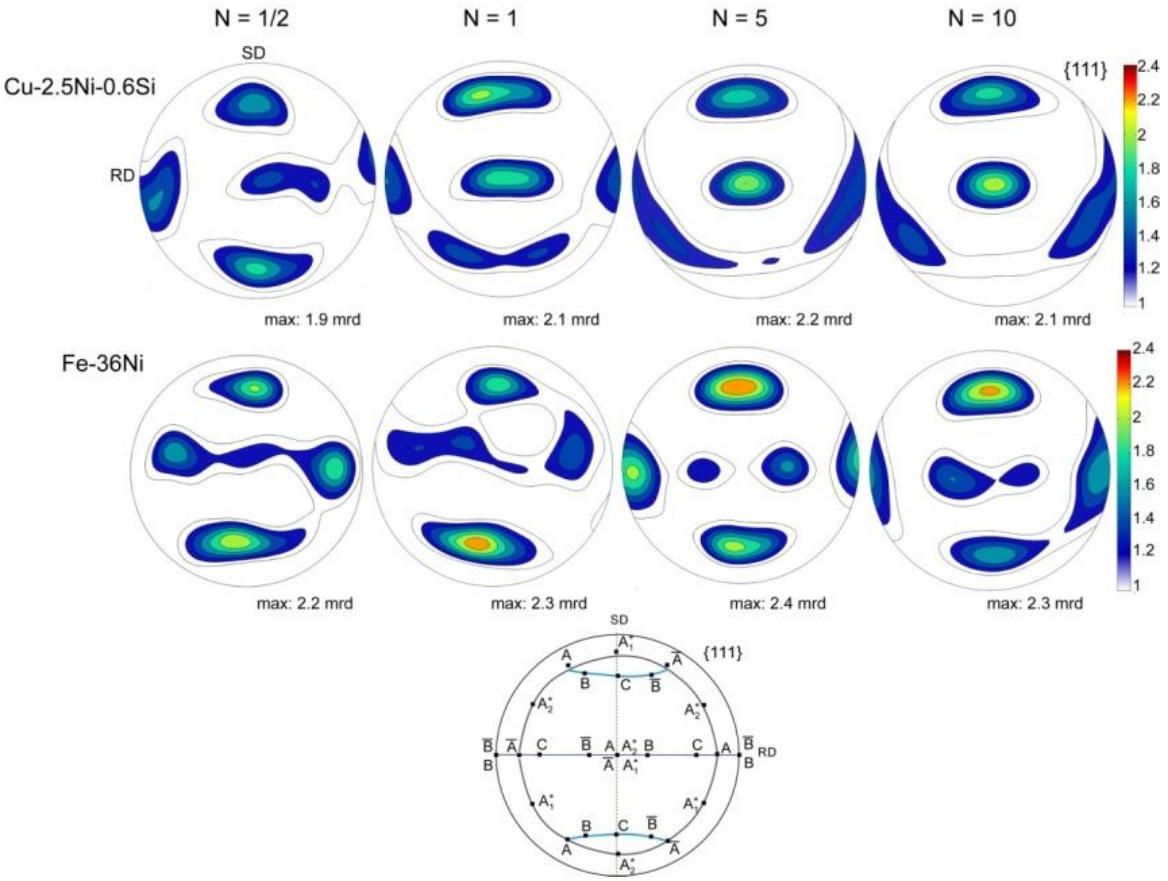

Figure 6: Recalculated {111} pole figure of Cu-2.5Ni-0.6Si and Fe-36Ni alloys after HPT proceeding at RT through N = 1/2, 1, 5 and 10 turns [157]. Pole figures were presented in equal area projection.

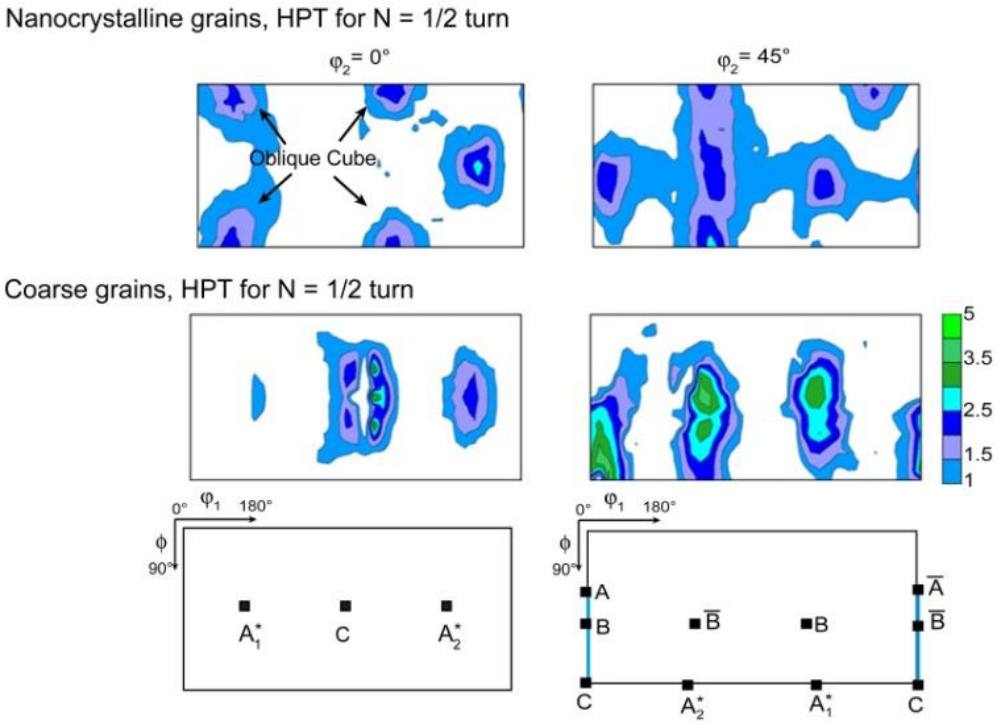

Figure 7: Texture evolution of Pd-10Au alloy after HPT processing for N = ½ turn (ε_{eq}= 7.67) with different initial grain size: based on an earlier report [133].

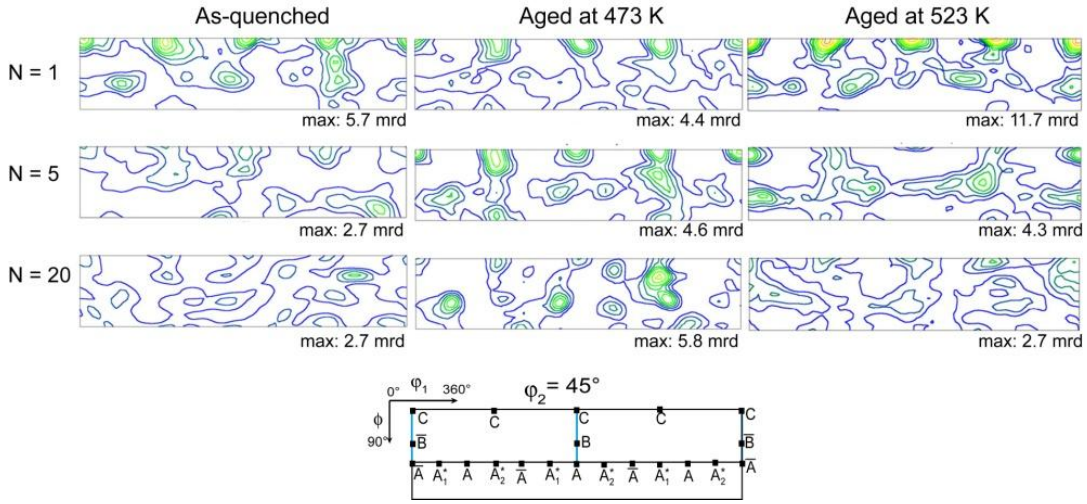

Figure 8: ODF sections at φ_2 = 45° for as-quenched, aged at 473 K and aged at 523 K Al-0.6Mg-0.4Si alloy processed by HPT for N = 1, 5 and 20 turns, respectively [119]. Reproduced with permission.

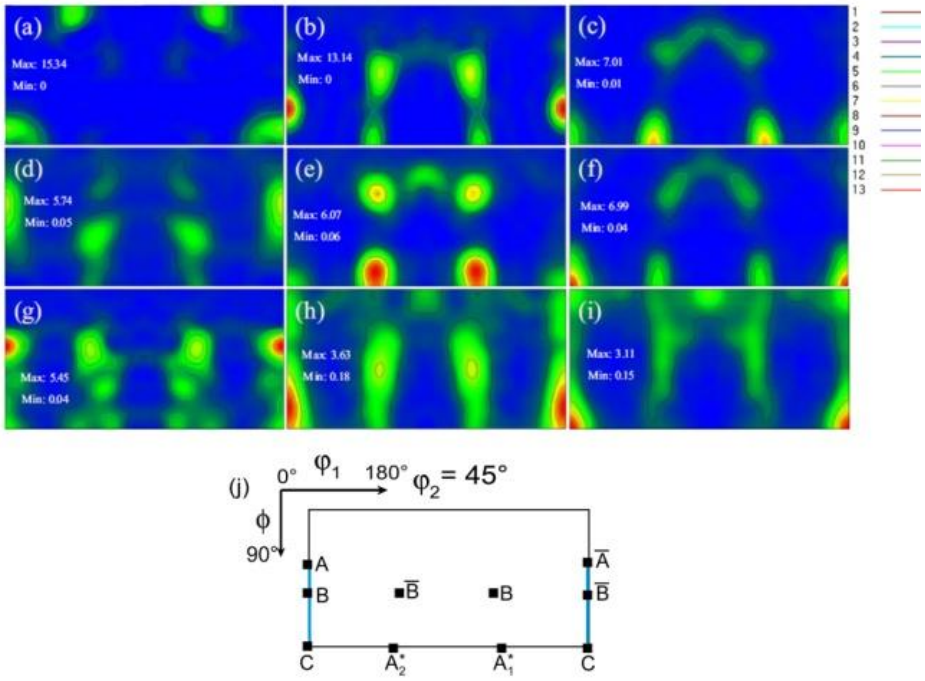

Figure 9: Instability of the texture during earlier stage of processing showing by ODF sections at $\varphi_2 = 45°$ of CP Al alloy after HPT processing at ε_{eq} of: (a) 0.45, (b) 0.90, (c) 1.34, (d) 2.69, (e) 5.38, (f) 10.76, (g) 21.51, (h) 32.27 and (i) 53.78 [117]. Reproduced with permission.

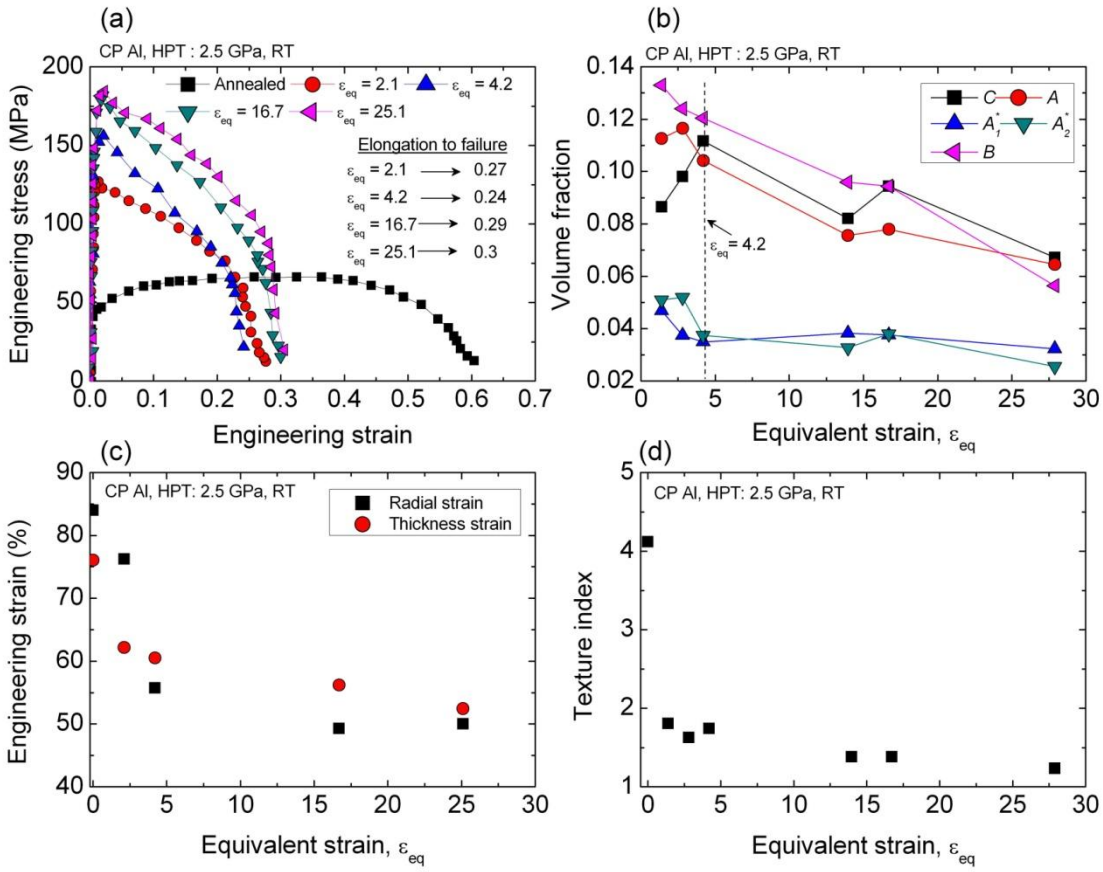

Figure 10:. (a) Engineering stress-strain curves of annealed and HPT processed CP Al, (b) evolution of (c) shear texture components (c) radial and thickness strain and (d) texture index as a function of equivalent strain [138].

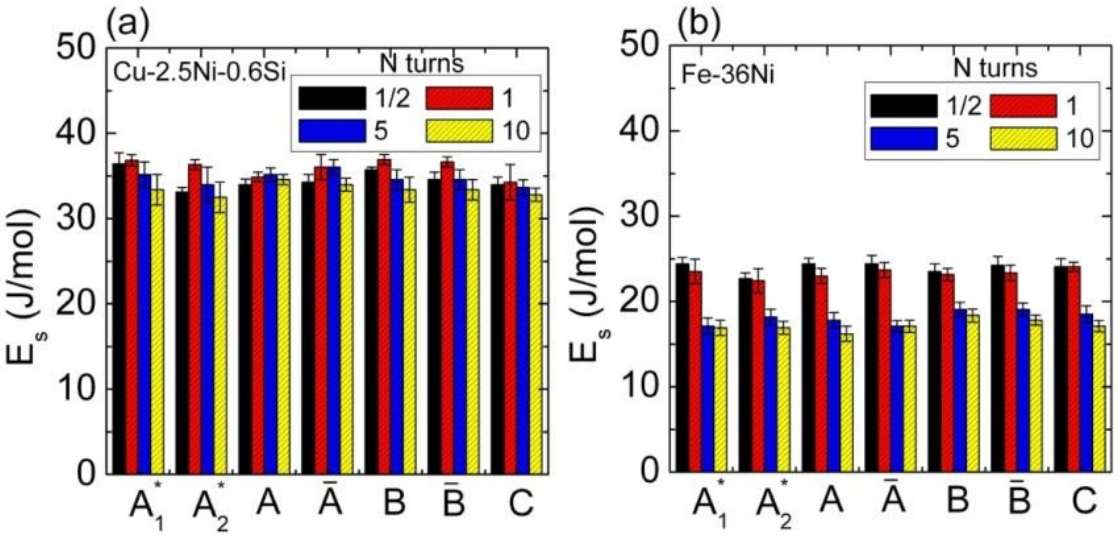

Figure 11 : Evolution of the stored energy in the shear texture components as a function of number of HPT turns of the: (a) Cu-2.5Ni-0.6Si and (b) Fe-36Ni alloy [157].

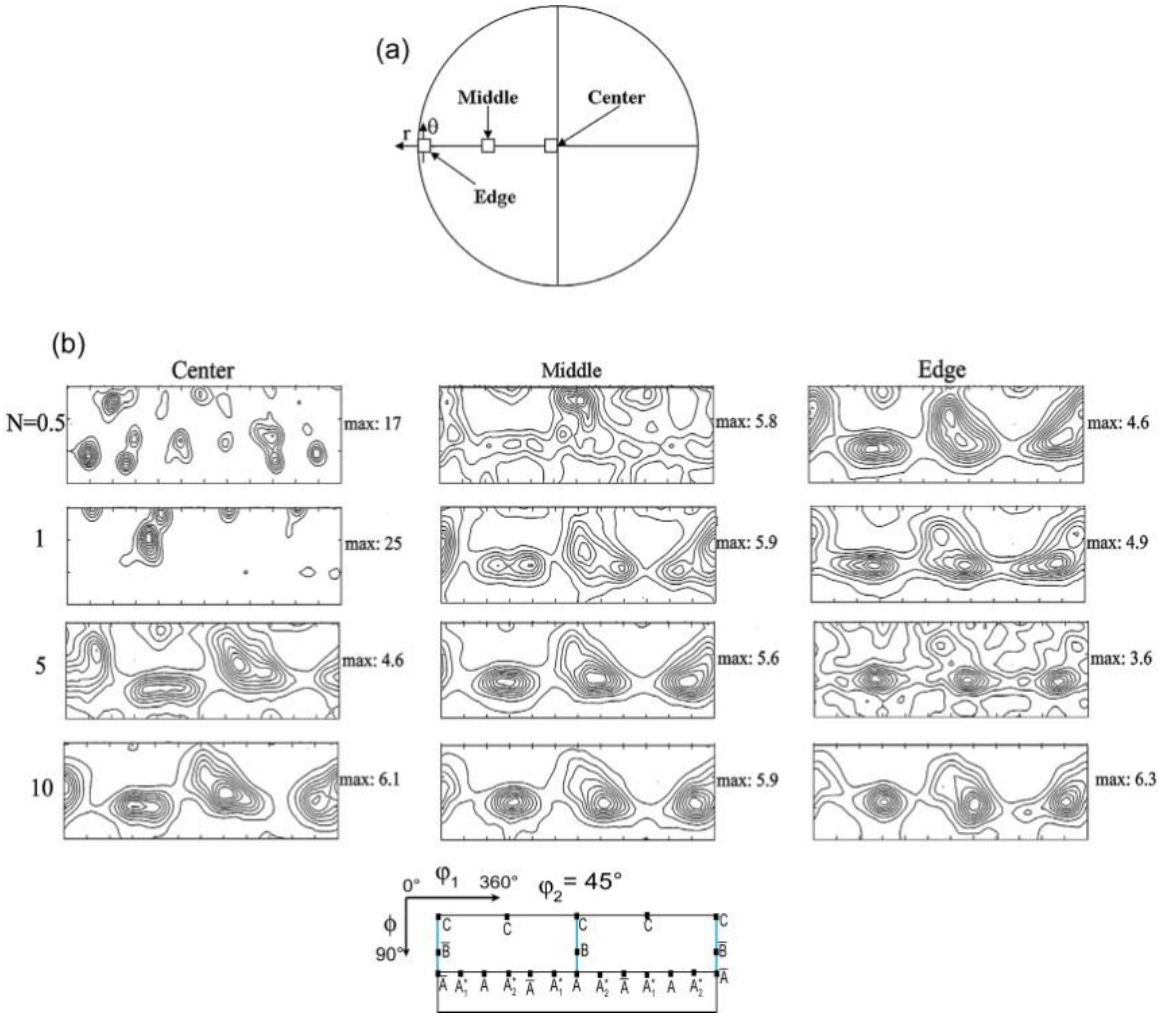

Figure 12: (a) Distribution of HPT-disc areas, where the texture measurements were performed and (b) ODF sections at φ_2 = 45° near the center, half-radius and near the edge of the disc of Cu-2.5Ni-0.6Si alloy after processing by HPT through 1/2, 1, 5 and 10 turns [72]. Reproduced with permission.

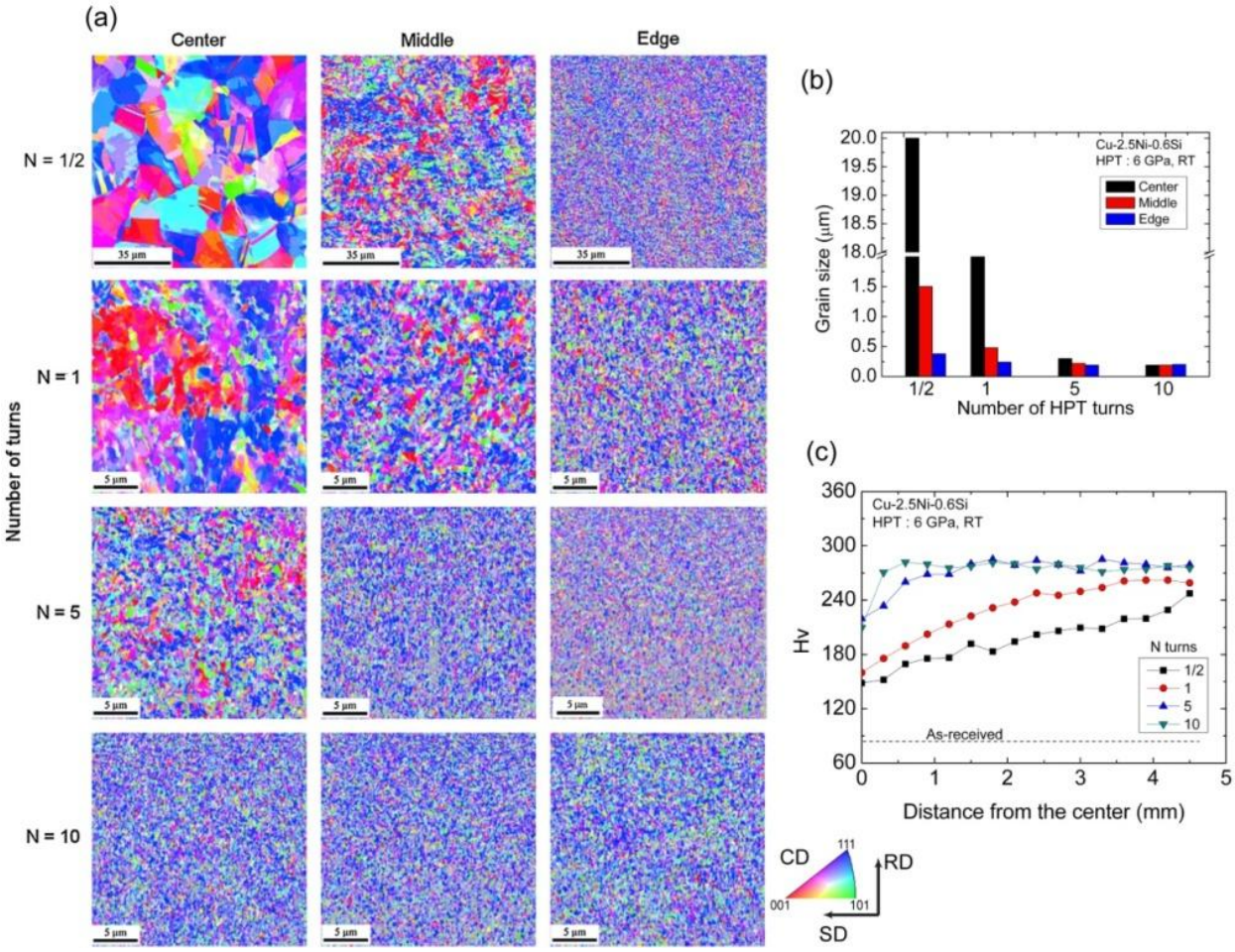

Figure 13: (a, b) evolution of the microstructure and mean grain size of Cu-2.5Ni-0.6Si alloy after HPT at the center, middle and near edge after processing through 1/2, 1, 5 and 10 turns [72] and (c) evolution of Vickers microhardness with distance from the center of the HPT processed discs [150].

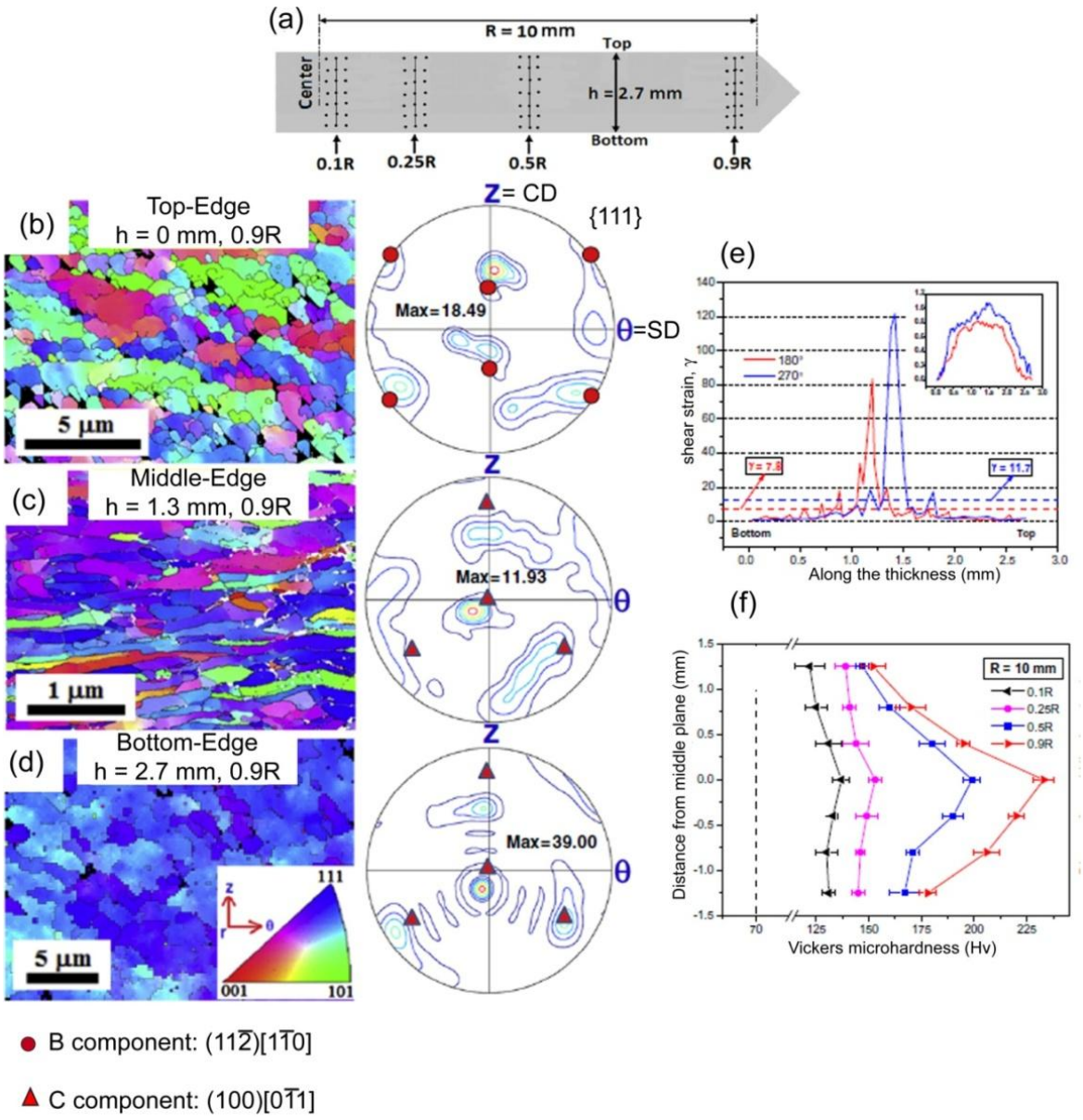

Figure 14: (a) Schematic illustration of cross-sectional plane of one-half of an HPT-disc showing the positions selected for Vickers microhardness and EBSD measurements. EBSD orientation maps and the corresponding {111} pole figures measured at the edge of the disc: (b) top, (c) middle and (d) bottom sections. (e) Strain distribution across the through-thickness and (f) distributions of Vickers microhardness in the radial direction across the through-thickness in Al (A5086) alloy processed at RT for 270° rotation (N = 3/4 turn) [175]. Reproduced with permission.

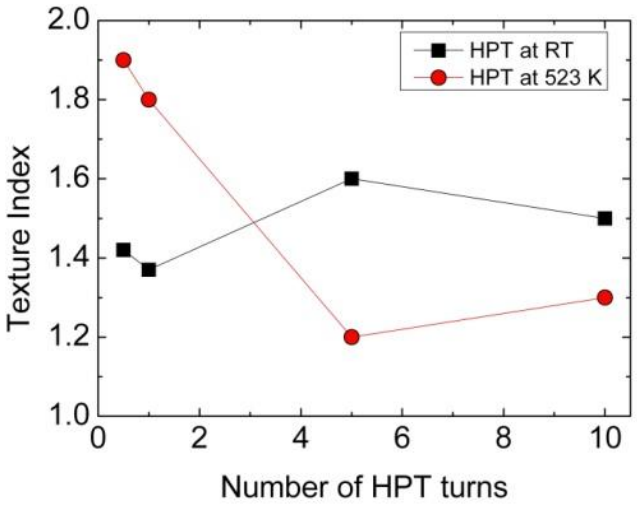

Figure 15: Evolution of the texture index value of Fe-36Ni alloy after HPT processing up 10 turns at RT and 523 K [54] . Reproduced with permission.

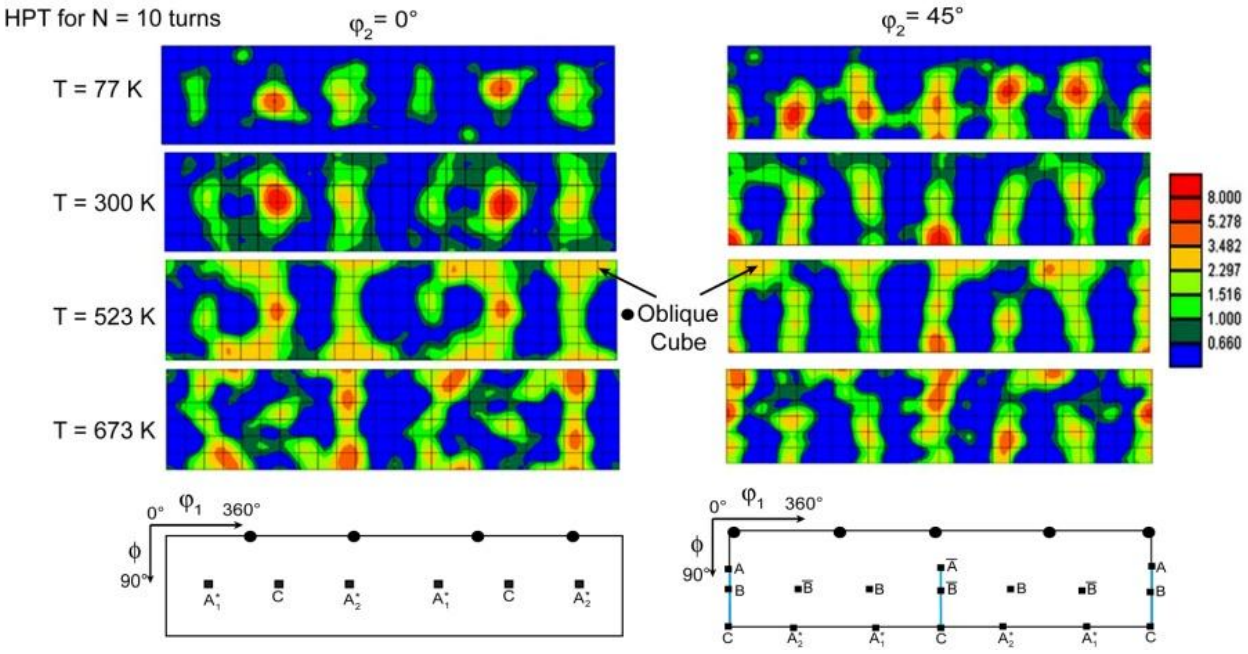

Figure 16: ODF sections at φ_2 = 0 and 45° of HPT processed pure Ni at 77, 300, 523 and 673 K, respectively [124]. Ideal positions of the shear texture components and Oblique Cube are also presented. Reproduced with permission.

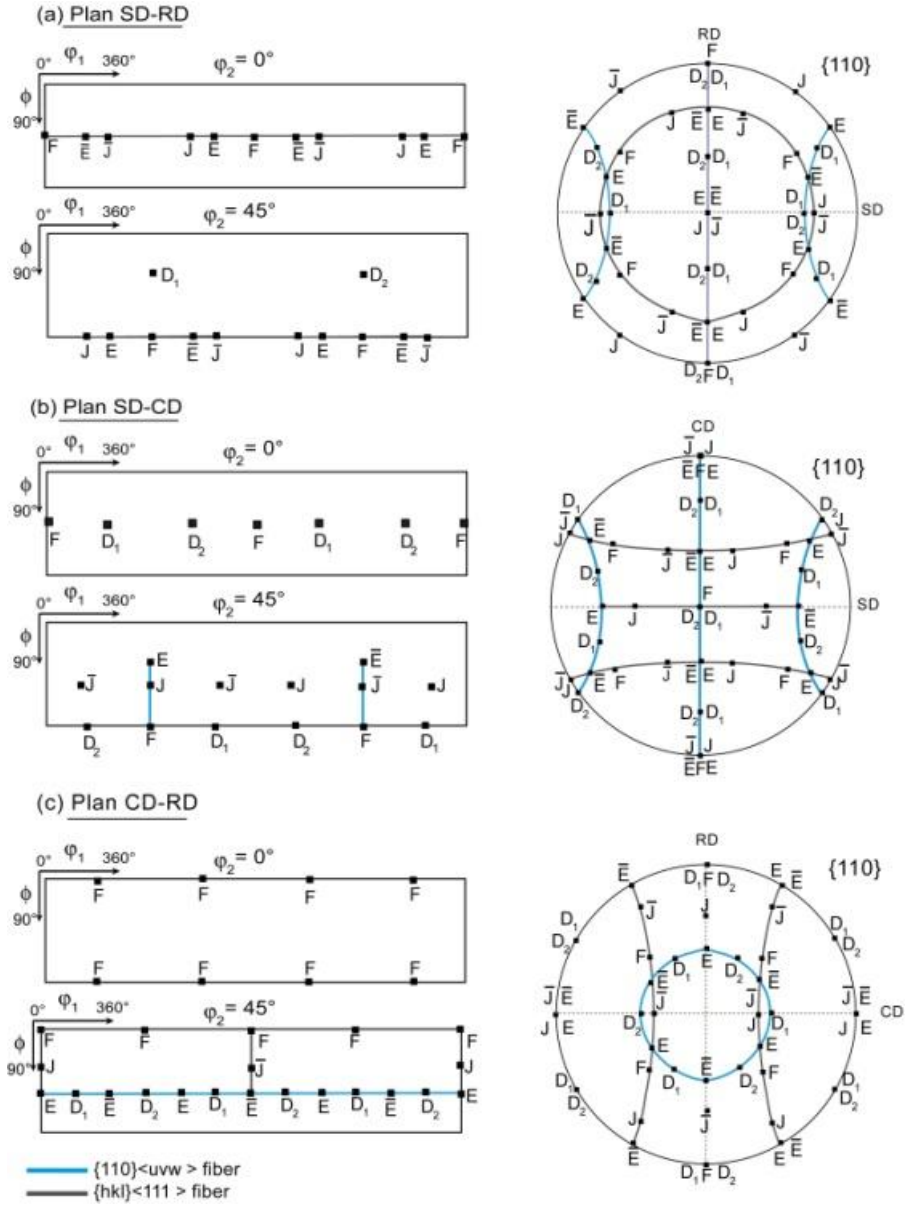

Figure 17: ODF sections at φ_2 = 0 and 45 ° and {110} pole figures showing the position of ideal shear texture components on the SD-RD, SD-CD, CD-RD planes for materials with BCC structure.

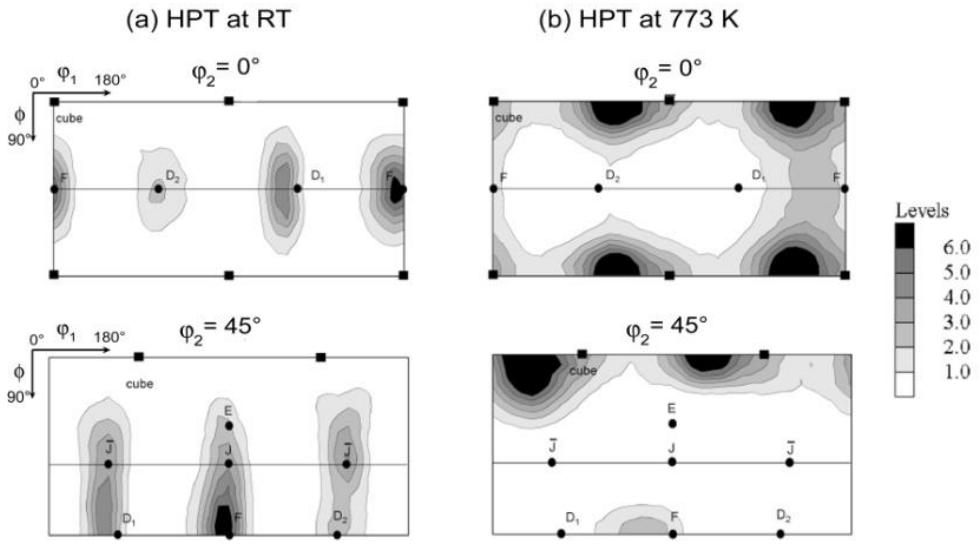

Figure 18: ODF sections at φ_2 = 0 and 45° of NiAl intermetallic processed by HPT to $\varepsilon_{eq} \approx 34.6$ at: (a) RT and (b) 773 K [188].

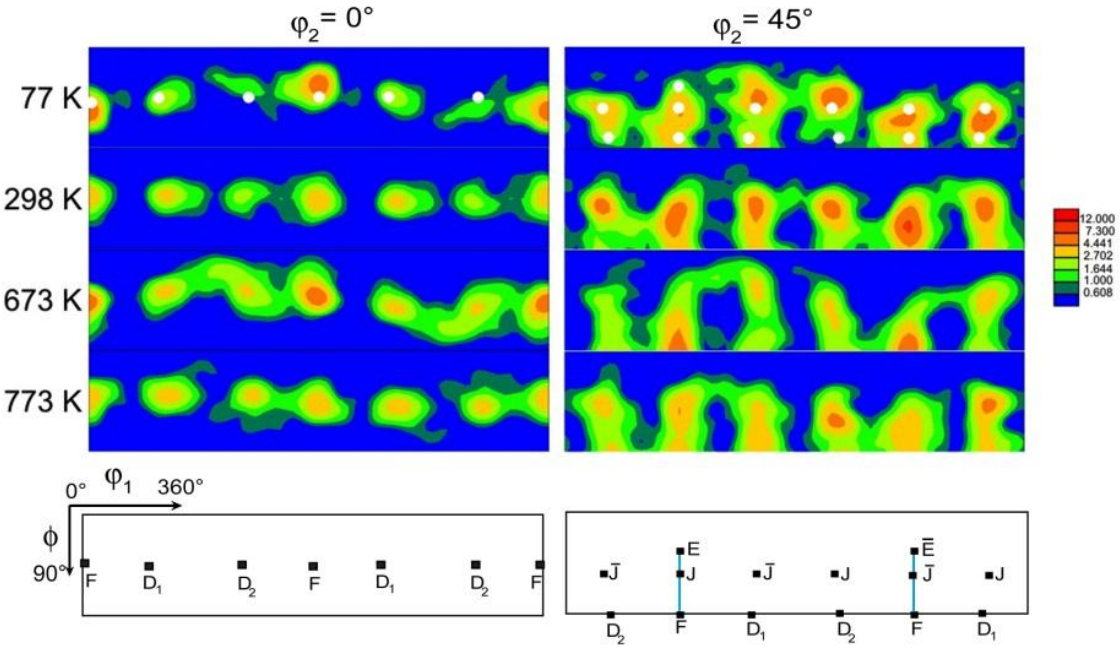

Figure 19: ODF sections at φ_2 = 0 and 45° for pure tantalum HPT processed (ε_{eq} = 136) for different temperatures [191]. Reproduced with permission.

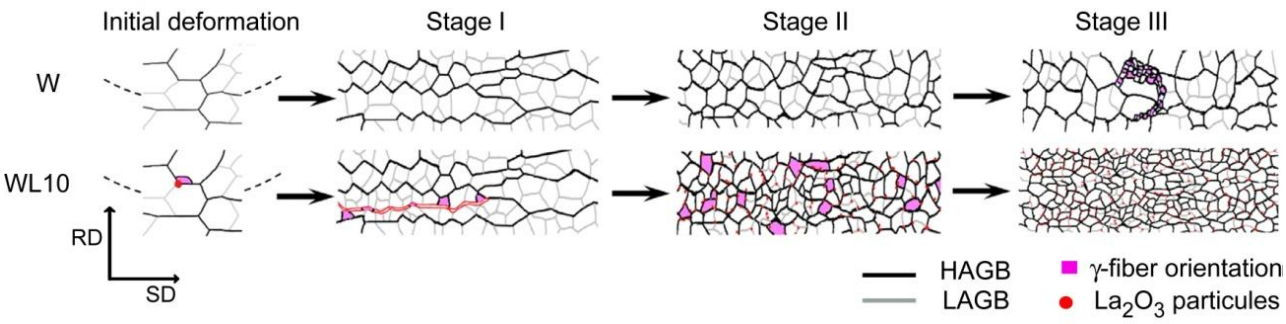

Figure 20: A schema illustrates the evolution of the microstructure and texture in W and WL10 alloys during HPT processing [186].

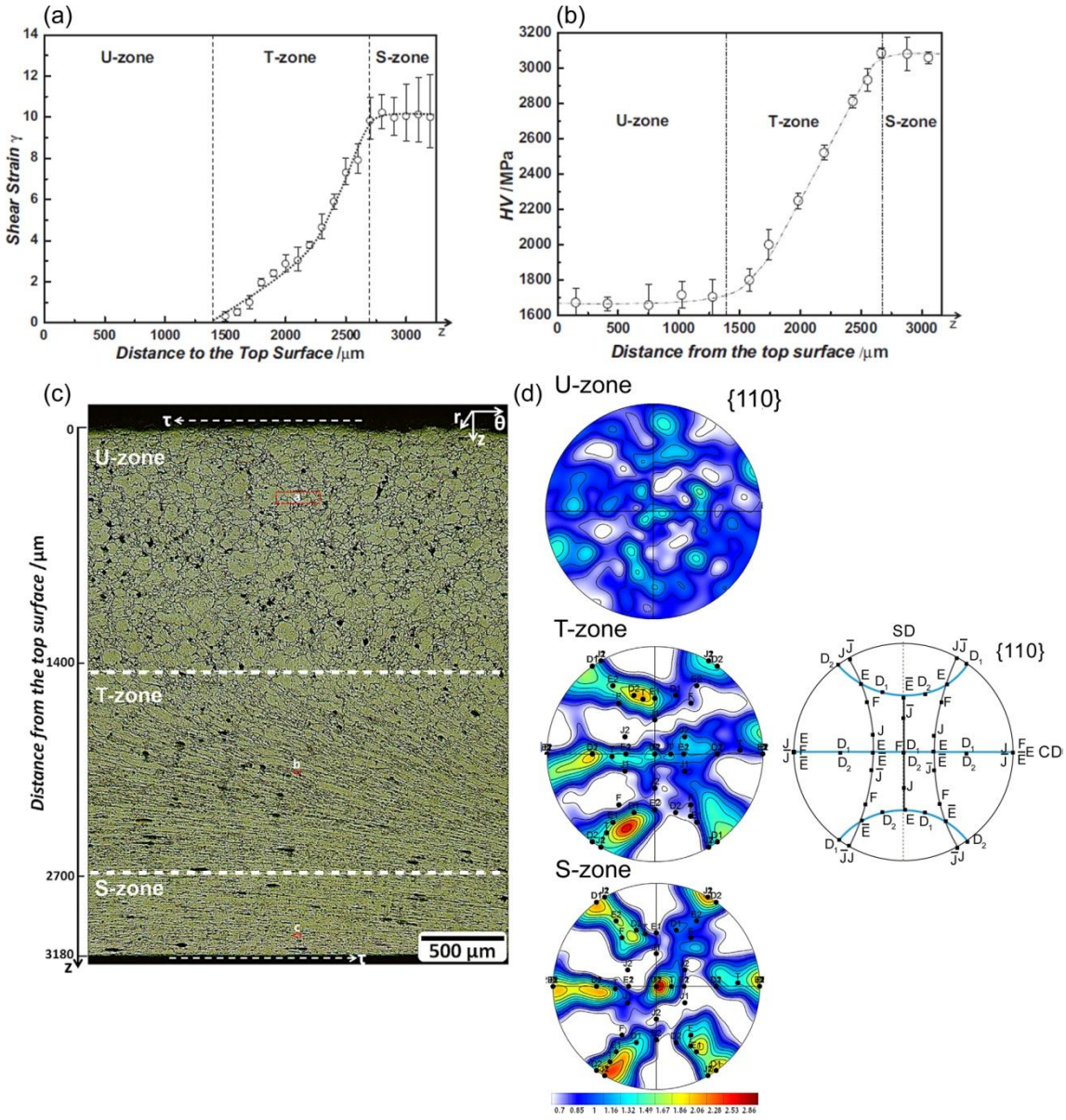

Figure 21: Variation of (a) shear strain, (b) microhardness, (c) Optical micrograph, across the thickness of the HPT Fe consolidated disc and (d) the corresponding {110} pole figure in the three distinct deformation zones: U, T and S-zones [183]. Pole figures were presented in stereographic projection Reproduced with permission.

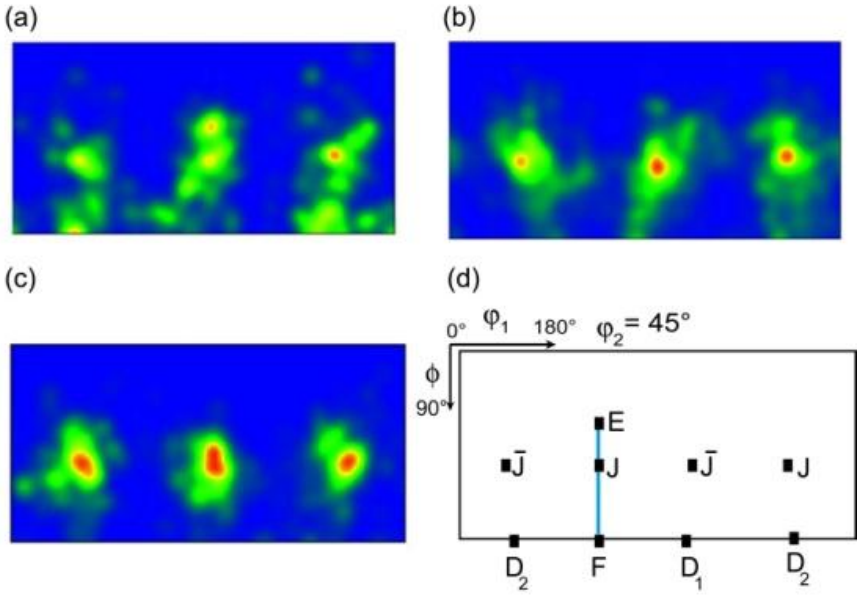

Figure 22: φ_2 = 45° ODF sections of Fe-9Cr alloy: (a) processed by HPT at 573 K for N = 10 turns, followed by annealing at 873 K for (b) 6 h and (c) 24 h. (d) represents the key figure of ideal shear components of BCC materials [184]. Reproduced with permission.

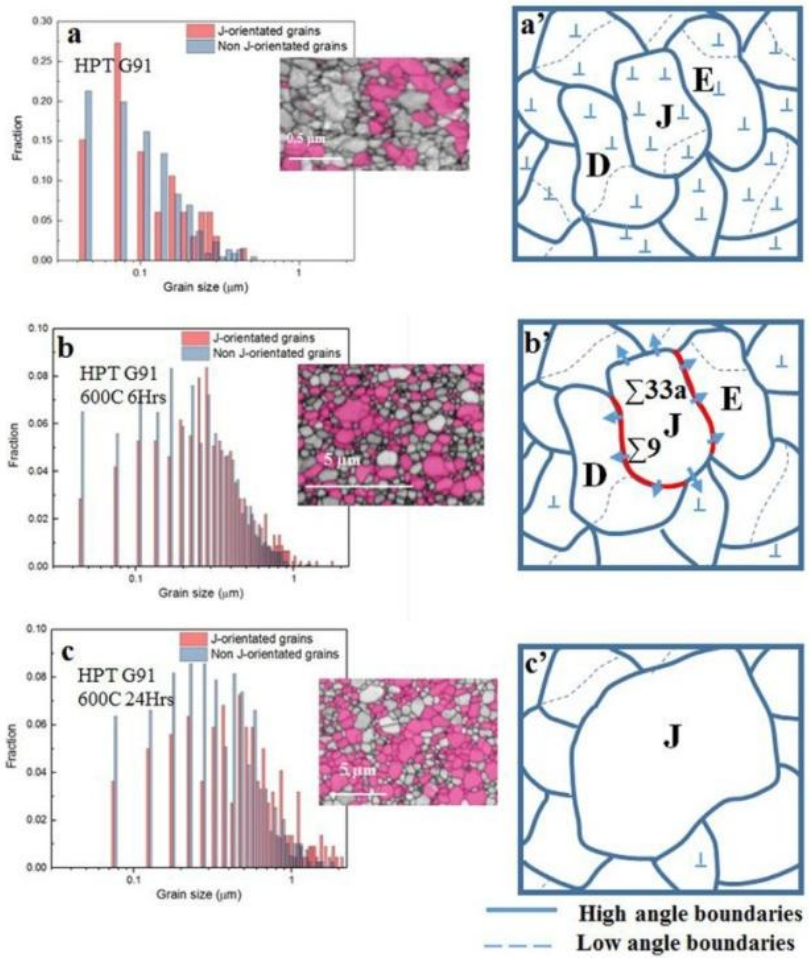

Figure 23: (a-c) grain size distribution of Fe-9Cr alloy after HPT processing at 573 K for N = 10 turns and subsequent annealing at 873 °C for 6 and 24 h. EBSD maps showing grains with *J* orientation (highlighted in red color) having the larger average size, (a'- c') schematic illustrations of the changes in microstructure and texture in HPT-processed Fe-9Cr alloy during annealing [184].

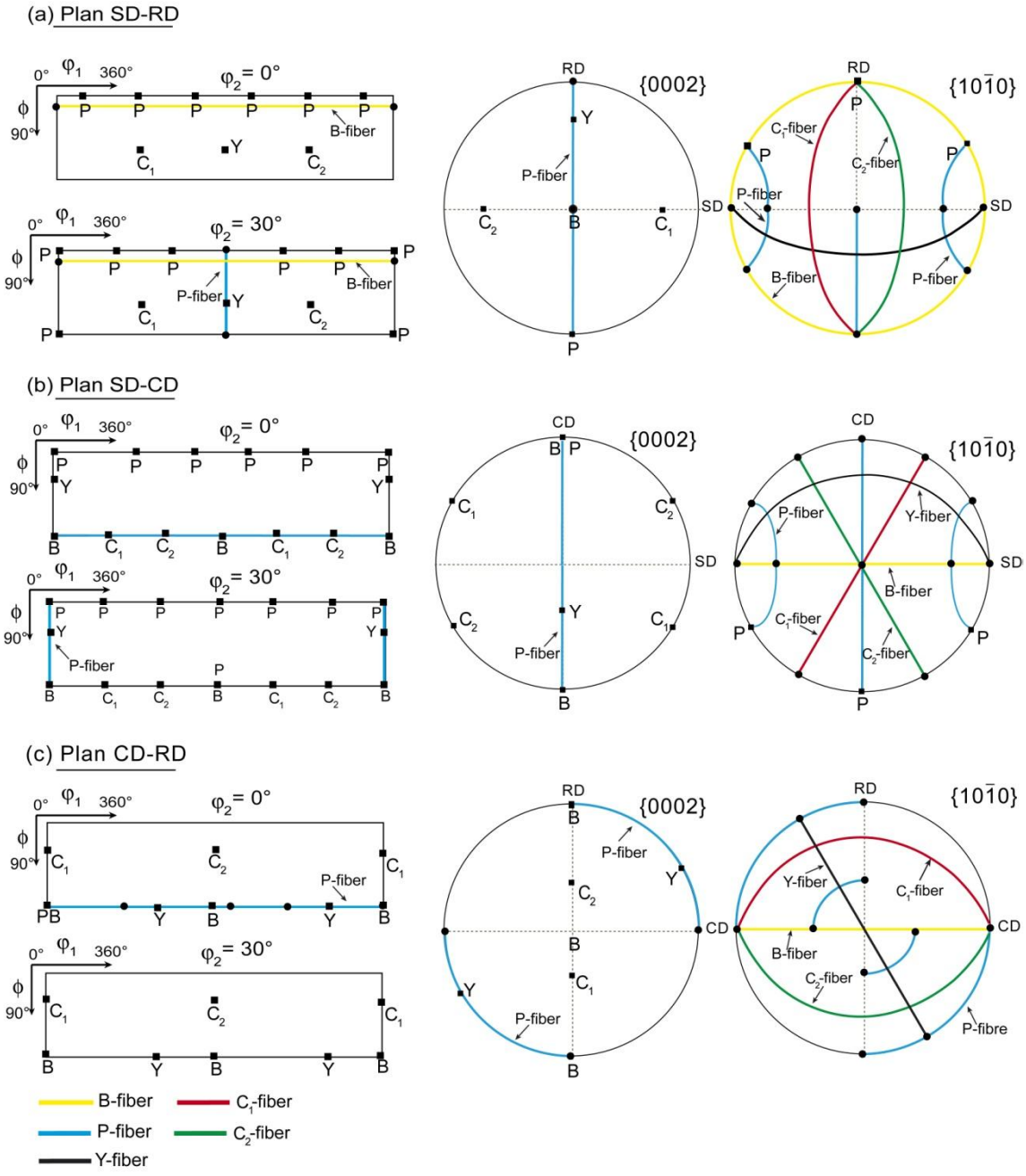

Figure 24: ODF sections at φ_2 = 0 and 30 ° and {0002} and {10$\bar{1}$0} pole figures showing the position of ideal shear texture components on SD-RD, SD-CD, CD-RD planes for materials with HCP structure.

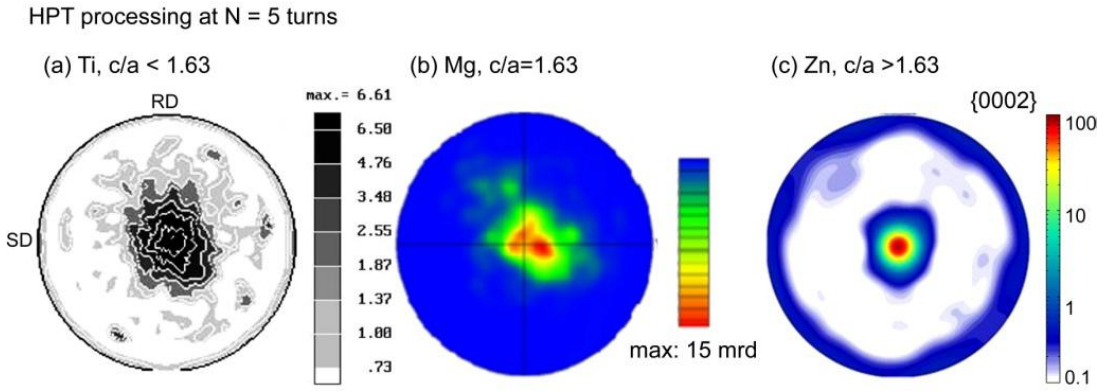

Figure 25: {0002} pole figure of pure : (a) Ti [201], (b) Mg [202] and (c) Zn [203] after HPT processing at RT through N = 5 turns. Reproduced with permission for Zn.

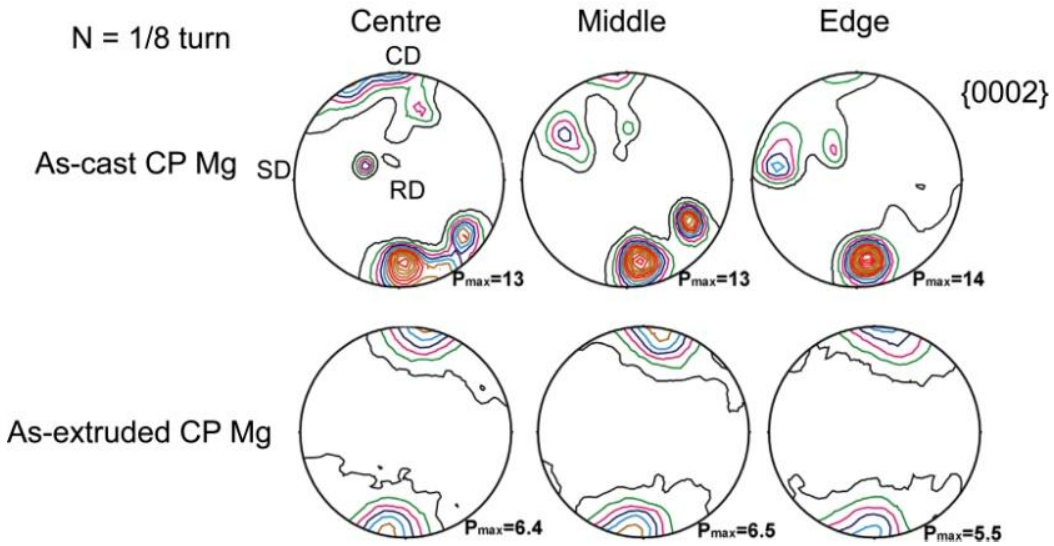

Figure 26: Texture difference presented by the {0002} recalculated pole figures between the as-cast and as-extruded CP Mg after HPT processing at N = 1/8 turn [67]. Reproduced with permission.

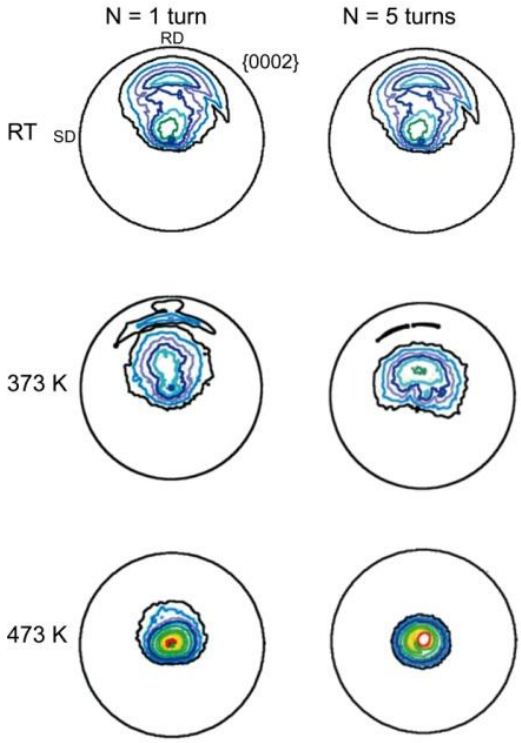

Figure 27: {0002} recalculated pole figures of AZ31 alloy processed by HPT for N = 1 and 5 turns at RT, 373 and 473 K, respectively [211].

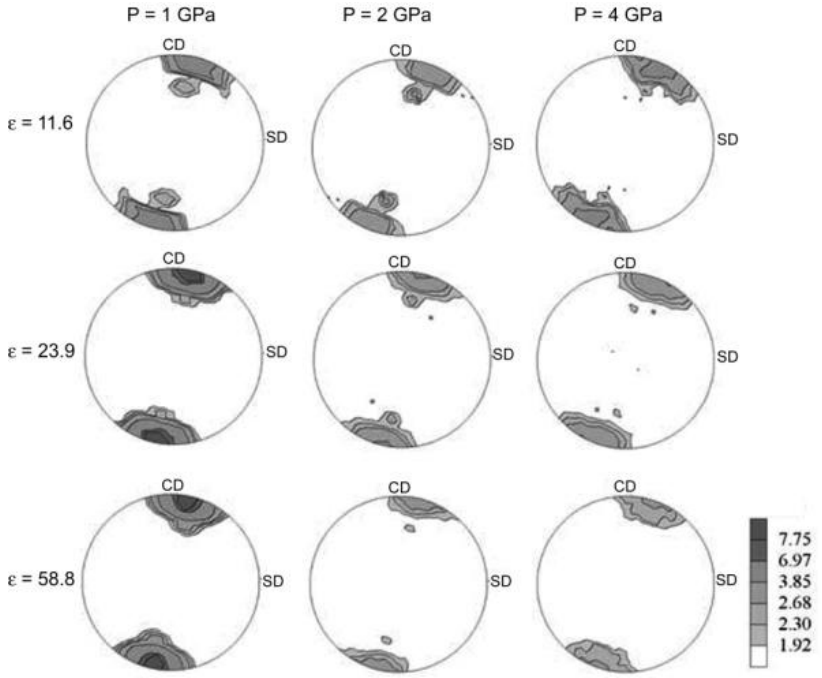

Figure 28: {0002} pole figure evolution in pure Mg as a function of the hydrostatic pressure and shear strain imposed during HPT processing: modified from [213].

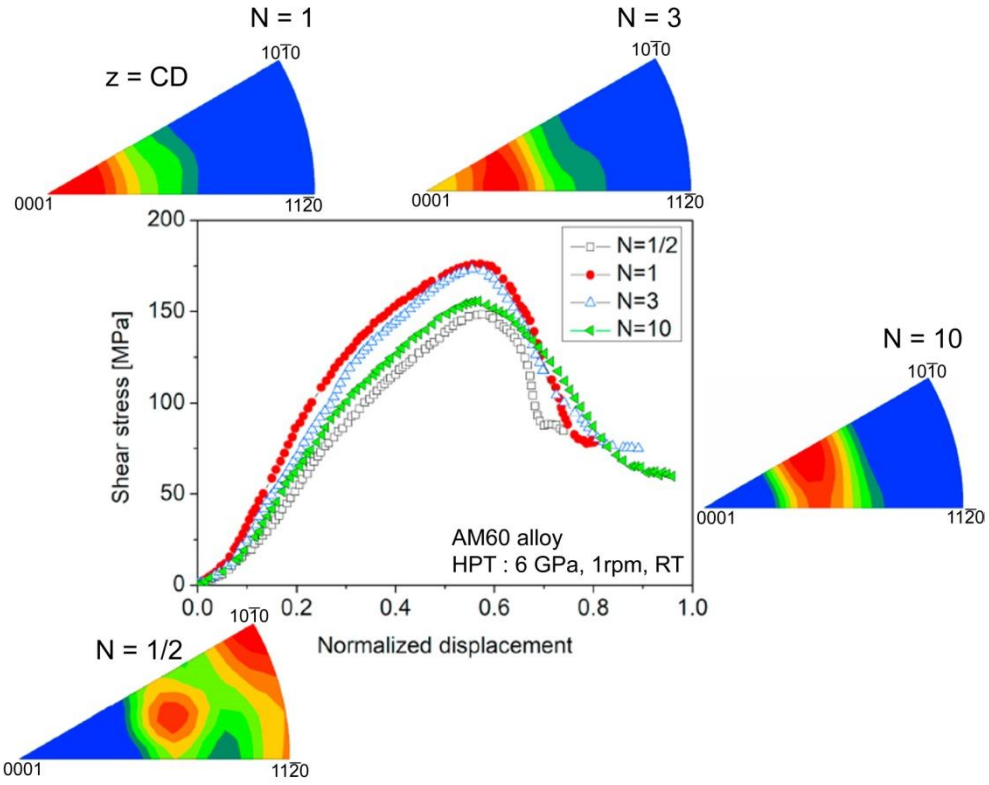

Figure 29: Strain-stress curves and the corresponding texture evolution of AM60 alloy as a function of number of HPT turns [215].

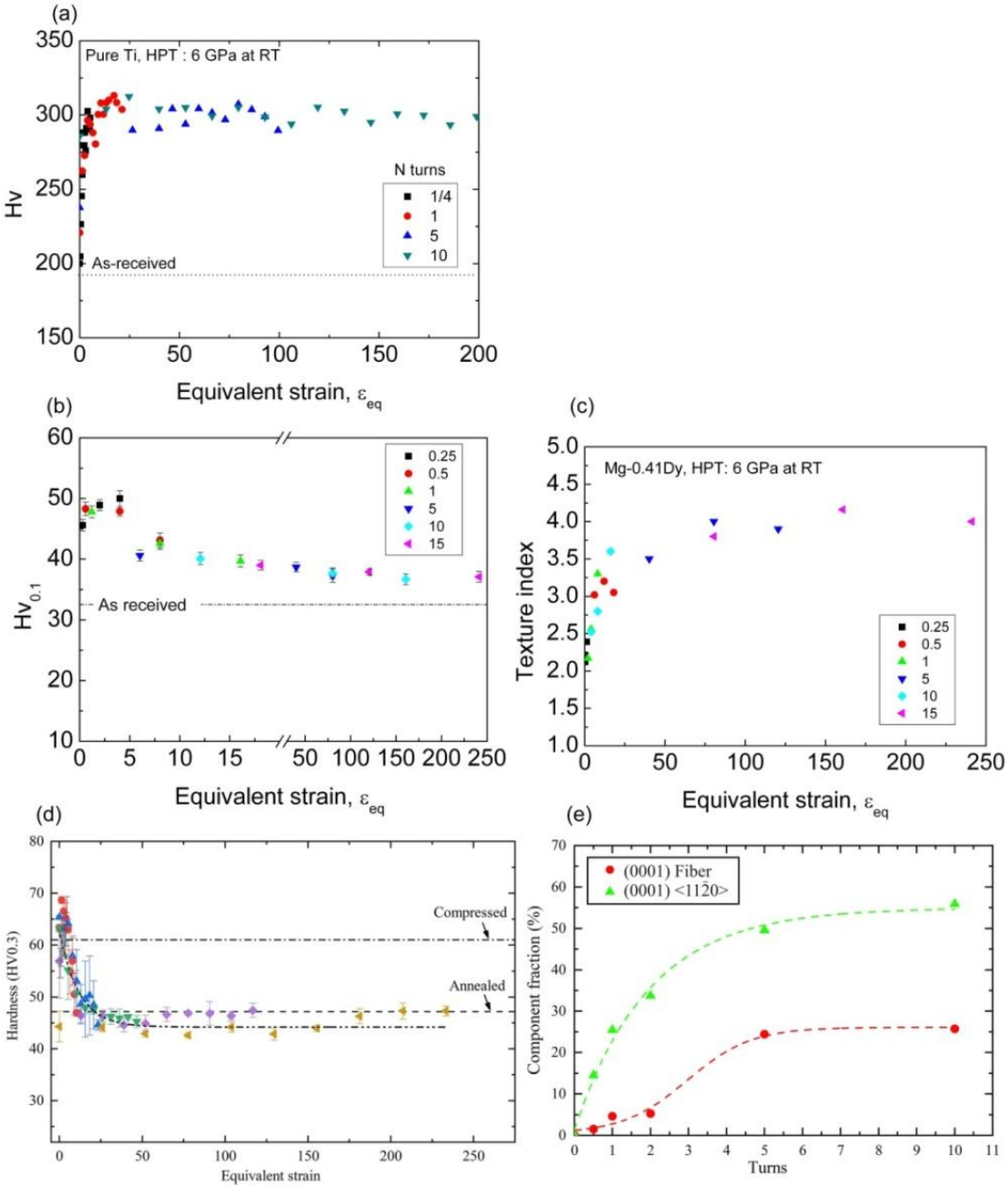

Figure 30 : Evolution of microhardness and texture intensity as a function of equivalent strain for pure Ti (a) [217], Mg-0.41Dy (b, c) [68] and Zn-0.5Cu (d, e) [218] alloys.

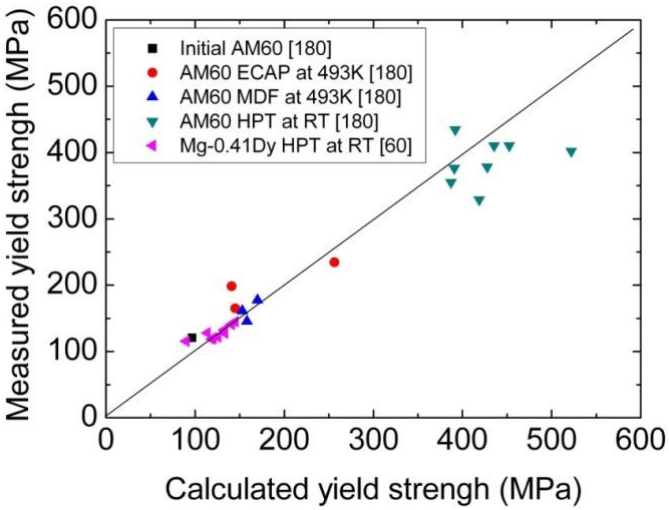

Figure 31: The measured yield strength as a function of the calculated values for AM60 alloys processed by ECAP, MDF and HPT [215] and for Mg-0.41Dy alloy processed by HPT [68].

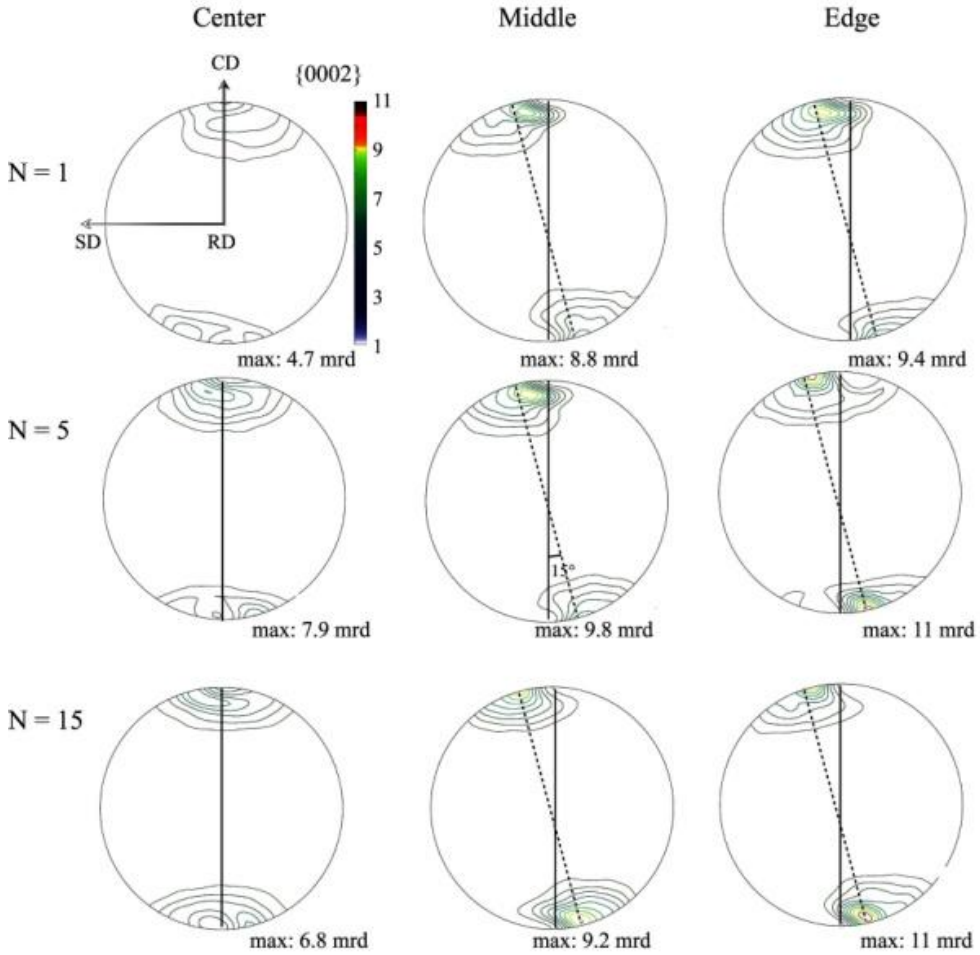

Figure 32: Basal {0002} pole figures near the center, middle and the edge of the discs of the Mg-0.41Dy (wt. %) alloy processed by HPT at RT to N = 1, 5 and 15 turns [68]. Reproduced with permission.

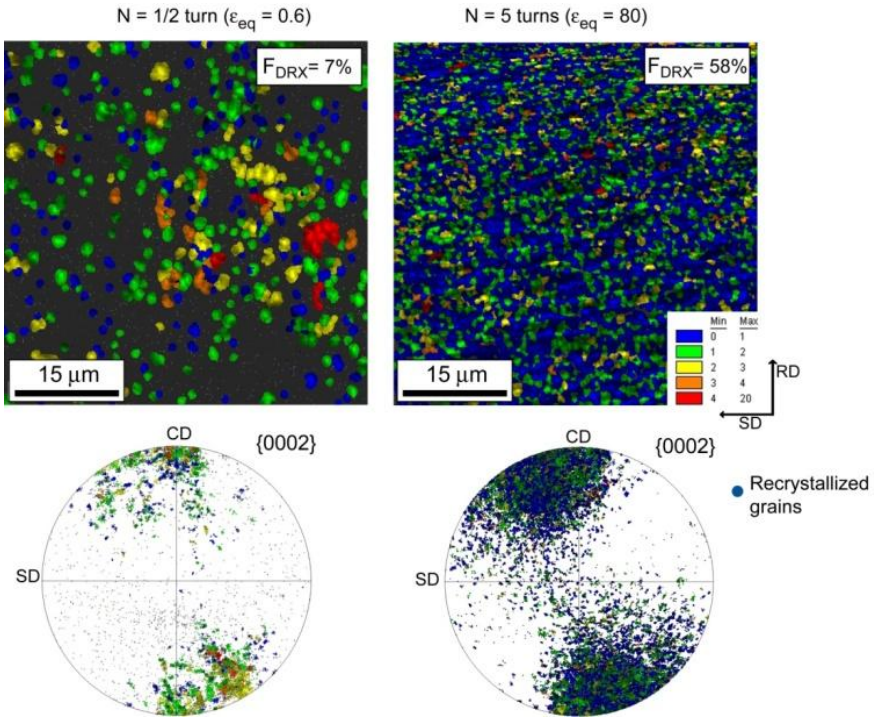

Figure 33: Grain orientation spread maps of the HPT processed Mg-0.41Dy alloy and the {0002} corresponding pole figures showing the orientation of the deformed and recrystallized grains obtained by grain orientation spread (GOS) approach [68].

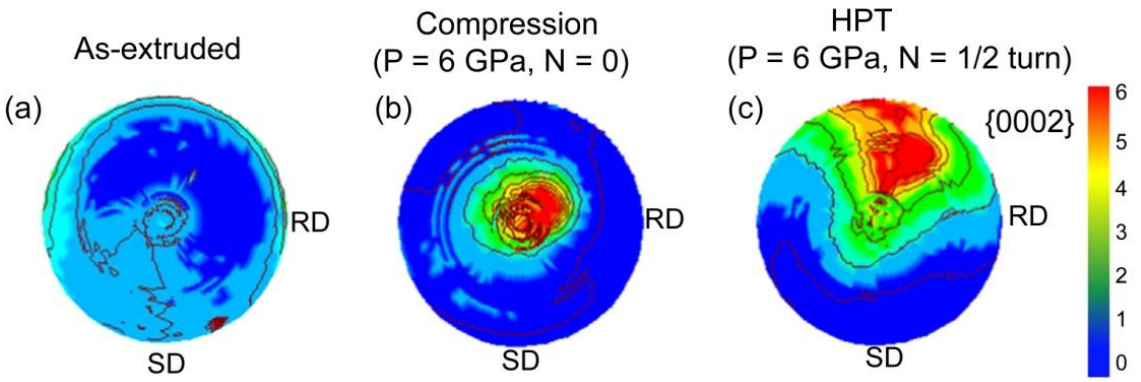

Figure 34: {0002} pole figures of AZ60A alloy at edge position: (a) initial state (as-extruded), (b) after compression under 6.0 GPa without torsion straining and (c) after HPT processing for N =1/2 under P = 6.0 GPa [205]. Reproduced with permission.

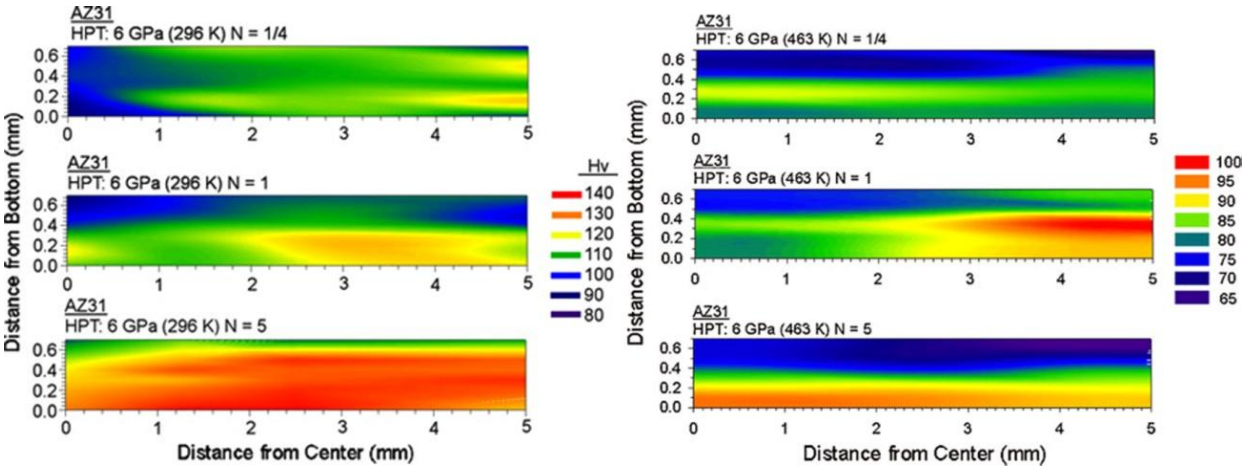

Figure 35: Color-coded maps showing the microhardness distributions across the one-half cross-sections of discs of AZ31 alloy after processing by HPT at 296 and 463 K for 1/4, 1, and 5 turns, respectively [221, 222].

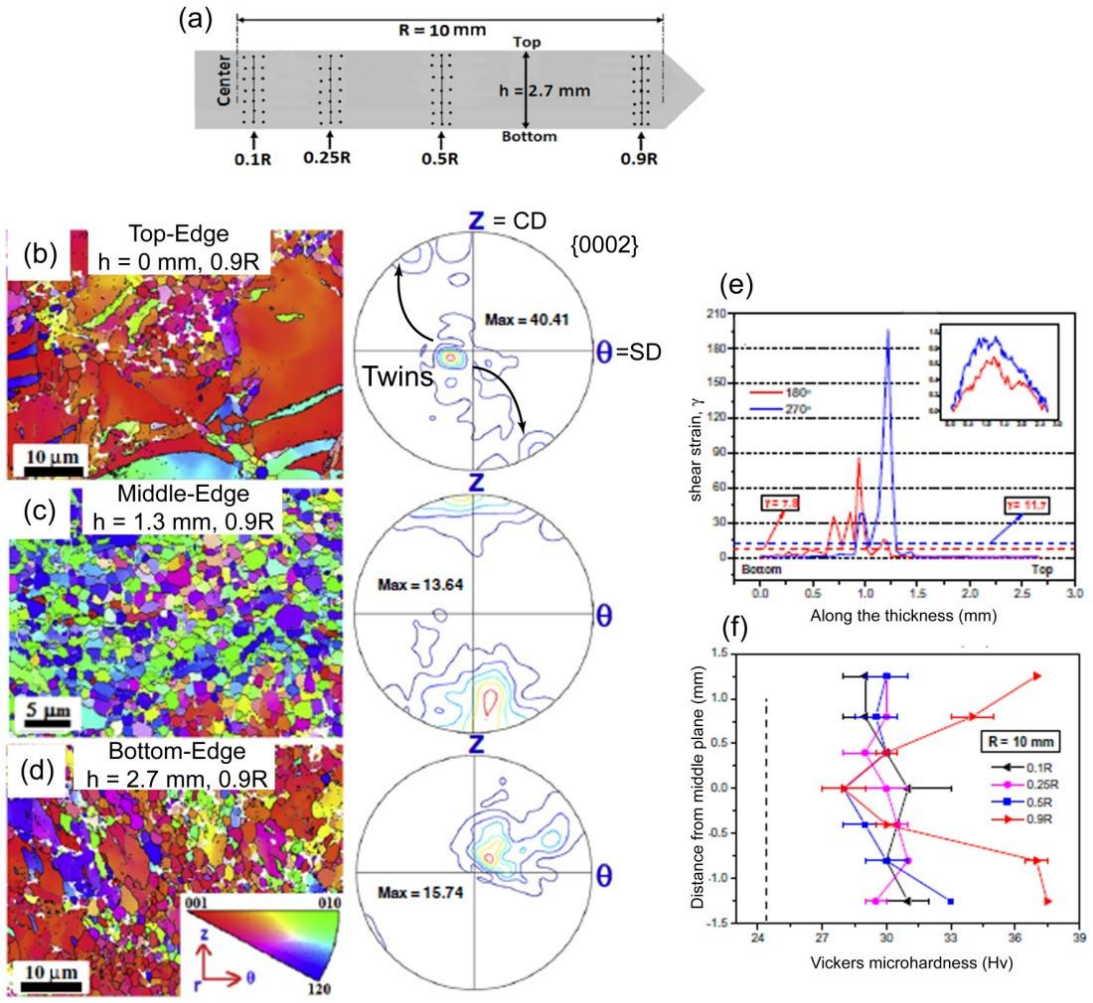

Figure 36: (a) Schematic illustration of cross-sectional plane of one-half of an HPT-disc showing the positions selected for Vickers microhardness and EBSD measurements. EBSD orientation maps and the corresponding {0002} pole figures measured at the edge of the disc: (b) top, (c) middle and (d) bottom sections. (e) Strain distribution across the through-thickness and (f) distributions of Vickers microhardness in the radial direction across the through-thickness in pure Mg processed at RT for 270° rotation (N = 3/4 turn) [175]. Reproduced with permission.

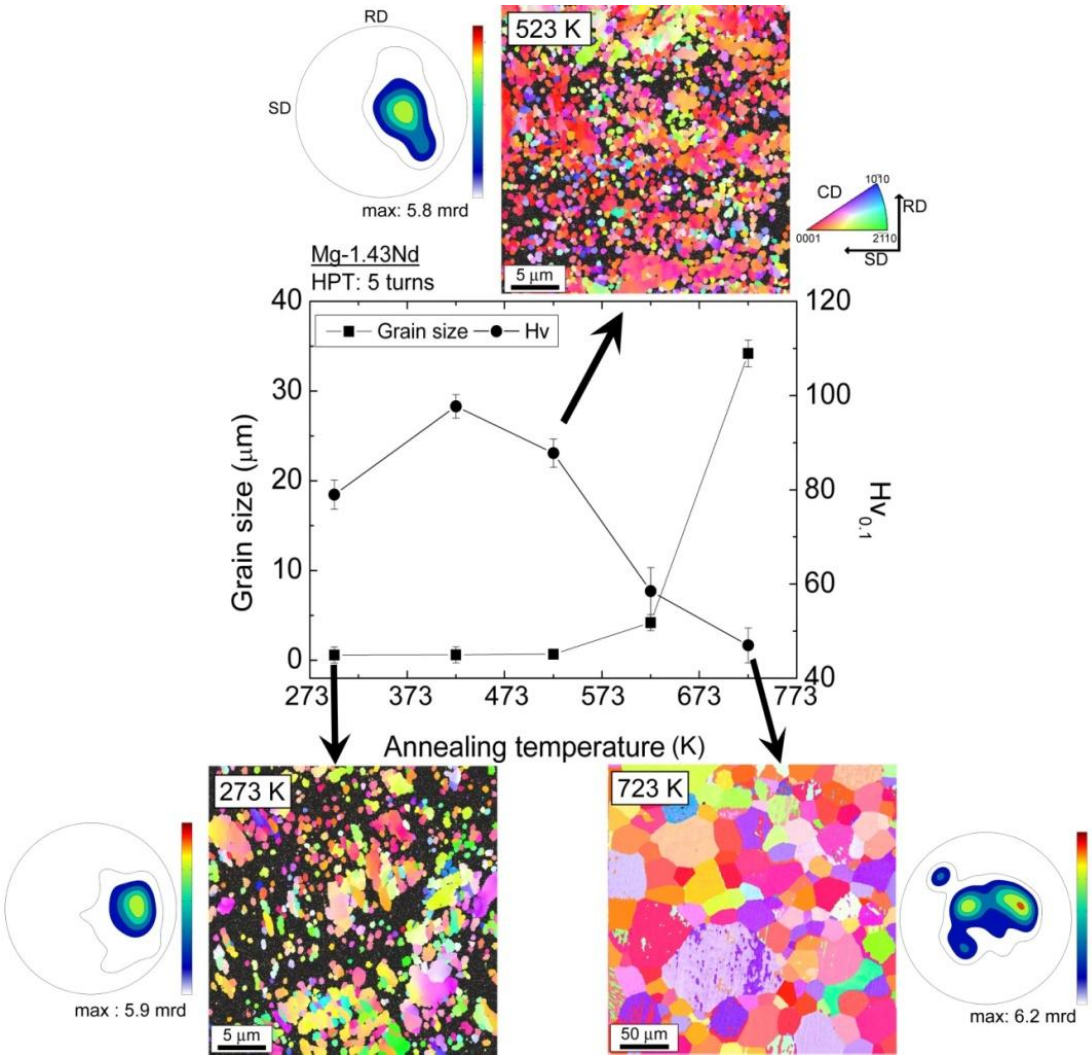

Figure 37: Evolution of texture, grain size and microhardness as a function of annealing temperature of the HPT processes at N = 5 turns [10].

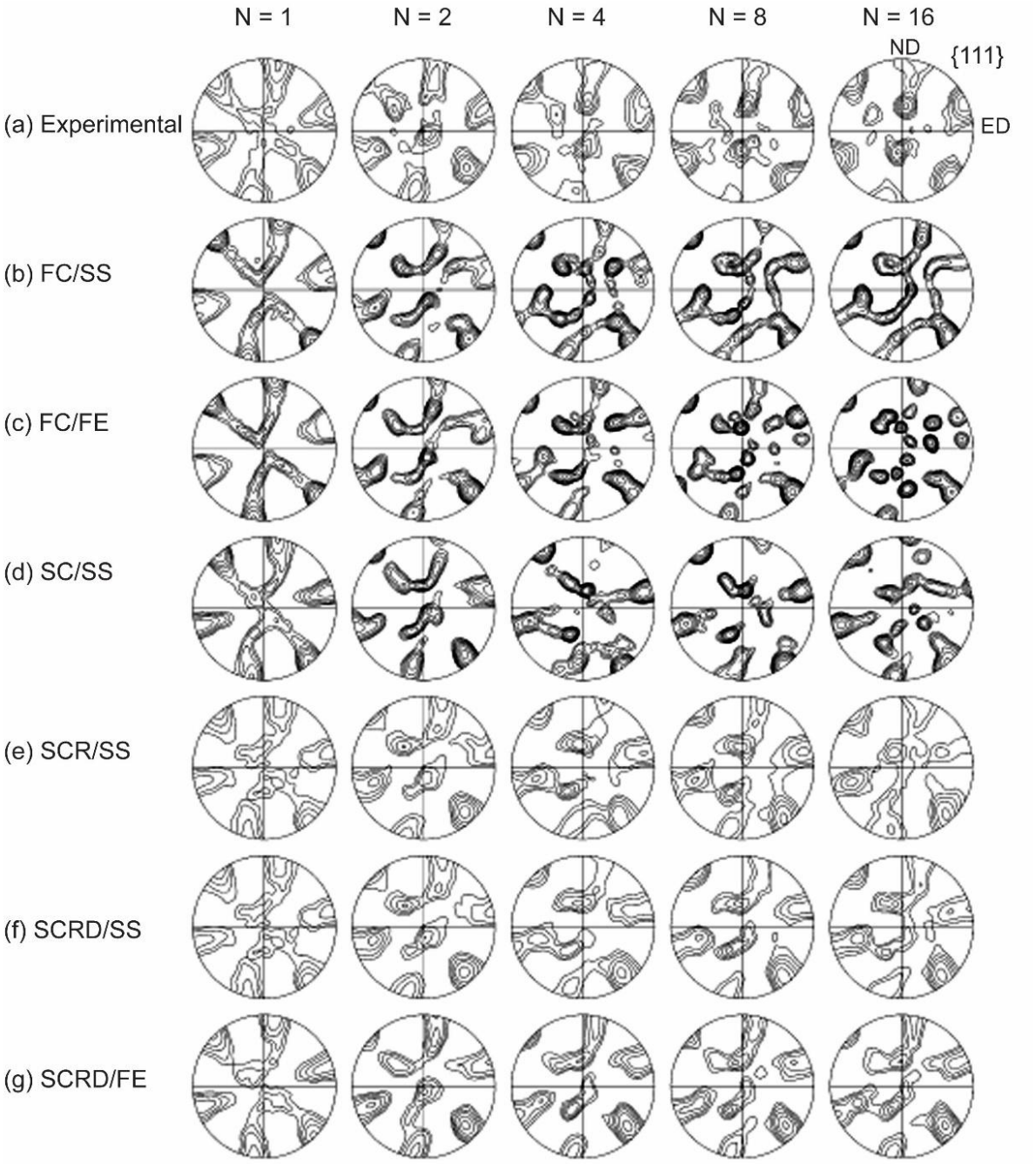

Figure 38: Evolution of texture as a function of number of ECAP passes via route Bc. (a) experimental results and simulated resulted by: (b) FC/SS, (c) FC/FE, (d) SC/SS, (e) SCR/SS, (f) SCRD/SS and (g) SCRD/FE methods (see Table 11) [233]. Contours: 1/1.4/2.8/4/5.6/8/11/16/22. Reproduced with permission.

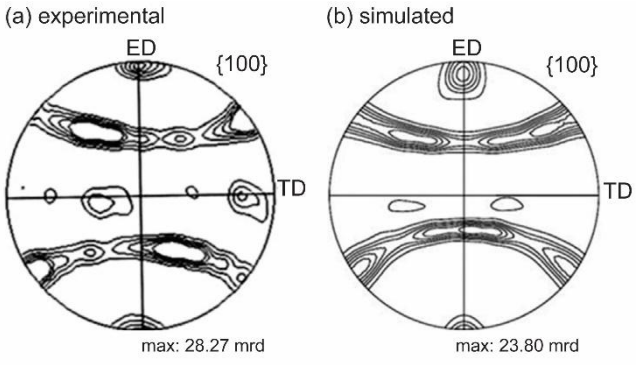

Figure 39: (a) Experimental and (b) predicted {100} pole figures for micro-extruded ultra-fine grains copper [247, 248]. Contours: 1.2/2/2.5/3/3.5/4/8/12/20. Reproduced with permission.

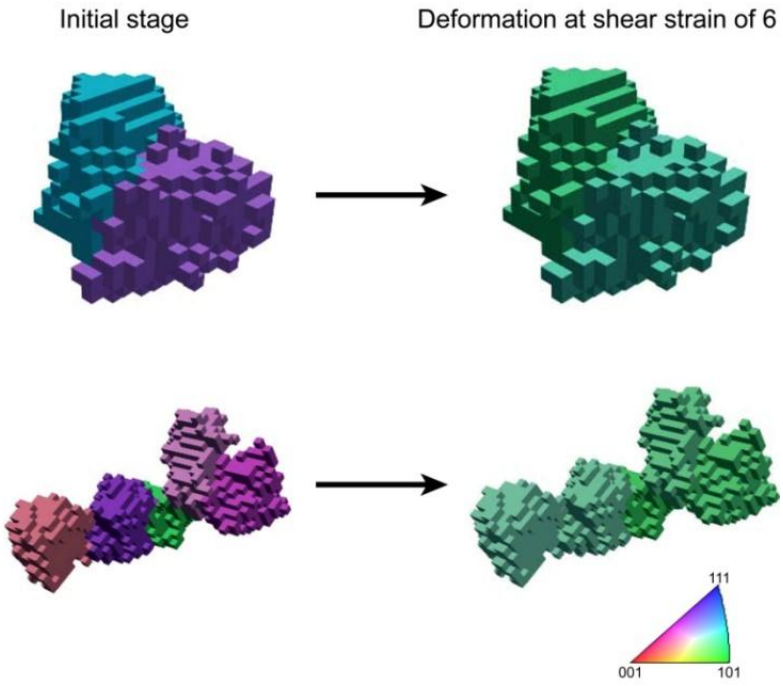

Figure 40: Typical morphologies for orientation evolution induced grain coarsening events obtained by 3D simulation [98].

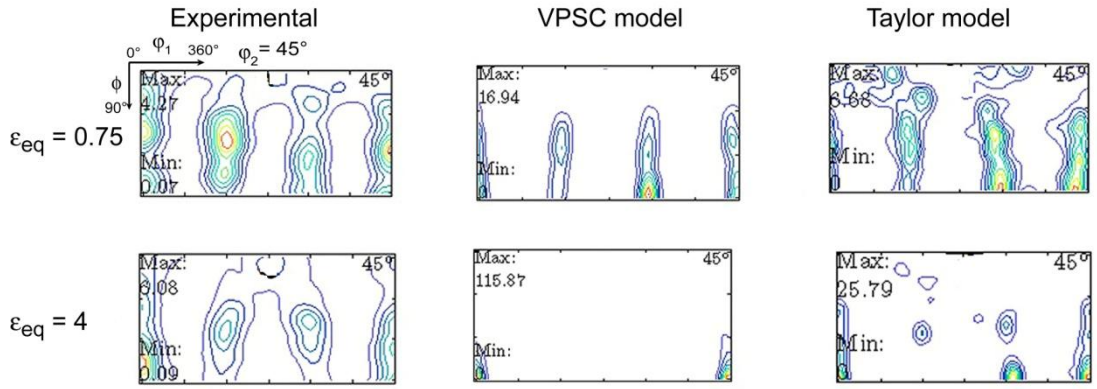

Figure 41: Experimental and predicted texture evolution using VPSC and Taylor models after HPT processing of CP Al at ε_{eq} = 0.75 and 4 [116].

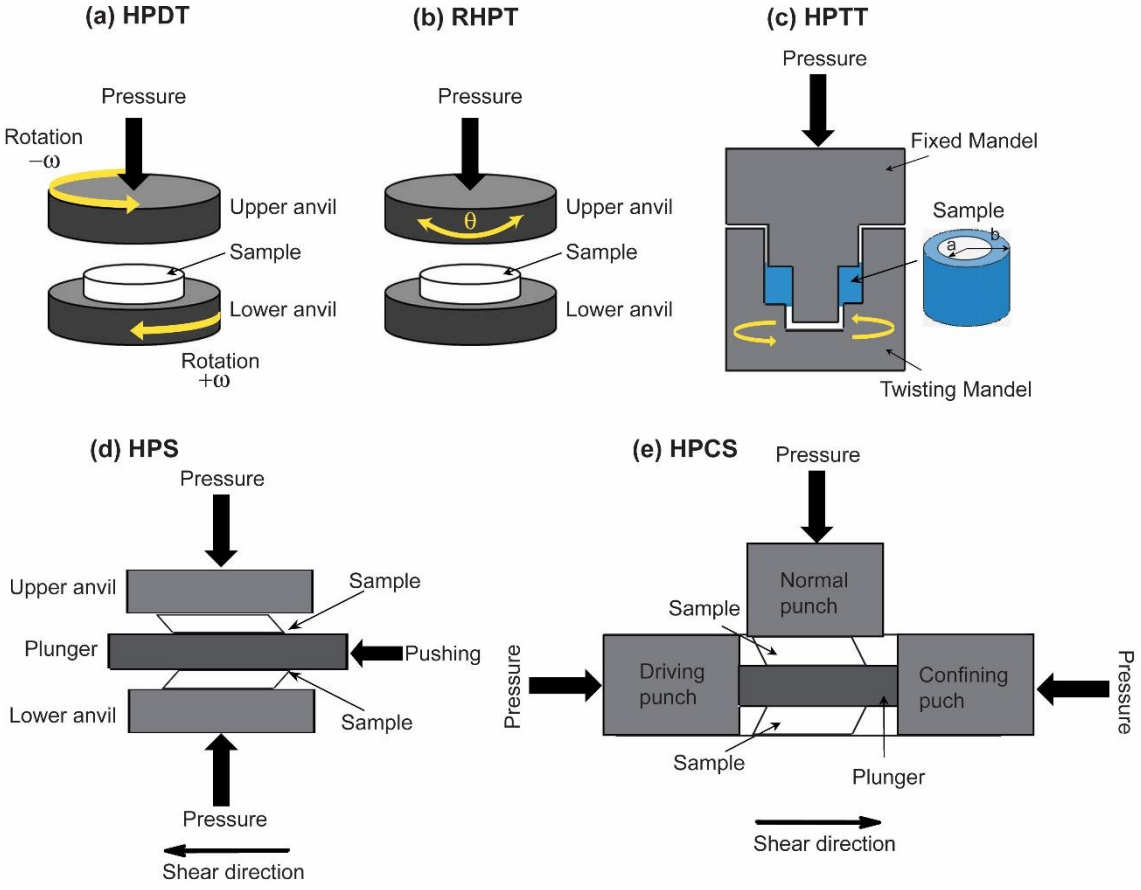

Figure 42: Scheme of: (a) high pressure double torsion (HPDT), (b) reversal high pressure torsion (RHPT), (c) high pressure tube twisting (HPTT), (d) high pressure shearing (HPS) and (e) high pressure compressive shearing (HPCS).

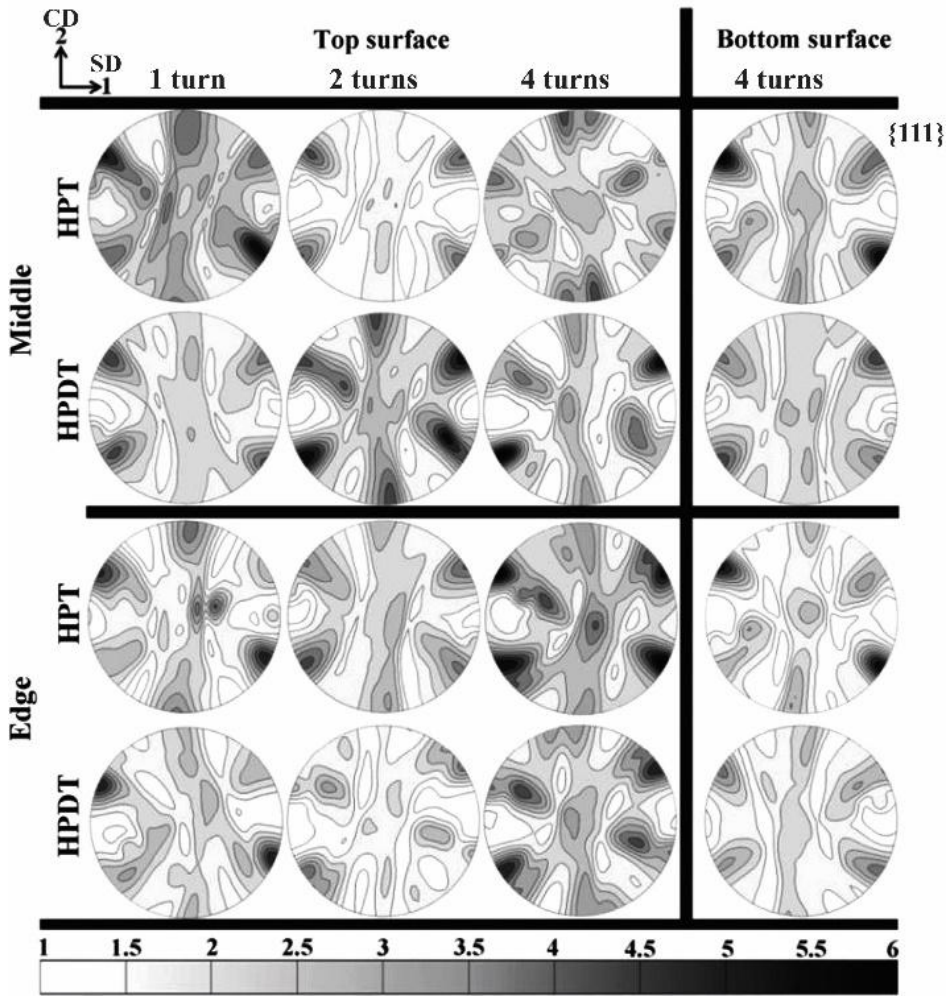

Figure 43: Evolution of the texture of CP Cu discs processed by HPT and HPDT as a function of the disk location and the numbers of turns [263]. Reproduced with permission.

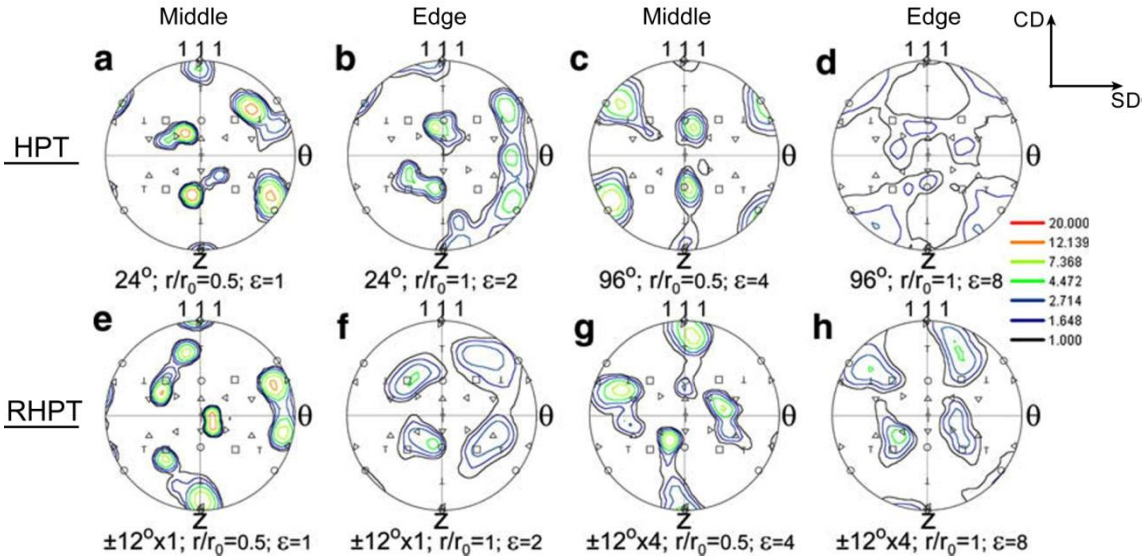

Figure 44: {111} pole figures of the pure Al after monotonous (HPT) processing (a-d), RHPT processing (e-h) and the ideal position of the shear component in the {111} pole figure (i) [118]. Reproduced with permission.

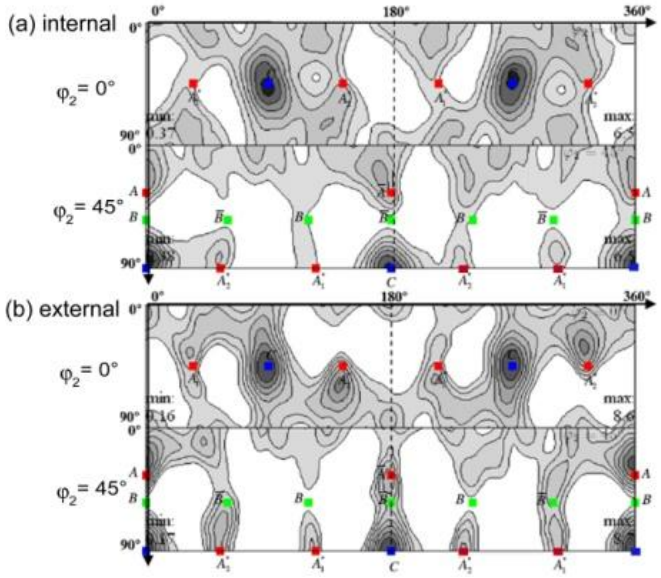

Figure 45: ODF sections at φ_2 = 0 and 45 ° at (a) the internal and (b) external surfaces of the tube of CP Al alloy after HPTT processing for an average shear of 2 [34]. Reproduced with permission.

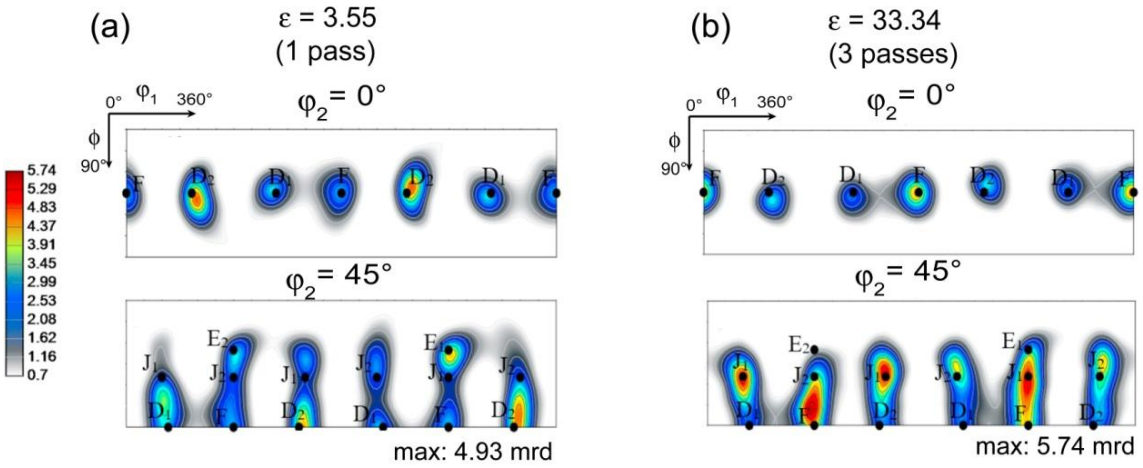

Figure 46: ODF sections at φ_2 = 0 and 45 ° of ARMCO steel (BCC) after HPCS processing at RT through: (a) pass and (b) 3 passes [39]. Reproduced with permission.